Analysis of the different signal acquisition schemes of an optical feedback based laser diode interferometer

Jalal Al Roumy

THÈSE

En vue de l'obtention du

DOCTORAT DE L'UNIVERSITÉ DE TOULOUSE

Délivré par :

Institut National Polytechnique de Toulouse (INP Toulouse)

Discipline ou spécialité :

Micro-ondes, Électromagnétisme et Optoélectronique

Présentée et soutenue par :

M. JALAL AL ROUMY

le mardi 20 septembre 2016

Titre :

ANALYSIS OF THE DIFFERENT SIGNAL ACQUISITION SCHEMES OF AN OPTICAL FEEDBACK BASED LASER DIODE INTERFEROMETER

Ecole doctorale :

Génie Electrique, Electronique, Télécommunications (GEET)

Unité de recherche :

Laboratoire d'Analyse et d'Architecture des Systèmes (L.A.A.S.)

Directeur(s) de Thèse :

M. THIERRY BOSCH

M. JULIEN PERCHOUX

Rapporteurs :

M. MAURIZIO DABBICCO, UNIVERSITA DEGLI STUDI DI BARI

M. SANTIAGO ROYO, CD6 Universitat Politecnica Catalunya

Membre(s) du jury :

M. MICHEL LEQUIME, ECOLE CENTRALE DE MARSEILLE, Président

M. JULIEN PERCHOUX, INP TOULOUSE, Membre

M. PHILIPPE ARGUEL, UNIVERSITE PAUL SABATIER, Membre

M. THIERRY BOSCH, INP TOULOUSE, Membre

Acknowledgments

I would like to express my admiration and gratitude to my Prof. Thierry Bosch, thesis advisor, for granting me the opportunity of being part of the OSE research group. His scientific skills and perpetual willingness to listen have made an enormous contribution to this work, while his humanity and advices allowed me to overcome the hard times along this journey.

All my respect and compliments go to Dr. Julien Perchoux for co-advising my work. Always full of sureness, his insights and friendship increased the confidence on my background knowledge and empowered the joy of becoming proficient in the domain of optical sensing. He was so patient with me and provided me with so many helpful advices whenever I struggled due to home sickness or worrisome about the situation of my family.

I would also like to thank Mr. Maurizio Dabbicco and Mr. Santiago Royo for accepting to be the reviewers of my thesis. I am thankful for any advice and suggestions from all the jury members.

The financial support provided by the French Government which was directed during the three years by the Campus France, is gratefully acknowledged. My special thanks go to the Academic Cooperation Division in the French Consulate in Jerusalem for selecting me to this program.

I’m grateful to all the researchers and staff of this group for their kindness and the positive work ambiance all these years, Marc Lescure, Michel Cattoen, Francoise Lizion, Olivier Bernal, Francis Bony, Hélène Tap, Han-Cheng Seat and Adam Quotb. I'm also grateful to Clement Tronche and Francis Jayat for their great help in conducting the experiments, and Emmanuelle Tronche for her help in the management stuff.

I treasure the time spent with all my fellow PhD students, Antonio Luna Arriaga, Bendy Tanios, Lucas Perbet, Blaise Mulliez, Mohanad Albughdadi, Haris Apriyanto, Laura Le Barbier, Lavinia Ciotirca, Evelio R. Miquet, Yu Zhao, Raul Da Costa Morerira and Patricio Fernando Urgiles Ortiz. My thoughts and

appreciation for the many other great people who I had the pleasure to know and exchange opinions in this research centre, Gautier, Usman, Laurent, Luc Eric, Sabine, Florentin and Jose Luis.

The work on this manuscript has been accomplished with the support and encouragement from the people who has been with me since the beginning, my parents who have devoted their life to make me grow integrally as well as my brother and sisters. There are no words to thank the precious time that you gave me, I dedicate this work to you.

Table of Contents

Acknoledgment ..... **iii**

Table of Contents ..... **v**

List of Figures ..... **vii**

List of Tables ..... **xiii**

General Introduction **1**

1 Principle and Applications of Optical Feedback Interferometry **5**

1.1 Introduction to the History of Optical Feedback Interferometry 6

1.2 Principle of the Optical Feedback Interferometry 10

1.2.1 Model of coupled cavities 12

1.3 Applications of Optical Feedback Interferometry 22

1.3.1 Typical sensing applications 23

1.3.2 High sensitive sensing applications 30

1.4 Conclusion 34

2 Modelling of Optical Feedback Interferometric Signals **35**

2.1 Re-demonstration of OFI Rate Equations Model 38

2.1.1 Standalone laser diode 39

2.1.2 Laser diode subject to optical feedback 49

2.2 Amplitudes of LV and PD OFI signals 53

2.2.1 Photodetected signal 54

2.2.2 Voltage signal 60

2.3 Analysis of the Front PD Signal 64

2.4 Conclusion 70

3 Experimental Validation of the OFI Signal Modelling **71**

3.1 Validation of the Model for Single-mode Laser Diodes 72

3.1.1 Description of the Experimental Setup 72

3.1.2 Detailed description and characterization of both laser diodes 75

3.2 Experimental Validation 81

3.2.1 A DFB laser diode subject to optical feedback 81

3.2.2 A VCSEL subject to optical feedback 89

3.3 OFI Signals Strength Evolution for Multimode Lasers 95
3.4 The Case of the Front PD Signal 100
3.4.1 Comparison of the amplitudes of the front and the back PD signals ..
..... 100
3.4.2 Phases of front and back PD signals 104
3.4.3 Ratio of modulation indices 109

4 Improvement of the OFI sensor sensitivity using multiple acquisition schemes 111
4.1 Description of the Experimental Setup 113
4.2 Theoretical Background 114
4.2.1 Noise sources in different acquisition schemes 114
4.2.2 The applied signal processing techniques 115
4.2.2 Validation on ideal signals 119
4.3 Experimental Results 122
4.3.1 Different feedback levels 123
4.3.2 Different injection currents 135
4.4 Conclusion 139

General Conclusion 134

Bibliography 147
List of Publications 165
Abstract/Résumé 166

List of Figures

Fig. 1.1: A comparison between a conventional interferometer (left) and the OFI interferometer (right) 10
Fig. 1.2: A schematic diagram of a laser commercial package with a built-in monitoring photodiode 11
Fig. 1.3: A simple Fabry-Pérot model of the solitary laser diode. 12
Fig. 1.4: The three-mirror model of a laser diode subject to optical feedback 14
Fig. 1.5: The reduced model of laser diode subject to optical feedback 15
Fig. 1.6: The round-trip phase change against the lasing frequency change simulated for different values of the feedback parameter C 20
Fig. 1.7: The regimes of feedback levels at different power ratios..... 22
Fig. 1.8: The displacement of a target can be retrieved from processing the OFI signal acquired for a target moving along the optical path of a laser diode: (a) basic representation of the displacement measurement setup, and (b) a sinusoidal displacement with sawtooth-like fluctuations 24
Fig. 1.9: a) Laser Doppler velocimetry demonstration with a VCSEL sensor: a) basic representation of the velocity measurement setup and b) an OFI signal spectrum..... 27
Fig. 1.10: Optical power variations and their corresponding beat frequencies for a triangular injection current..... 29
Fig. 1.11: Schematic diagram of the of the acoustic filed measurement setup..... 31
Fig. 1.12: Ppropagation of the acoustic field with the ultrasonic transmitter propagating the field into free space; Left: Measured, Right: Simulation..... 32
Fig. 1.13: Experimental setup for edge filter enhanced self-mixing interferometry (ESMI) experiments 33
Fig 2.1: A block diagram of the laser diode and the photodiodes 36
Fig 2.2: Flowchart that illustrates the main stages undergone to derive the OFI model equations 37
Fig. 2.3: Evolution of the PD and LV OFI Signals strengths with laser injection current 63
Fig. 2.4: Evolution of the PD and LV OFI Signals strengths with the operating temperature 64

Fig 2.5: A schematic representation of the phase relationship model 65
Fig 2.6: The ratio of modulation indices as a function of injection current 69
Fig 2.7: Evolution of the front and the back PD signals normalised strengths with laser injection current 69
Fig. 3.1: Photography of the experimental setup for measuring velocity of a rotating disk: 1) a micrometric 3-axis mechanical stage, 2) lens, 3) neutral density, 4) rotating disk (target), 5) needle, 6) laser driver, and 7) amplifier 73
Fig. 3.2: Block diagram of the experimental setup inside the climatic chamber . 73
Fig. 3.3: Output optical power of the DFB laser as a function of laser injection current measured at different operating temperatures (ranging from -40˚C to 80˚C in steps of 5˚C) 77
Fig. 3.4: Measured (solid lines) and fitted (dashed and dotted lines) slope efficiency and threshold current of the DFB laser diode as a function of the operating temperature. The upper slope efficiency curve is the maximum while the lower one is the average 78
Fig. 3.5: Output optical power of the VCSEL as a function of laser injection current measured at different operating temperatures (ranging from 0˚C to 80˚C in steps of 5˚C). 79
Fig. 3.6: Slope efficiency and threshold current of the VCSEL as a function of the operating temperature 80
Fig. 3.7: The Doppler signal spectrum. The inset shows the fitting of the measured spectrum (black) to a combination of a Gaussian function and a linear function fitting the noise floor (green) 82
Fig. 3.8: Evolution of the PD signal amplitude of the DFB with laser injection current: measured (red solid); modelled (constant slope efficiency of an ideal laser diode, green dashed); modelled (actual slope efficiency, blue solid)..... 83
Fig. 3.9: Evolution of the LV signal amplitude of the DFB with laser injection current: measured (red solid); modelled (constant slope efficiency of an ideal laser diode, green dashed); modelled (actual slope efficiency, blue solid). 83
Fig. 3.10: Evolution of the PD signal amplitude of the DFB with the operating temperature: measured (red solid); modelled (actual slope efficiency, blue solid). 85

Fig. 3.11: Evolution of the LV signal amplitude of the DFB with the operating temperature: measured (red solid); modelled (actual slope efficiency, blue solid). 85
Fig. 3.12: PD signal strength of the DFB laser diode as a function of the injection current and the operating temperature: (a) measured and (b) modelled 87
Fig. 3.13: LV signal strength of the DFB laser diode as a function of the injection current and the operating temperature: (a) measured and (b) modelled 88
Fig. 3.14: Evolution of the PD signal amplitude of the VCSEL with laser injection current at 20℃: measured (red solid); modelled (constant slope efficiency of an ideal laser diode, green dashed); modelled (actual slope efficiency, blue solid). 89
Fig. 3.15: Evolution of the LV signal amplitude of the VCSEL with laser injection current: measured (red solid); modelled (constant slope efficiency of an ideal laser diode, green dashed); modelled (actual slope efficiency, blue solid). 90
Fig. 3.16: Evolution of the PD signal amplitude of the VCSEL with the operating temperature: measured (red solid); modelled (actual slope efficiency, blue solid). 91
Fig. 3.17: Evolution of the LV signal amplitude with the operating temperature of the VCSEL: measured (red solid); modelled (actual slope efficiency, blue solid) 91
Fig. 3.18: PD signal strength of the VCSEL as a function of the injection current and the operating temperature: (a) measured and (b) modelled 93
Fig. 3.19: LV signal strength of the VCSEL as a function of the injection current and the operating temperature: (a) measured and (b) modelled 94
Fig. 3.20 The two-mode operation of the VCSEL a) the operating wavelength and b) the total output power and detected power of each mode. 96
Fig. 3.21: Evolution of the PD OFI signal amplitude with the laser injection current in the two-mode VCSEL. Solid blue line: simulated taking into account the actual slope efficiency; dashed line: simulated with constant slope efficiency; red solid line: measured. 97
Fig. 3.22: Evolution of the amplitude of the voltage OFI signal with laser injection current in the two-mode VCSEL. Solid blue line: simulated taking into account the actual slope efficiency; dashed line: simulated with constant slope efficiency; red solid line: measured. 98

Fig. 3.23: Evolution of the PD OFI signal amplitude with laser injection current in the two-mode VCSEL 99
Fig. 3.24: Evolution of the voltage OFI signals amplitudes with injection current for multimode laser diodes 99
Fig. 3.25: Experimental setup used for the simultaneous measurement of the front and back PD signals 101
Fig. 3.26 Back (upper plots) and front (lower plots) PD signals at different bias currents: a) I = 6 mA, PD signals are in-phase, b) I = 9 mA, front PD signal vanishes, c) I = 16 mA, signals are out-of-phase 102
Fig. 3.27 Evolution of the amplitudes of the back (blue trace) and front (green trace) PD signals with laser injection current at different attenuation levels: top) No neutral density is introduced to the optical path; middle) Attenuation level is 16 dB; bottom) Attenuation level is 20 dB. 103
Fig. 3.28 Photocurrents as a function of the injection current measured at different attenuation levels (purple solid line for external photodiode, and golden solid line for the internal photodiode) 104
Fig. 3.29 The phase difference as a function of frequency at: a) 7 mA, and b) 27 mA. 105
Fig. 3.30 Histogram of the phase difference at: a) 7 mA, and b) 27 mA. 106
Fig. 3.31 Histogram of the corrected phase difference at: a) 7 mA, and b) 27 mA. 107
Fig. 3.32 Phase differences as a function of the laser injection current measured at different attenuation levels (blue solid line for the case of no attenuation; green solid line for the case of 16 dB attenuation; and red solid line for the case of 20 dB attenuation). 108
Fig. 3.33 Ratio of modulation indices as a function of the injection current both modelled (black solid line) and measured at different attenuation levels (blue solid line for the case of 0 dB attenuation; green solid line for the case of 16 dB attenuation; and red solid line for the case of 20 dB attenuation). 110
Fig. 4.1: Spectrum of a noisy sinusoidal signal with a frequency of 1 kHz and an amplitude of 1, accompanied by a white Gaussian noise with a standard deviation of 0.2. The SNR in decibel is measured as the difference between the signal amplitude at 1 kHz and the average noise level elsewhere 112

Fig. 4.2: The sum and the difference SNRs of the input signals as a function of the phase shift (solid blue is the sum, and solid green is the difference). The SNRs of the input signals are equal and are normalised at 0° 121
Fig. 4.3: SNRs of OFI signals obtained at 6.5 mA for different feedback levels (solid red: LV signal, solid black: back PD signal, and solid blue: front PD signal). 124
Fig. 4.4: SNRs of the output signals obtained from the autocorrelation of the OFI signals at 6.5 mA for different optical feedback levels (solid blue: obtained values, and dashed red: expected values) 125
Fig. 4.5: SNRs of the cross-correlation of the OFI signal pairs obtained at 6.5 mA for different feedback levels (solid blue: obtained values, and dashed red: expected values) 126
Fig. 4.6: SNRs of either the addition or the subtraction of the OFI signal pairs obtained at 6.5 mA for different attenuation levels (solid blue: obtained values, and dashed red: SNRs of the OFI signals) 128
Fig. 4.7: SNRs of OFI signals obtained at 20 mA for different feedback levels (solid red: LV signal, solid black: back PD signal, and solid blue: front PD signal) 130
Fig. 4.8: SNRs of the output signals obtained from the autocorrelation of the OFI signals at 20 mA for different optical feedback levels (solid blue: obtained values, and dashed red: expected values) 131
Fig. 4.9: SNRs of the cross-correlation of the OFI signal pairs obtained at 20 mA for different feedback levels (solid blue: obtained values, and dashed red: expected values) 132
Fig. 4.10: SNRs of either the addition or the subtraction of the OFI signal pairs obtained at 20 mA for different attenuation levels (solid blue: obtained values, and dashed red: SNRs of the OFI signals). 134
Fig. 4.11: SNRs of OFI signals as a function of laser injection current (solid red: LV signal, solid black: back PD signal, and solid blue: front PD signal). 135
Fig. 4.12: SNRs of the output signals obtained from the autocorrelation of the OFI signals measured at different laser injection currents (solid blue: obtained values, and dashed red: expected values). 136

Fig. 4.13: SNRs of the cross-correlation of the OFI signal pairs as a function of laser injection current (solid blue: obtained values, and dashed red: expected values)..... 137
Fig. 4.14: SNRs of either the addition or the subtraction of the OFI signal pairs obtained at different laser injection currents (solid blue: obtained values, and dashed red: SNRs of the measured OFI signals). 138
Fig. 4.15: SNRs of the outputs of the different signal processing techniques (AC: autocorrelation, XC: cross-correlation, sum and difference) of the different OFI input signals (L: LV signal, B: back PD signal, and F: front PD signal) acquired at 6.5 mA for different attenuation levels (red solid: 0 dB, black solid: 12 dB, and blue solid: 20 dB) 139
Fig. 4.16: SNRs of the outputs of the different signal processing techniques (AC: autocorrelation, XC: cross-correlation, sum and difference) of the different OFI input signals (L: LV signal, B: back PD signal, and F: front PD signal) acquired at 20 mA for different attenuation levels (red solid: 0 dB, black solid: 12 dB, and blue solid: 20 dB). 140
Fig. 4.17: Comparison of the SNRs of both the cross-correlation and the difference of the LV and back PD signals as a function of the laser injection current (solid red: cross-correlation and solid blue: difference). 141
Fig. 4.18: Comparison of the SNRs of both the cross-correlation and the difference of the front and back PD signals as a function of the laser injection current (solid red: cross-correlation and solid blue: difference). 141

List of Tables

Table 1.1: The characteristics of the regimes of optical feedback levels..... 21
Table 3.1: A comparison of the lasers' absolute maximum ratings..... 76
Table 3.2: A comparison of the lasers' important parameters 76
Table 3.3: Laser parameters used for the calculation of the model curves 109
Table 3.4: Comparisons of the fitted and the standard values of the ratio of the carrier densities at transparency..... 109
Table 4.1: Calculated and evaluated SNRs of the output signals 121
Table 4.2: Calculated and evaluated SNRs of the sum of the in-phase input signals 122

General Introduction

Optical feedback interferometry (OFI) is a promising sensing technique for both industrial and laboratory environments due to its simple optical setup when compared to other interferometric techniques. Typical sensing applications of OFI are the measurement of displacement, absolute distance, vibration and velocity of solid targets.

The OFI sensing technique allows to design compact, self-aligned and cost-effective sensors with a very good precision comparable with the one offered by the more accurate, yet more complicated and more expensive, conventional interferometric sensors. This comes from the fact that, in OFI sensors, there is no need for a separate receiving channel to first gather and then mix the back-reflected optical power from the remote target, which is the case in conventional interferometry. In the OFI sensing scheme, the back-reflected laser beam is coupled into the active laser cavity where it induces changes of the lasing frequency and the optical power of the laser diode. These perturbations, and in particular the power perturbation, are carrying information on the remote target and the external cavity.

The most recent and exciting applications proposed for OFI sensors concern the monitoring of fluid flows and the imaging of acoustic wave. In the case of fluid flows at the micro-scale, small particles such as red blood cells are flowing in semi-transparent ducts and are the remote targets that induce the Doppler shifted back-scattering inside the laser cavity. For the imaging of acoustic wave, the sensors measures the pressure induced change of the refractive index in the external cavity formed by the laser and a fixed diffusing target. Despite their complete different nature, these two applications encounter the same challenge: the changes in the measurable quantity (laser power or laser frequency) are extremely small and can easily be drowned into the noise thus constraining the sensor's range of operation. In all applications requiring the detection of very small changes, OFI sensor signal strength is a key parameter which requires the full attention when designing the sensor. The objective of the present thesis is to describe both theoretically and experimentally the sensor parameters that impact directly the OFI signal amplitude.

OFI signals can be acquired by two different means: the first method is by observing the power fluctuations in the output optical power emitted from either the rear facet of the laser diode using the commonly built-in monitoring photodiode (denoted here as the rear PD signal) or the front facet using an external photodiode (denoted here as the front PD signal). The second method is by amplifying the variations in the laser junction voltage (denoted here as the LV signal). In this acquisition scheme, the laser diode acts simultaneously as: a light source, a micro-interferometer and a light detector. Actually, the latter method is the only measurement approach when a monitoring photodiode is not included in the laser diode package, as for example, when an array of laser diodes is used. Moreover, in the second configuration, the OFI sensor is reduced to the laser diode itself associated with a focusing lens, which is quite interesting for industrial applications as it opens up new possibilities for increased miniaturization of the sensor.

For both methods of signal acquisition in OFI sensors, in order to achieve the best performance, it is essential to maintain the maximum signal-to-noise ratio. Thus, this thesis proposes a simple mathematical model, applicable to single-mode laser diodes, which provides compact analytical expressions to quantitatively describe the dependence of OFI signal strength on the laser injection current. Due to the device-dependent nature of the optical feedback sensing scheme, we have limited our study to single-mode (transverse and longitudinal) laser diodes and only experimental results have been performed on multimode devices. The thesis manuscript has been written with the following order:

In the first chapter, an introduction to the OFI phenomenon is presented. The chapter consists of three major sections: a historical overview of the OFI phenomenon and the state-of-the art in this field is described in the first section. In the second section, the theoretical background required for a proper understanding of the phenomenon is presented. The expressions of the threshold gain, the emission frequencies and the phase condition are derived based on the equivalent cavity model. In the third section, various applications of the phenomenon are presented with a particular focus on the most demanding ones in term of signal strength.

The second chapter is dedicated to the demonstration of the analytical model that describes the evolution of the OFI signals strengths with the system parameters, and particularly the laser injection current. The derived model proposes an explanation to the experimentally observed divergent evolution of the PD and the LV signals with laser injection current. The chapter can be divided into three major sections: in the first section, a demonstration of the OFI rate equations for both the laser diode subject to optical feedback is presented. Those rate equations, and in particular the photon and the carrier densities, are then used as the basis for the derivation of the analytical model of OFI signals in the second section. The third section of this chapter investigates the phase relationship between the front and the rear PD signals as well as the ratio of their modulation indices expressed as a function of the laser injection current.

The third chapter consists of the experimental validation of the behaviour predicted by the analytical model that describes all three OFI signals. In the first section of the chapter, the model is experimentally validated for two different types of pure single-mode laser diodes: a distributed feedback (DFB) laser and a vertical-cavity surface-emitting laser (VCSEL), while in the second section, the model pertinence in the case of multimode laser diodes is evaluated: a transverse multimode VCSEL and a longitudinal multimode Fabry-Pérot (FP) type laser diode are thoroughly investigated.

In the fourth chapter, different signal processing techniques are applied to either two of the different OFI signals (the front PD signal, the rear PD signal and the LV signal) in search for any noticeable improvements in the characteristics of the signals, and in particular the SNR. The method is based on the hypothesis that acquisition of the same informative signal through two different sources should be emphasizing the signal while suppressing the noise. Autocorrelation, cross-correlation, and the simple arithmetic addition/subtraction operations were applied to a noisy sinusoidal reference signal, then to the experimentally obtained OFI signals.

Finally, a general conclusion is proposed and further evolution of the modelling effort and sensor improvement are discussed.

Chapter 1

Principle and Applications of Optical Feedback Interferometry

1.1 Introduction to the history of optical feedback interferometry

The Optical Feedback Interferometry (OFI) phenomenon occurs when a back-scattered light from an external object mixes optically with the electric filed within the active cavity of the laser diode thus inducing variations in its emitted power as well as its spectral properties. One of the problems with the first lasers constructed in 1960 [1, 2] was the presence of multiple longitudinal modes of emission. To counter this problem, Kleinman and Kisliuk first proposed in 1962 that the mode structure of the laser could be modified through the addition of an external mirror [3]. Such arrangement was first demonstrated for a Helium-Neon (He-Ne) laser in the same year by Kogelnik and Patel [4]. Many subsequent works in the following years demonstrated that mode selectivity could be achieved with the addition of reflective elements inside or outside the laser cavity [5-11].

In 1963, King and Steward first demonstrated that optical feedback could also be used for metrology applications when they observed the variation of the output power of a He-Ne laser with the distance to the external mirror [12]. The output power changes were periodic functions of the distance to the external mirror with a period of half the laser's wavelength, a behaviour that was used later in many other He-Ne laser interferometers to measure velocity [13] or the refractive index [14-21] and density of plasma [22-29]. In 1972, Wheeler and Fielding first observed that the optical feedback interference fringes could also be monitored as a change in the voltage across the discharge tube [29], interestingly highlighting the ability to perform interferometry using only the laser itself without any extra photodetector.

Meanwhile, in 1964 Yeh and Cummins first performed a series of experiments where a reference beam from the laser and the light scattered from a fluidic chip were coherently mixed onto an external photodiode (PD) to determine the flow rate using the Doppler-Fizeau effect [30, 31]. In this technique, the optical components should be accurately aligned to ensure that the reference and scattered beams are nearly parallel when mixed onto the PD [32], which, in practice, is a difficult task. In 1968, Rudd reported the first auto-aligned configuration using a He-Ne laser when he experimentally proved that the mixing of the scattered and reference beams could take place inside the laser cavity and detected with a PD at

the rear facet of the laser, demonstrating the measurement of velocity by exploiting the Doppler frequency shift [32]. Since then, the interest to use OFI as a reliable technique for instrumentation was revealed.

Those early demonstrations of the OFI were performed with the large and bulky He-Ne lasers. In 1962, the more compact and lower cost semiconductor lasers were first constructed, and just like the first gas lasers they were also exhibiting multiple modes of emission [33-36]. In 1964, Crowe and Craig first showed that the linewidth of the lasing spectrum could be reduced or even further that the single-mode emission could be achieved using the optical feedback [37]. In 1968, the change of the threshold carrier density of the semiconductor lasers due to the optical feedback was shown by Bachert and Raab [38] as well as Morosov et al. who also observed that this change was dependent on the distance to the external mirror [39]. Furthermore, Morosov reported that the influence of the optical feedback on the dynamical properties of the laser diode, and in particular the oscillating frequency.

In 1969, Broom discovered that a considerable enhancement in the intensity noise of the output power at the relaxation oscillation frequency as well as the noise of the voltage across the laser junction could be achieved when the spacing between the longitudinal modes in the external cavity was equal to the relaxation oscillation frequency of the laser diode [40]. This work as well as a subsequent theoretical analysis in 1970 [41] showed that the dynamic behaviour of the laser diode with optical feedback was also dependent on the strength of the light coupling from the external cavity.

Despite all these experimental observations, there was no theoretical model that could accurately describe the origins of the dynamical operation of semiconductor lasers with optical feedback until 1980, when Lang and Kobayashi showed that the changes in the carrier density of the laser diode due to optical feedback induce a modification of the refractive index, which in turn leads to a change in the lasing frequency [42].

The desire to use semiconductor laser diodes in optical communication systems greatly motivated the great interest in their spectral and dynamical properties. For proper and adequate long-distance light propagation, low loss optical fibres are

used which require the light from the semiconductor laser diode to be properly coupled in. In 1978, Ikushima and Maeda showed that the back-reflected light into the laser from the optical fibre can lead to periodic peaks in the noise floor of the output power spectrum, with a frequency spacing dependent on the length of the fibre [43]. Furthermore, in 1979, Hirota and Suematsu [44] first demonstrated that optical feedback from optical fibres can increase the intensity noise of the semiconductor laser, which has a major effect on the performance of fibre-optic communication systems as it can limit the transmission distance and maximum possible bit rate [45]. Thus, many researchers have often considered optical feedback in laser diodes as a nuisance and an undesirable phenomenon.

On the contrary, other researchers realised the possible use of optical feedback in semiconductor laser diodes for many applications, which was first demonstrated in 1975 by Seko et al. who proposed to use the change in the laser output power due to optical feedback for data storage applications [46]. In 1976, Mitsuashi et al. proposed that the same could be achieved by monitoring the voltage across the laser junction [47]. More in-depth experiments were performed and theoretical models were proposed to determine the amplitude of the voltage change due to optical feedback by Burke et al. in 1978 [48] and Mitsuashi et al. in 1981 [49].

The awareness of the ability to use that optical feedback in semiconductor lasers for metrology applications was rising by this time. In 1980, Dandridge et al. first presented an acoustic laser diode sensor capable of detecting sinusoidal displacements as small as 90 μm [50]. Meanwhile, more properties of OFI were discovered in other types of lasers: in 1984, Churnside used optical feedback in a CO2 laser to measure velocity where he demonstrated an enhancement in the modulation depth near the lasing threshold [51, 52].

This sparked a wide interest in the use of OFI for instrumentation and sensing applications. In 1986, a velocity measurement was demonstrated using a laser diode by Shinohara et al. [53] where he pointed out the capability to obtain the interferometric signal by monitoring the voltage variations across the laser junction. In 1987, Shimizu observed that the target's direction of motion could be determined by examining the inclination of the power fringes [54]. A year later, Jentink et al. measured the velocity in a multi-mode laser diode, where they

demonstrated the periodicity of the OFI signal with the distance to the target [55]. In 1991, Koelink et al. first measured the flow rate of blood using a fibre-coupled laser diode subject to optical feedback, which signified the potential use of OFI in many medical applications [56]. Recently, It is has been shown in 2005 by Zakian et al. that the OFI technique can also be used to determine the size of scattering particles [57].

Another application is the absolute distance measurement. In the displacement measurement, the target is moving and the displacement of the target is determined by counting the fringes for a constant injection current. However in the absolute distance measurement both the sensor and the target are fixed, so the lasing frequency is modulated through the modulation of the injection current so to observe signal fringes with a periodicity related to the target distance. This technique was first proposed by Beheim and Fritsch in 1986 [58].

Since these first demonstrations, the OFI technique has been widely used in the measurements of displacement [59-63], absolute distance [64-68], velocity of solid bulky targets [69-73] and flow rates [74-78] using different types of lasers. More applications include a rudimentary parallel self-mixing imaging system to measure the speed and distance to different points on a rotating disk [79-83] as well as scanning based imaging systems such as: near field scanning optical microscopes [84-89], surface profiling [90-94], modal analysis and defect detection of metallic plates [95-97], and three-dimensional range imaging [98-102].

Considering the exposed historical and the current state of research achievements, the OFI sensing scheme can be considered as an active research domain with high potential to incursion on both industrial and laboratorial applications. In the next section, the theoretical principle of OFI technique is introduced followed by a brief description of some major OFI sensing applications.

1.2 Principle of the Optical Feedback Interferometry

The OFI sensing scheme, which is also widely known as self-mixing or self-mixing interferometry, occurs when a small portion of the optical power of the lasing source is back-reflected and coupled into the laser cavity. This back-scattered and time-delayed electromagnetic field interacts (or mixes) with the one of the cavity resulting in changes in the laser properties such as: threshold gain, lasing frequency and output optical power. These changes carry information about the remote target which can be extracted through appropriate signal processing.

A schematic illustration of the optical feedback interferometer is shown on the right side of Fig. 1.1, in comparison with a conventional Michelson interferometer. On one hand, all that is needed for an optical feedback interferometer is a laser diode as well as a collimating lens to focus the beam spot on the target surface. Some work has shown that the lens is not always necessary under certain conditions [103, 104]. Though not necessary, the monitoring photodiode that is already implemented inside the laser package is most common method used for the detection of the output power fluctuations due to OFI. On the other hand, additional optical components, such as: mirrors, splitters, isolators and etc., are necessary for the conventional interferometric system. Hence, the optical feedback interferometer is simpler, cheaper, self-aligned and more compact than the conventional interferometric techniques.

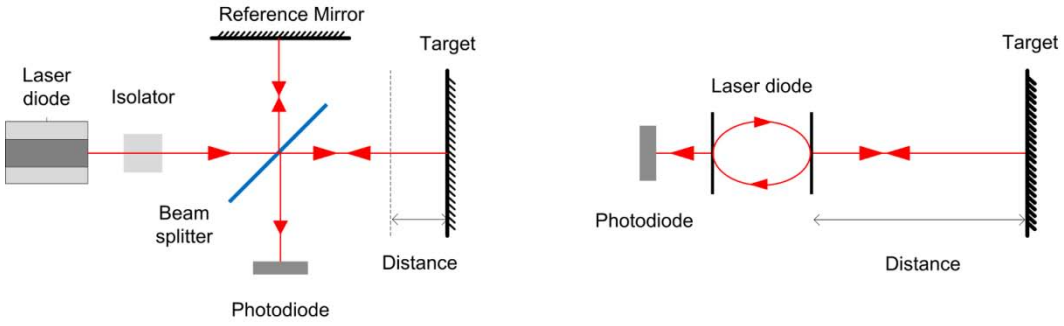

Fig. 1.1: A comparison between a conventional interferometer (left) and the OFI interferometer (right).

1.2 Principles of Optical Feedback Interferometry

In many commercial laser diodes, a monitoring photodiode is integrated inside the laser package to control the optical power emitted at the back facet, as shown in Fig. 1.2.

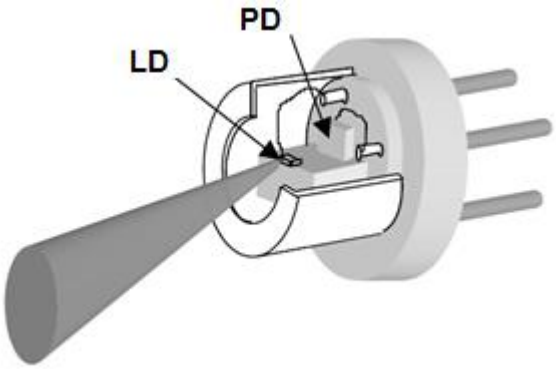

Fig. 1.2: A schematic diagram of a laser commercial package with a built-in monitoring photodiode.

However, optical feedback signals can still be obtained even without the monitoring photodiode by directly monitoring the voltage variations of the laser junction [60, 105]. This allows the deployment in OFI sensing of VCSEL based laser arrays where the integration of photodiodes is impractical [106], as well as the production of even smaller OFI sensors. Though, the signal-to-noise-ratio obtained from the voltage variations across the laser junction is usually lower than that obtained through the detection of the power variations [107].

A major difference between the optical feedback interferometers and the conventional interferometers is that the optical feedback interferences occur in an active medium with an imaginary refractive index whereas in conventional interferences are normally observed in free space, a passive medium. Therefore, the OFI sensor simultaneously acts as a power source, a micro-interferometer and as a light detector.

In order to further understand the subtleties of OFI, we consider the well documented model of coupled cavities, with the target as an external optical cavity. In this chapter we will present the rate equations of the laser diode subject to optical feedback based on those of the standalone laser diode that we will first present.

1.2.1 Model of Coupled Cavities

The standalone laser diode is simply modelled as a gain medium bounded by two mirrors. To account for the remote target and the subsequent optical feedback, a third mirror is added to the model resulting in what is called the three-mirror resonator.

1.2.1.1 Standalone laser diode

Due to its simple structure, the adopted model, shown in Fig. 1.3, is based on the Fabry-Pérot laser diode [108]. The laser diode is modelled as an active medium of effective refractive index of n_{eff} and length L, which is bounded by two mirrors with field reflection coefficients of r_1 and r_2 respectively for the rear mirror and the front mirror.

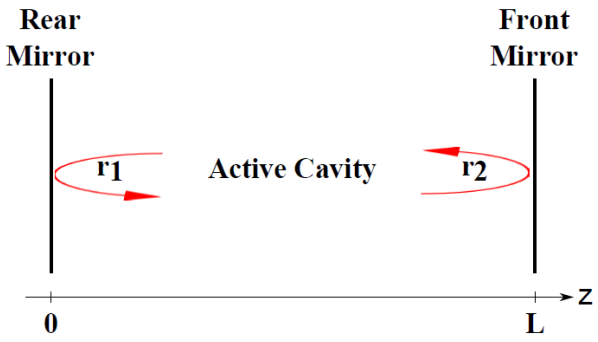

Fig. 1.3: A simple Fabry-Pérot model of the solitary laser diode.

The time-varying electric field inside the laser cavity at any point along the z-axis is given by:

$$E(z,t) = E_0 . e^{j\omega t} . e^{-j\beta z} \tag{1.1}$$

Where E_0 is the electric field amplitude, ω is the angular frequency, $\beta = \frac{2\,\pi\, n_{\text{eff}}}{\lambda}$ is the phase constant, where $\lambda = \frac{c}{\nu}$ is the wavelength of the electric field, ν is the lasing frequency, and c is the speed of light in vacuum.

The electric field propagating inside the laser cavity will encounter a gain as the active medium has a power gain per unit length of g. A power loss per unit length of α_s is assumed to account for the optical losses within the laser cavity.

Taking into account for the power gain and losses, the time-independent term of electric field, *E(z)*, from eq. (1.1) can be written as:

$$E(z) = E_0 . e^{0.5(g-\alpha_s)z} . e^{-j\beta z} \tag{1.2}$$

After a round-trip travel along the cavity, the electric field becomes:

$$E(z_{|_{2L}}) = r_1 . r_2 . E_0 . e^{(g-\alpha_s)L} . e^{-j2\beta L} \tag{1.3}$$

Stationary laser oscillation requires that the electric field faces no decay along its travel path. Hence, both amplitude and phase conditions for lasing must be satisfied. The amplitude condition requires that the gain over the round-trip compensates the total losses. On the other hand, the phase condition requires the round-trip phase within the laser cavity to be an integer multiple of *2π*. Both conditions could be written as:

$$r_1 . r_2 . e^{(g-\alpha_s)L} = 1 \tag{1.4a}$$

$$2\beta L = 2m\pi \tag{1.4b}$$

this expression can be simplified, yielding:

$$g_{\text{th}} = \alpha_s + \frac{1}{L} \ln(\frac{1}{r_1 r_2}) \tag{1.5a}$$

$$\lambda = \frac{2\, n_{\text{eff}}\, L}{m} \tag{1.5b}$$

where g_{th} is the threshold gain for the solitary laser diode.

In eq. (1.5a), the first term on the right hand side corresponds to the losses within the active cavity due to various factors such as: scattering and photon absorption. The second term corresponds to the losses due to light propagation out of the cavity through the partially reflecting mirrors.

In the following section, we extend our model by adding a third mirror in order to account for the remote target. Then, to simplify the analysis, the external cavity

(the one bounded by the front and the external mirrors) is replaced by an equivalent mirror, reducing the model to one similar to that of Fig. 1.3.

1.2.1.2 Laser diode subject to optical feedback

The model in Fig. 1.3 is extended by adding a third external mirror of an effective reflectivity r_{ext} at a distance L_{ext} from the front facet to account for back-reflection from a remote target [109-111]. The three-mirror model is shown in Fig. 1.4.

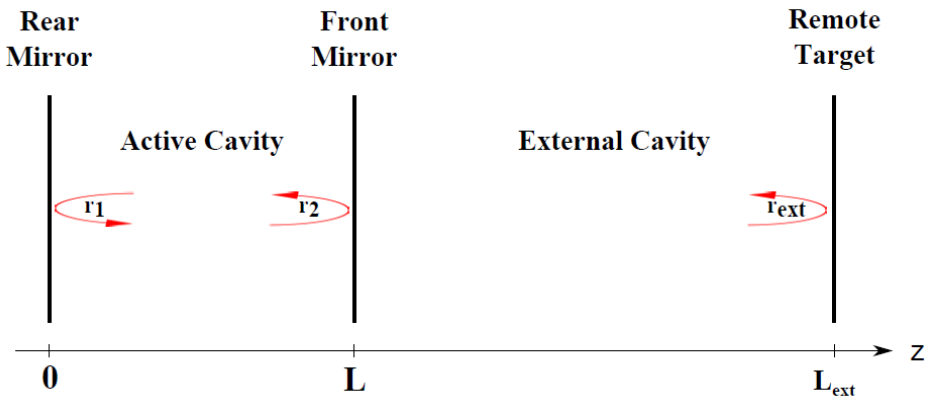

Fig. 1.4: The three-mirror model of a laser diode subject to optical feedback.

The back-scattered beam may be reflected from the front facet back towards the target in order to theoretically make multiple round trips before re-entering the active cavity [112-114]. This may be used for increasing the accuracy of displacement measurements as the number of fringes is doubled for a given amplitude of displacement. However, we limit our analysis to the case of a single reflection. Also, the models presented in this thesis are limited to the case of the single-mode operation of the laser source.

Assuming a single reflection from the remote target, the electric field at the boundary of the laser external front facet is the sum of the electric field reflected from it and the back-reflected field injected into the laser. This model can be reduced to one similar to that shown in Fig. 1.3 by replacing the external cavity with a single equivalent mirror, as shown in Fig. 1.5, with an electric field reflectivity of r_{eq}, given by:

$$r_{eq} = r_2 + (1 - |r_2|^2).r_{ext}.e^{-j\omega\tau_{ext}} \quad (1.6)$$

where $\tau_{ext} = \frac{2\,L_{ext}}{c}$ is the round-trip delay time in the external cavity, assuming a unity refractive index of the external medium.

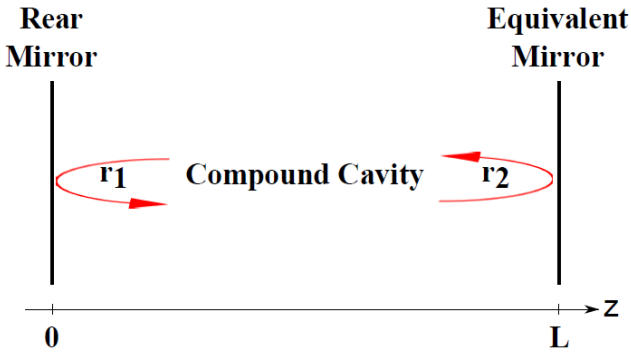

Fig. 1.5: The reduced model of a laser diode subject to optical feedback.

Eq. (1.6) can be rewritten as:

$$r_{eq} = r_2(1 + \kappa\, e^{-j\omega\tau_{ext}}) \quad (1.7)$$

where $\kappa = (1 - |r_2|^2)\frac{r_{ext}}{r_2}$ is the feedback coupling coefficient, which is a measure of the coupling strength between the external and active cavities. Eq. (1.7) can be written in a compact complex form:

$$r_{eq} = |r_{eq}|.e^{-j\phi_r} \quad (1.8)$$

where ϕ_r is the phase shift of the equivalent reflectivity. In most of the sensing applications, r_{ext} is very small compared to r_2, and $\kappa \ll 1$. Hence, the amplitude and phase shift can be expressed as:

$$|r_{eq}| = r_2(1 + \kappa\, cos(\omega.\tau_{ext})) \quad (1.9)$$

and

$$\phi_r = \kappa\, sin(\omega.\tau_{ext}) \quad (1.10)$$

To determine the amplitude and phase under stationary lasing conditions of a laser diode subject to optical feedback, r_2 in eq. (1.3) is replaced with r_{eq} yielding the amplitude condition:

$$r_1.\left|r_{\text{eq}}\right|.e^{(g-\alpha_s)L} = 1 \tag{1.11}$$

and the phase condition:

$$\frac{4\pi\nu n_{\text{eff}}L}{c} + \phi_r = 2m\pi \tag{1.12}$$

Eq.s (1.11) and (1.12) explicitly show that the presence of optical feedback leads to changes in the laser properties such as threshold gain, output power and lasing frequency. The threshold gain under optical feedback, g_c, is then expressed as:

$$g_c = \alpha_s + \frac{1}{L}\, ln(\frac{1}{r_1.\left|r_{\text{eq}}\right|}) \tag{1.13}$$

Replacing $|r_{eq}|$ with its equivalent expression in eq. (1.9), and expressing eq. (1.13) in terms of g_{th}, we obtain:

$$g_c = g_{\text{th}} - \frac{1}{L}\, ln(1 + \kappa\, cos(\omega.\tau_{\text{ext}})) \tag{1.14}$$

The change in threshold gain due to optical feedback, Δg defined as $\Delta g = g_c - g_{\text{th}}$, is then expressed as:

$$\Delta g = -\frac{\kappa}{L}\, cos(\omega.\tau_{\text{ext}}) \tag{1.15}$$

where the linear approximation: $\ln(1+x) \cong x$ if $x \ll 1$ is applied as $\kappa \ll 1$. Clearly, due to optical feedback, the gain changes periodically with the target distance, L_{ext}.

So far, we have demonstrated through equations (1.11) and (1.12) that, due to optical feedback, both threshold gain and emission frequency encounter changes. These changes lead to a change in the effective refractive index of the laser medium as it is a function of both frequency and gain. The gain change influence on the effective refractive index is indirect but occurs through the influence on the

carrier density within the laser cavity, N. The effective refractive index, threshold gain and carrier density are linked to each other through the expression [111]:

$$\frac{\partial n_{\text{eff}}}{\partial N}\,(N - N_{\text{th}}) = -\frac{\alpha c}{4\pi \nu_{\text{th}}}\,(g - g_{\text{th}}) \tag{1.16}$$

where N_{th} is the threshold carrier and α is the linewidth enhancement factor.

Eq. (1.12) of the phase condition is only satisfied when the round-trip phase within the compound cavity, ϕ_L, is an integer multiple of 2π. In other words, the round-trip phase change due to optical feedback should be zero to meet the phase condition. The phase change can be expressed as:

$$\Delta\phi_L = \frac{4\pi\Delta(\nu.n_{\text{eff}})L}{c} + \phi_r \tag{1.17}$$

The total change in the product of frequency and effective refractive index due to optical feedback is given by:

$$\Delta(\nu.n_{\text{eff}}) = \nu_{\text{th}}.\Delta n_{\text{eff}} + n_{\text{eff,th}}.\Delta\nu \tag{1.18}$$

where $\Delta\nu = \nu - \nu_{\text{th}}$ is the deviation from the lasing frequency of the solitary laser diode, ν_{th}, and $\Delta n_{\text{eff}} = n_{\text{eff}} - n_{\text{eff,th}}$ is the deviation from the effective refractive index of the active medium within the solitary laser diode, $n_{\text{eff,th}}$.

In eq. (1.17), the first term on the right hand side rises from the change induced by optical feedback on both the lasing frequency and the effective refractive index. The second term is the phase shift in the external cavity.

The effective refractive index is a function of both frequency and carrier density. Therefore, the change in the effective refractive index can be expressed as [111]:

$$\Delta n_{\text{eff}} = \frac{\partial n_{\text{eff}}}{\partial N}\,(N - N_{\text{th}}) + \frac{\partial n_{\text{eff}}}{\partial \nu}\,(\nu - \nu_{\text{th}}) \tag{1.19}$$

From eq. (1.16) and eq. (1.19), eq. (1.18) can be expanded to:

$$\Delta(\nu.n_{\text{eff}}) = -\frac{\alpha c}{4\pi}(g_c - g_{\text{th}}) + \nu_{th}\frac{\partial n_{\text{eff}}}{\partial \nu}(\nu - \nu_{\text{th}}) + n_{\text{eff,th}}(\nu - \nu_{\text{th}}) \tag{1.20}$$

The effective group refractive index, n_g, defined as the ratio of the speed of light in vacuum to the group velocity in the medium, is expressed as [111]:

$$n_g = n_{\text{eff}} + \nu_{\text{th}}\frac{\partial n_{\text{eff}}}{\partial \nu} \tag{1.21}$$

Using eq. (1.21), eq. (1.20) can be simplified to:

$$\Delta(\nu.n_{\text{eff}}) = -\frac{\alpha c}{4\pi}(g_c - g_{\text{th}}) + n_g(\nu - \nu_{\text{th}}) \tag{1.22}$$

Substituting eq. (1.22) into eq. (1.17), the later can be rewritten as:

$$\Delta\varphi_L = -\alpha L(g_c - g_{\text{th}}) + \frac{4\pi n_g.L}{c}(\nu - \nu_{\text{th}}) + \varphi_r \tag{1.23}$$

Substituting the phase shift in the external cavity from eq. (1.10) and the threshold gain change from eq. (1.15) into eq. (1.23), the round-trip phase change becomes:

$$\Delta\varphi_L = \frac{4\pi n_g.L}{c}(\nu - \nu_{th}) + \kappa\,[\sin(\omega.\tau_{\text{ext}}) + \alpha.\cos(\omega.\tau_{\text{ext}})] \tag{1.24}$$

which can be expressed in a more compact form:

$$\Delta\varphi_L = \Delta\omega.\tau_L + \kappa\sqrt{1+\alpha^2}.\sin(\omega.\tau_{\text{ext}} + \tan^{-1}\alpha) \tag{1.25}$$

where $\Delta\omega$ is the change in angular lasing frequency due to optical feedback, ω_{th} is the angular lasing frequency of the solitary laser diode and $\tau_L = \frac{2\,n_{\text{eff}}L}{c}$ is the round-trip delay time inside the laser cavity.

The lasing frequency of the laser diode subject to optical feedback is determined by setting eq. (1.25) to zero for the phase condition to be satisfied. Thus, the lasing frequency under optical feedback can be expressed as:

$$\nu = \nu_{\text{th}} - \frac{C}{2\pi\tau_{\text{ext}}}\sin(\omega.\tau_{\text{ext}} + \tan^{-1}\alpha) \tag{1.26}$$

where *C* is the feedback parameter which is expressed as:

$$C = \frac{\tau_{\text{ext}}}{\tau_L}\kappa\sqrt{1+\alpha^2} \tag{1.27}$$

Eq. (1.27) shows that the dimensionless C parameter depends on the distance to the remote target as well as the quantity of light re-injected into the laser cavity. The stronger is the optical feedback, the higher is C.

1.2.1.3 Optical feedback Regimes

In order to determine the influence of the dimensionless feedback parameter C on the round-trip phase change, and hence the possible solutions of lasing frequencies under optical feedback, we re-express eq. (1.26) as:

$$\Delta\varphi_L = 2\pi\tau_{\text{ext}}(\nu - \nu_{th}) + C.\sin(\omega.\tau_{\text{ext}} + \tan^{-1}\alpha) \tag{1.28}$$

Fig. 1.6 shows the round-trip phase change simulated using MATLAB and plotted as a function of $\nu - \nu_{\text{th}}$ for different values of C. The number of possible solutions of lasing frequencies is determined by the number of the zero-crossings of the round-trip phase change. The standalone laser diode operates at the unperturbed lasing frequency which is determined by the zero-crossing of the linear blue solid line.

In the presence of optical feedback, the zero-crossing, and thus the lasing frequency, is shifted from the threshold frequency. The number of the possible lasing modes depends mainly on the value of the feedback parameter C.

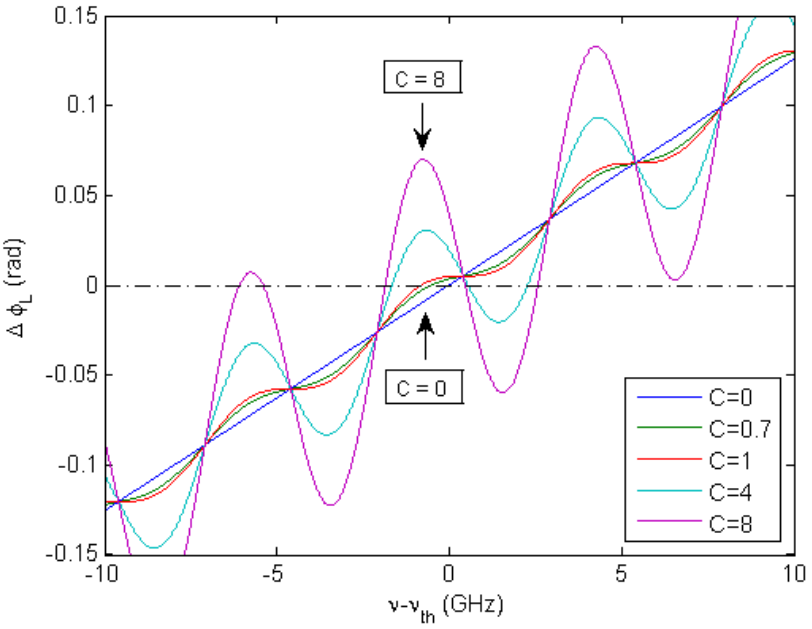

Fig. 1.6: The round-trip phase change against the lasing frequency change simulated for different values of the feedback parameter C.

As indicated in Fig. 1.6, for $C < 1$ which corresponds to weak optical feedback levels, the round-trip phase change increases monotonically with frequency yielding a single zero-crossing. Hence, the round-trip phase change has a single solution, and thus a single-mode operation. Since the purpose of the work presented in this thesis is to evaluate the laser parameters that impact the sensor sensitivity, we have limited our modelling to this range of C values.

For $C > 1$, the feedback is stronger and the round-trip phase is no longer monotonically increasing with frequency, rather it oscillates yielding multiple zero-crossings, which means multiple solutions. If the case of maximum three possible solutions is considered, the maximum value of C that satisfies this condition is calculated by solving eq. (1.28) and found to be 4.6 [115].

Indeed, for the values from $1 < C < 4.6$, the feedback is considered moderate, and the OFI signal assumes a saw-tooth like shape. The laser becomes bi-stable, and out of the three possible solutions: one is unstable while the other two are stable [116]. Even so, the laser diode still operates in single-mode as only the mode having the narrowest spectral width will be chosen by the laser diode [117-119], with the possibility of mode-hoping occurring.

For C > 4.6, the optical feedback level is considered strong and the system theoretically becomes multi-stable with mode-hopping as at least five solutions satisfying eq. (1.28). Very high values of C may lead to coherence collapse where the interferometric measurement is no longer possible.

Therefore, the number of the possible solutions of the round-trip phase change equation depends on the value of the feedback parameter C. Based on the number of solutions, the functioning of the laser can be divided into five regimes [120], as shown in Table 1.1 and Fig. 1.7:

Regime I	Weak optical feedback with (the feedback fraction of the amplitude is less than 0.01%). The linewidth of the lasing mode is narrow for weaker feedback levels and broadens with the increase of the feedback level.
Regime II	Moderate optical feedback (the feedback fraction of the amplitude is less than 0.1%). Generation of the external modes leads to mode hopping among internal and external modes.
Regime III	The feedback fraction of the amplitude is around 0.1%. The laser is perfectly single-mode and the spectral width is very narrow. Due to its narrow feedback ratio, this regime is difficult to obtain experimentally.
Regime IV	Strong optical feedback (the feedback fraction of the amplitude is around 1%). This is the coherence collapse regime which often is not appropriate for OFI sensing as the laser diode in this regime loses all its coherence properties and its linewidth is broadened greatly.
Regime V	Very strong optical feedback (the feedback fraction of the amplitude is higher than 10% feedback). The laser comes back to being single-mode with a very high rejection on the lateral modes of the laser cavity and exhibiting a very narrow spectral width. Because of the high instability of the laser diode in this regime, it is more suitable for chaos applications [121].

Table 1.1: The characteristics of the regimes of optical feedback levels.

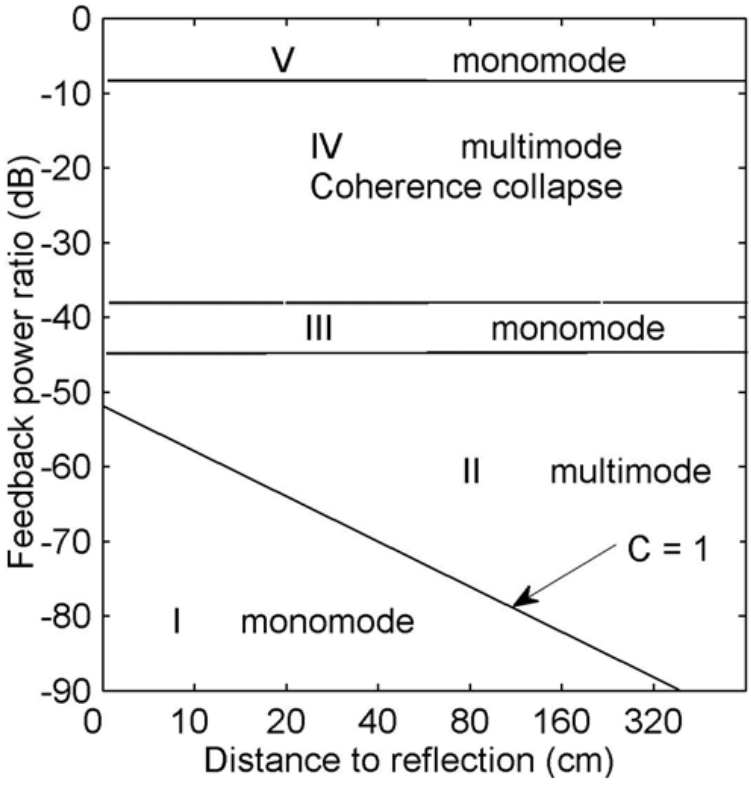

Fig. 1.7: The regimes of optical feedback levels at different power ratios.

1.3 Applications of Optical Feedback Interferometry

Optical feedback interferometry is a promising sensing technique for both industrial and laboratory environments due to its simple optical setup and cost-effectiveness compared to other interferometric techniques. Typical sensing applications of OFI are the measurement of displacement, absolute distance, vibration and velocity. Each of these applications fathers many sub-domain applications which are well covered by OFI literature, as the number of publications on OFI applications has been rapidly increasing since the early 1990s.

In this section, we briefly discuss the main typical sensing applications as well as two of the most recent OFI sensing applications: particle sizing and detection, and acoustics. We intentionally chose to discuss about those two applications because they all require high sensitivity, which is one of the goals of our work.

1.3.1 Typical sensing applications

Here, we present brief introductions of the main sensing applications that are widely covered in literature, namely the measurements of displacement, absolute distance, vibration and velocity.

a) Displacement:

The basic setup used in the measurement of the displacement of a moving target is shown in Fig. 1.8(a). When the target is moving along the optical path, the length of the external cavity is varying and so is the complex electric field reflectivity of the equivalent cavity. Those variations in the complex reflectivity affect the laser properties.

From eq. (1.15), we can see that the change in the gain due to optical feedback is periodic with a period of $\phi = \omega.\tau_{ext}$. Considering a full period swing in gain, we can evaluate the displacement in terms of wavelength by first evaluating the change in the external round-trip delay time due to displacement:

$$|\omega.\Delta\tau_{ext}| = 2\pi \tag{1.29}$$

where $\Delta\tau_{ext}$ is the change in the external round-trip delay time due to a target displacement of ΔD. Then, the target displacement due to a full swing can be expressed as:

$$|\Delta D| = \frac{\lambda}{2} \tag{1.30}$$

From eq. (1.30), we deduce that the resolution is in order of half of the operating wavelength. Actually, this resolution could be improved using several technical methods such as: the linearization of the normalized optical power that has been approximated by an ideal sawtooth signal [122], a fast modulation of the optical path difference of an OFI sensor that modifies the round-trip external delay [123], or the use of a pair of laser diodes, each with its own external cavity, where the first laser diode is used as a reference while the other is perturbed by the target displacement [124].

In addition, the resolution could also be improved using several signal processing techniques such as: the phase demodulation or un-wrapping method [125], the use

of extended Kalman filters [126], the use of wavelets transforms [127] or the use of genetic algorithms [128].

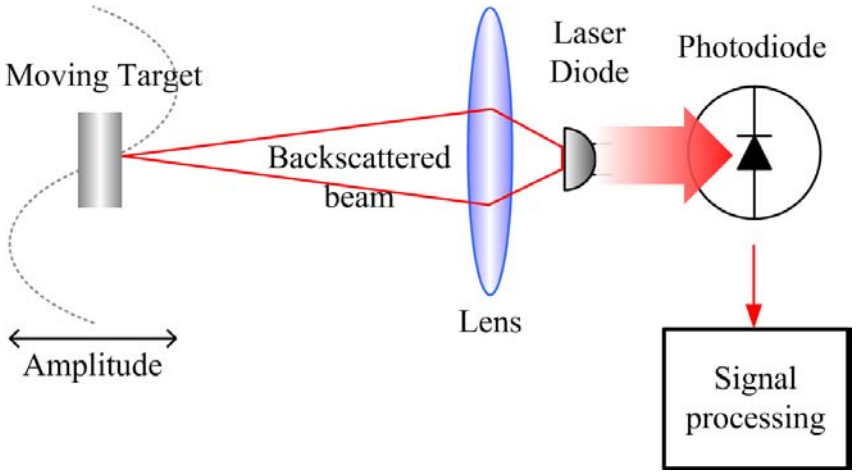

(a) Basic representation of the displacement measurement setup.

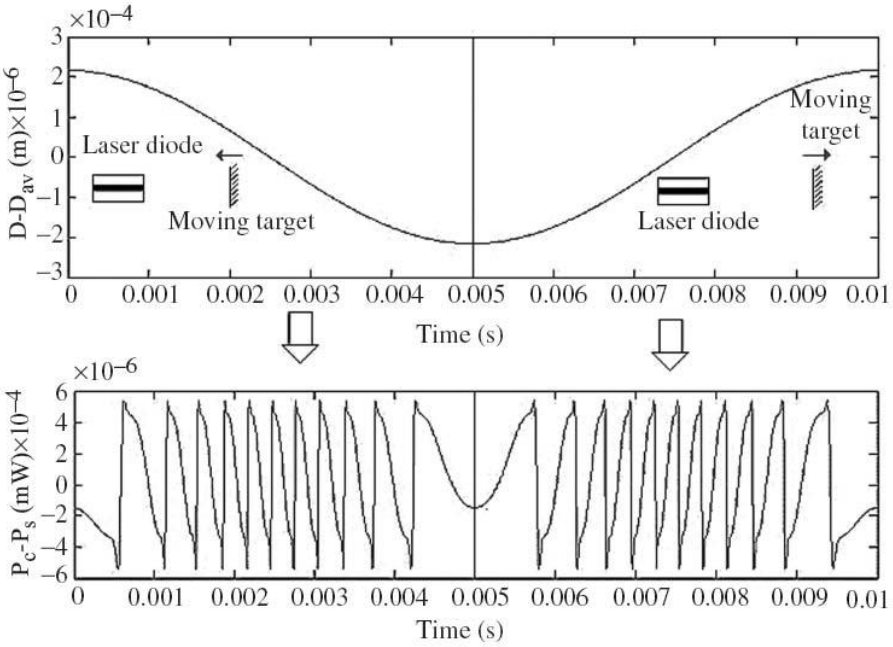

(b) A sinusoidal displacement with sawtooth-like fluctuations.

Fig. 1.8: The displacement of a target can be retrieved from processing the OFI signal acquired for a target moving along the optical path of a laser diode: (a) basic representation of the displacement measurement setup, and (b) a sinusoidal displacement with sawtooth-like fluctuations.

Fig. 1.8(b) shows a sawtooth-like modulation of an OFI signal corresponding to a sinusoidal displacement. We can observe that the number of sawtooth-like fringes

is directly proportional to the displacement. Moreover, the asymmetric shape of the fringes permits to directly recover the target direction of displacement.

By counting the fringes and adding them with their proper sign, we can retrieve the displacement with the basic resolution of $\lambda/2$. For example, if N fringes are detected for a motion in one direction, then the corresponding displacement D of the target is given by:

$$D = N \frac{\lambda}{2} \tag{1.31}$$

In comparison to a conventional system, the displacement can be retrieved using only the laser diode and a collimating lens to focus the beam spot on the target surface while conventionally the same information can be retrieved using two interferometric channels.

b) Vibration:

In many mechanical or mechatronic fields, vibration measurement is essentially demanded for the reduction or the elimination of the resultant vibration noise. In addition, it can be used for the quality control of the manufactured products to counter excessive vibration that may damage the product, limit processing speeds, or even cause catastrophic machine failure.

In 1996, Roos et al. first demonstrated the measurement of vibration using a laser diode OFI sensor [129]. Since then, many researchers concentrated their attention on this technique due to the low cost and compactness of the OFI sensor compared to conventional sensors. Other advantages include the high sensitivity, large bandwidth and a large dynamic range up to 70 kHz and 100 dB, respectively [130]. Moreover, it is able to function on different types of surfaces without any optical modulation as well it allows the measurement of low frequency vibrations. For example, the first sensor developed by Roos et al. allowed the measurement of vibrations in approximately all types of surfaces with a bandwidth ranging from 0.1 Hz to 70 KHz and a maximal peak to peak amplitude of 180 μm. A special algorithm was developed in order to analyse the OFI signal in real time which enabled the tracking of the target velocity variations.

In 2004, Scalise et al. used a laser diode OFI vibrometer in piezoelectric transducers characterization which measured both the velocities as well as the vibrations of solid targets with results comparable to those obtained by the conventional LDV by deploying a technique similar to the one used in LDV allowing the processing of the OFI signals even in the presence of speckle [69].

A more recent recovery technique of signals in an OFI vibrometer has been published in 2008 where the single beat frequency is extracted over a period containing a few fringes at least [131]. This method has allowed to rectify the problems of speckle, electromagnetic interference and mechanically induced parasitic signal fluctuations for an ultrasound solder vibrating at 20 kHz with an amplitude of 40μm.

c) Velocity:

The measurement of velocity is essentially desired in many areas like aerospace, automotive, metallurgy and paper industry, with an increasing demand for remote sensing of rough targets in hostile environments and in in-line assembly processes. Many techniques are used for the velocity measurements but either they have poor spatial definition like in ultrasonic sensors or they are expensive like in Laser Doppler Velocimetry (LDV). OFI sensors have the advantages of compactness, low cost and compatibility.

The main principle of this technique is based on Doppler-Fizeau effect. In the case of OFI velocimetry, either the laser diode or the remote target is static while the other is moving relatively. The Doppler frequency F_D that corresponds to the frequency of the sawtooth-like OFI signal can be expressed in terms of the velocity of the target V_F as:

$$F_D = \frac{2V_F}{\lambda} \tag{1.32}$$

Even when a target moves in a direction other than the propagation direction, the OFI sensor can still be used to measure the velocity of the target. In this case, we account for the angle that the direction of movement makes with the optical axis Θ to modify eq. (1.32) into:

$$F_D = \frac{2V_F}{\lambda} cos(\Theta) \tag{1.33}$$

An example of a measurement setup of rotating tilted targets is shown in Fig. 1.9(a) whereas Fig. 1.9(b) depicts an example of the electrical spectrum of the OFI velocimetric signal acquired for this setup.

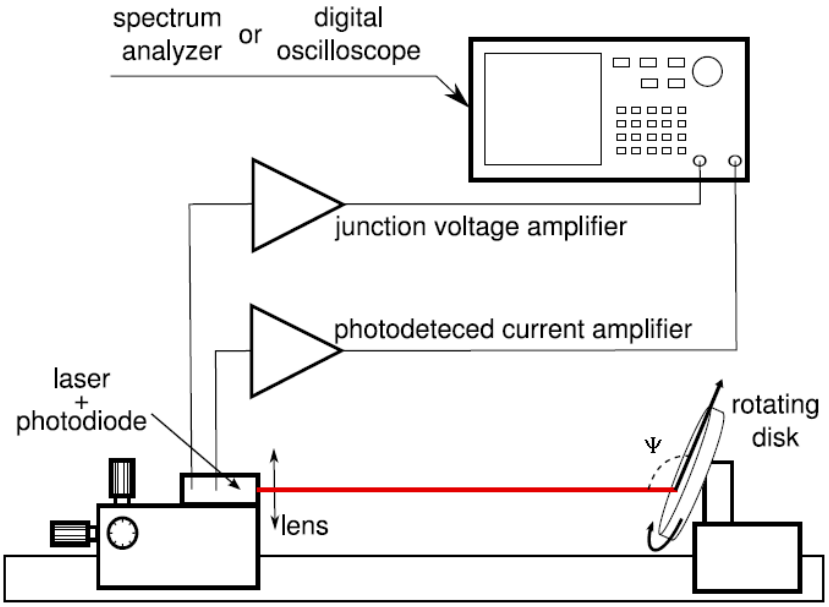

(a) Basic representation of the velocity measurement setup.

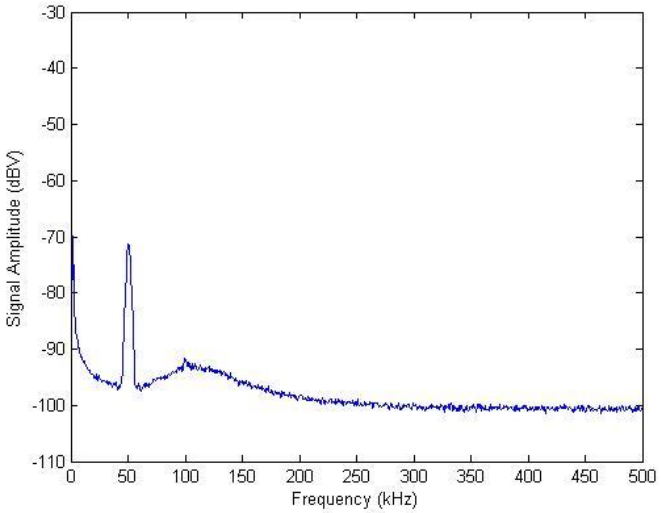

(b) Example of an OFI signal spectrum.

Fig. 1.9: Laser Doppler velocimetry demonstration with a VCSEL sensor: a) basic representation of the velocity measurement setup, and b) an OFI signal spectrum.

Recently, an on-board double-laser diode velocity sensor has been successfully tested by removing the influence of the pitching and the pumping effects in order to improve both the accuracy and the robustness of the OFI velocimetry system [132]. Furthermore, in order to improve the OFI velocimeter resolution by a factor of 10 when the Doppler frequency measurement was strongly affected by the roughness of the target surface, a second order auto-regressive algorithm has also been applied to the OFI signal [133]. In 2008, an OFI velocimeter based on a commercial 850nm VCSEL has been used for the measurement of velocity by acquiring and processing the LV OFI signal [107]. The velocimetry principle is also used for the measurement of flow rates in fluidics.

d) Absolute distance:

OFI sensors can also be used as range finder techniques besides the geometric technique of triangulation and the time-of-flight (TOF) technique [134]. The geometric technique of triangulation is widely used in industrial applications due to its low cost and robustness, yet it lacks the auto-alignment and has a limited distance-dependent sensitivity. The TOF technique, on the other hand, provides a long distance measurement coverage up to tens of kilometres with a uniform sensitivity throughout the whole measurement range, yet they are not the most accurate. The most accurate but very expensive approach is the interferometric technique which is mostly used in metrology when high accuracy is demanded. On the other hand, OFI sensors offer a low-cost and compact alternate solution.

In this configuration, the external cavity length is constant while the length of the active cavity is varying due to the continuous modulation of the laser injection current. As shown in Fig. 1.10, a properly shaped triangular waveform is used for the modulation of the current in order to enable the measurement of the absolute distance, inducing a triangular variation of $\Delta\lambda$ in the operating wavelength, corresponding to a variation of $(-2\pi\Delta\lambda/\lambda^2)$ in the wave number.

Variations of the output optical power P_F under optical feedback will then be superimposed on the output optical power of the solitary laser diode P_0 which corresponds to the triangular carrier as depicted in Fig. 1.10. By performing a

derivative of this OFI signal, characteristic spikes can be retrieved and digitalized for further signal processing to calculate the distance.

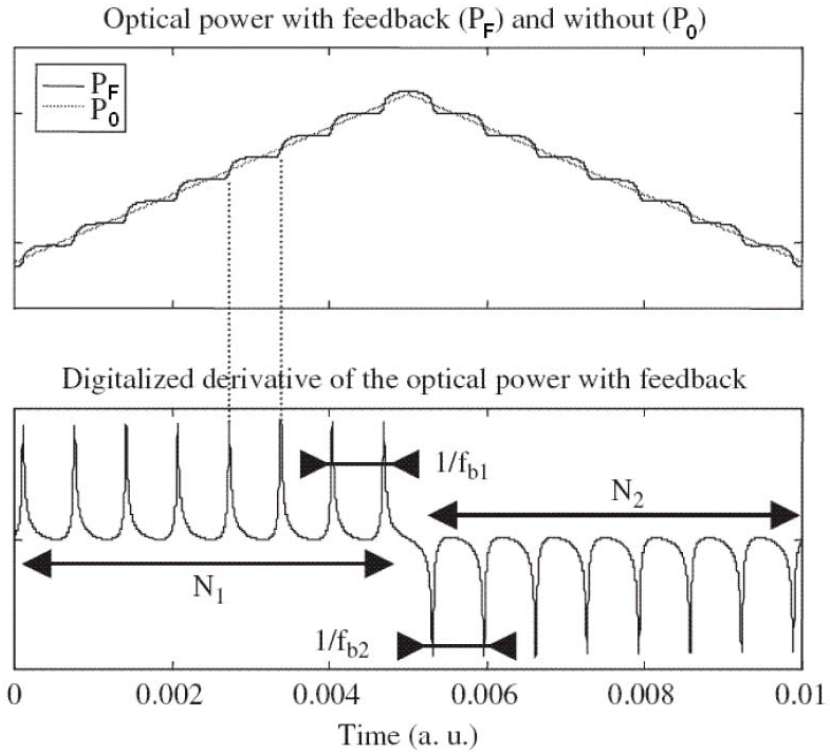

Fig. 1.10: Optical power variations and their corresponding beat frequencies for a triangular injection current.

The distance D was initially calculated by counting the integer number of those spikes. In more details, let us consider N_1 and N_2 as the number of spikes recorded during the increasing and decreasing triangular semi-period respectively as well as N as their sum in a complete period T_P of the modulating triangular signal. Then the distance can be approximately expressed as [135]:

$$D \approx \frac{\lambda^2}{2\Delta\lambda} N \simeq \frac{c}{2\Delta\nu} N \tag{1.34}$$

where $\Delta\nu$ the optical frequency shift.

The accuracy can be improved by determining the beat frequencies $f_{b,1}$ and $f_{b,2}$ between the spikes of the upward and downward triangular signal respectively, yielding the following exact relationship [109]:

$$D = \frac{c}{4\left(\frac{d\nu}{dt}\right)}(f_{b1} + f_{b2}) \simeq \frac{c.T_P}{8\Delta\nu}(f_{b1} + f_{b2}) \quad (1.35)$$

Theoretically, this method has zero error rising interest in the low cost and compact OFI sensor, but its experimental implementation is quite complicated. Moreover, beat frequencies of the produced spikes suffer from distortion due to thermal effects when the injection current is modulated at a frequency lower than 10 MHz [16].

1.3.2 High sensitive sensing applications

Here, we briefly discuss two of the most recent OFI sensing applications: particle sizing and acoustics.

a) Acoustics:

An interesting application of the OFI sensing to acoustics is the visualization of the propagating pressure or sound fields in transparent media. Possible applications include acoustic transducer design, hearing systems study or noise source identification.

Several techniques can be used to reconstruct the propagation of the acoustic fields such as microphone arrays [136] and shadowgraphy [137]. However, the microphone arrays can interfere with the field being measured, while the shadowgraphy, though it is capable of visualising the field, is unable to quantify its pressure. Also, laser Doppler vibrometry (LDV), an optical measurement technique, is used for the visualisation of the field propagation, but the sensing system is bulky and highly sensitive to mechanical perturbations [138].

One of the most recent OFI applications is the sensing of the acoustic field and its reconstruction as a 2D image by the direct measurement of the variation in the local pressure induced by the acoustic wave [139]. Like in all other OFI systems, the sensor is self-aligned, and the measurement setup (shown in Fig. 1.11) requires only a laser diode, a collimating lens and a light reflector. However, OFI is also sensitive to mechanical perturbations.

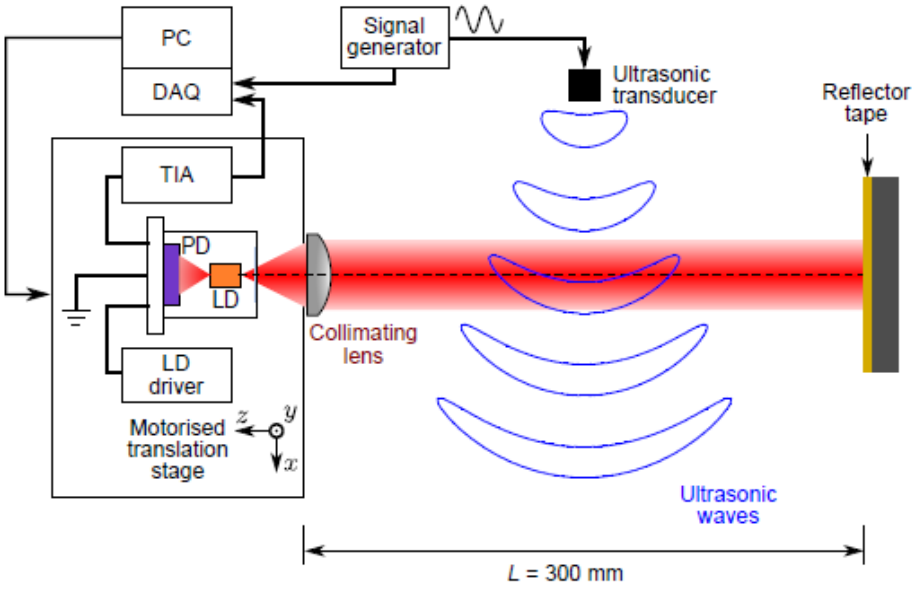

Fig. 1.11: A schematic diagram of the of the acoustic filed measurement setup [139].

Sound is produced through the mechanism of the compression wave propagation. The compression makes the propagating medium denser, changing its refractive index. The most common arrangement for interferometric systems to sense this change is shown in Fig. 1.11 and consists of a fixed light reflector as the remote target. The propagating acoustic wave then changes the index along the optical path between the target and the interferometer (the external cavity), allowing detection by LDV. Hence, replacing the LDV system by an OFI sensor enables pressure field visualisation.

Due to the continuous change in the refractive index of the external cavity, the external round-trip delay time τ_{ext} can be expressed as the sum of two terms: the constant part τ_0 which is the external round-trip delay time of the ambient refractive index n, and the variable part $\delta\tau$ resulting from the propagation medium compression. The variation $\delta\tau$ integrates the acoustic pressure change along the optical path. A 2D array of OFI signals is acquired by varying the spatial position of the laser in the plane perpendicular to the beam axis. OFI signals are then recorder over several periods of the acoustic wave and synchronized with the speaker exciting signal. Fig. 1.12 shows the image for a given time of the measured changes. The measured and simulated pressure fields agree almost perfectly.

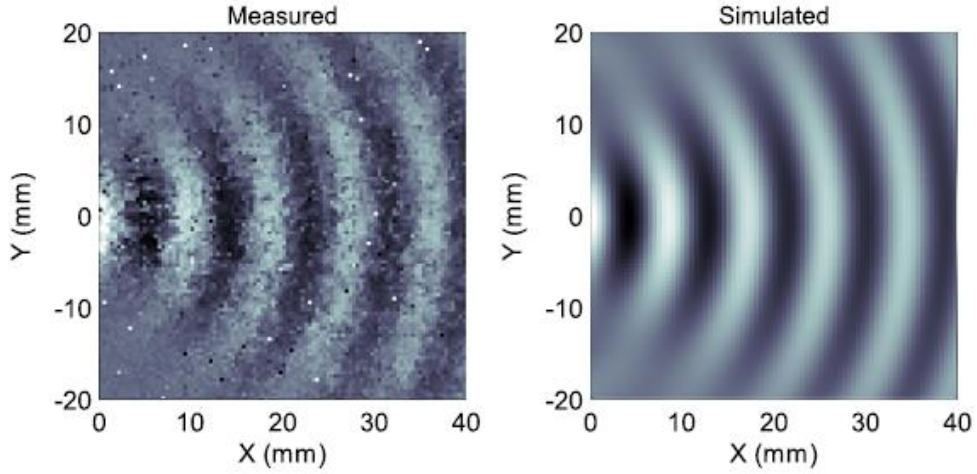

Fig. 1.12: Propagation of the acoustic field with the ultrasonic transmitter propagating the field into free space; Left: measured, Right: simulation [139].

It is very important to keep in mind that the integration of the changes in the refractive index over the length of the external cavity results in a very small change of the external round-trip time. Despite the strong power piezo actuator used for this experiment (~ 110 dB SPL), the OFI signal amplitude was about 10 times lower than the fringe amplitude which could be observed while moving the target in such conditions. The corresponding change in optical path length was λ/20. Thus a high sensitive OFI sensing system is required for these applications. Our analytical model provides the opportunity to optimize the system parameters and to choose the proper acquisition biasing in order to obtain the highest SNR.

b) Particle sizing and detection:

Like in acoustics, the detection in applications involving small targets such as particles in micro-fluidic channels is more challenging than solid targets, due to the weak backscattering of light from those small particles.

Flow measurements and particle sizing of particles with diameters as small as small as 20 nm were achieved using OFI sensors under the conditions of near-infrared wavelengths, short distances, and high particle density [140]. However, the detection range is limited to short distances for low density of particles due to the very weak optical feedback. Moreover, as high velocities require large detection bandwidth, the maximum detectable speed is also limited due to the increase of the system noise level with bandwidth [141]. Due to those reasons, the

detection of aerosol targets has mainly been achieved for a relatively high particle density, short operation ranges and limited target velocities [140, 142, 143].

A very recent work on particle detection in the air shows very promising results. About two orders of magnitude larger SNR was obtained through an edge-filter enhanced self-mixing interferometry (ESMI), which was achieved using an edge-filter that maps the laser frequency modulation (FM) into intensity modulation (IM) for wavelengths close to the steep edge of the absorption profile, allowing the detection of aerosol particles at lower optical feedback levels [144].

Velocity measurements of single micro-particles were firstly achieved using the ESMI approach in [145] using the setup shown in Fig. 1.13. Particles as small as 1 μm size were detected from a distance of 2.5 m while a detection range of 10 m was achieved for single particles of 10 μm in diameter.

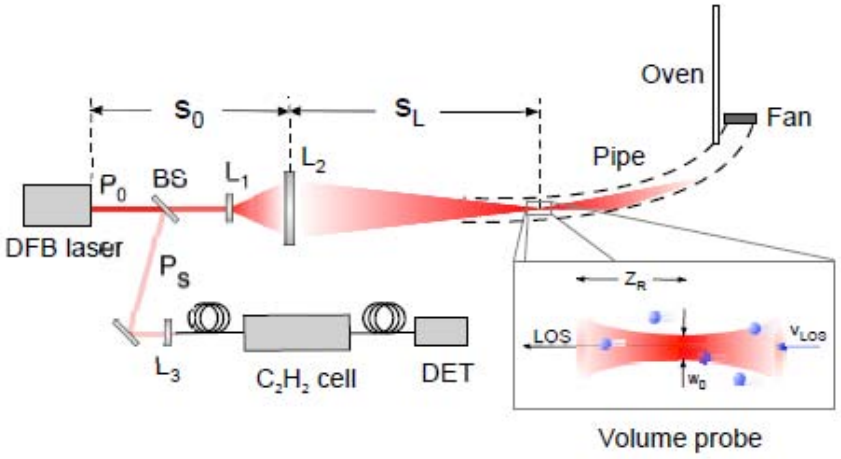

Fig. 1.13: Experimental setup for edge filter enhanced self-mixing interferometry (ESMI) experiments [145].

The advantages of OFI sensing technique as well as the high sensitivity of the ESMI method in particle sizing and detection is attractive in application areas that currently lack robust, inexpensive and self-aligned sensors. Furthermore, the optimization of the system parameters using our derived model to ensure the operation at the maximum SNR is advantageous for such a sensitive application.

1.4 Conclusion

The OFI sensing technique is widely deployed in industrial and laboratorial metrology fields such as the measurements of displacement, velocity, vibration and absolute distance. OFI sensors have the advantages of low cost, self-alignment and compactness over the other conventional interferometric techniques. In this chapter, we have briefly presented the history of optical feedback interferometry and the start of deploying this technique using semiconductor laser diodes in the major sensing applications. Later in this chapter, we have introduced the physical principles of the aforementioned sensing applications in more details.

As mentioned before, one of the main advantages of the OFI sensor is its compactness. In other words, there is no need for any additional optical components expect for the laser diode itself and a collimating lens. The fluctuations of the output optical power can be detected using the monitoring PD which is already implemented inside the laser package. Even when the monitoring PD is eliminated, either an external PD can be used for the detection of the power fluctuations from the front emission or the OFI signal can be detected by amplifying the variations in the voltage across the laser junction. Hence, we have three different sources for the acquisition of OFI signals.

In the aforementioned sensing applications, sensors with higher sensitivity provide more accurate measurements. Moreover, in order to achieve the best performance, it is essential to maintain the signal-to-noise ratio (SNR) at a maximum. One of the main goals of this thesis is to develop an analytical model of the different OFI signals that expresses their amplitudes in terms of the system parameters, and in particular the laser injection current, in order to determine the most influential parameters on the strengths of those signals. Another goal of this work is to determine the best biasing strategies required to achieve the optimal sensor sensitivity for the different OFI signal acquisition schemes.

Chapter 2

Modelling of Optical Feedback Interferometric Signals

The behaviour of the laser diode subject to optical feedback is a phenomenon of a great interest for many applications. For the analysis of this behaviour, either the compound cavity model introduced in the previous chapter or a model based on a set of rate equations that describe the rate of change in the complex electric field as well as the photon and the carrier densities can be used. The later model provides a greater insight and a better understanding of what happens within a laser diode system subject to optical feedback.

The optical feedback interferometric signals can be obtained from any of three different sources: the photodetection of the fluctuations in the output optical power from the front and the back facets of the laser diode, called the front and the back PD OFI signals respectively, or the amplification of the voltage variations in the laser junction, called the LV OFI signal.

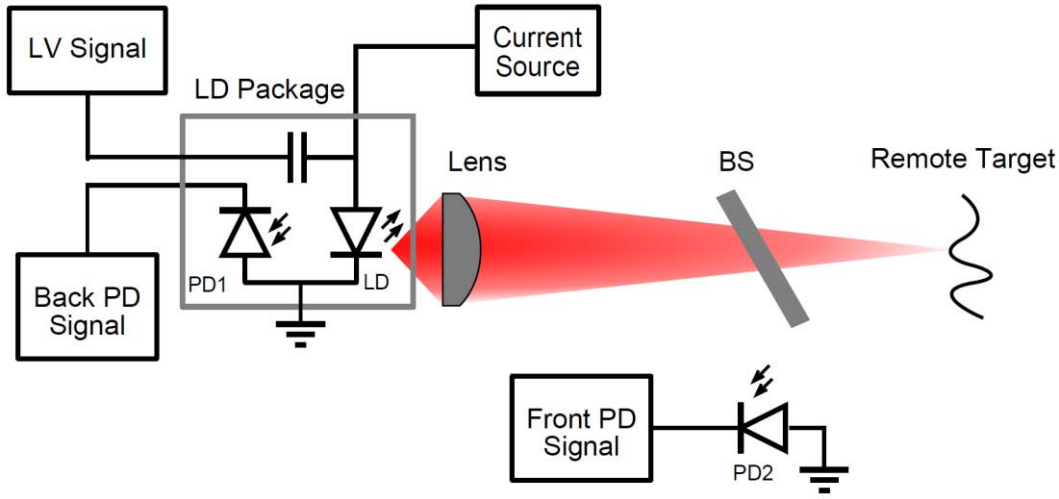

Fig. 2.1: A block diagram of the laser diode and the photodiodes.

Fig. 2.1 shows a block diagram of a laser diode subject to optical feedback with the three different sources of OFI signals indicated. The monitoring photodiode (denoted as *PD1* in Fig. 2.1), which is already integrated inside the laser package, is used in the detection of the back PD signal whereas an external photodiode (denoted as *PD2* in Fig. 2.1) is used to detect the front PD signal. For the front detection, a beam splitter is placed in the optical path between the laser diode and the remote target in order to reflect a fraction of the output optical power towards the external photodiode which is placed on one of its sides.

While the external PD signals require a more complex optical arrangement, it is usually discarded for in-plane laser-based OFI sensors. However, with VCSEL laser diodes, back facet PD is not possible and the monitoring PD is photodetecting the front facet power after reflection on the LD package window. Moreover, as will be demonstrated later in this manuscript, the front PD signal present interesting characteristics.

The demonstration of a simple analytical model that describes the evolution of each of these signals with the system parameters, and particularly the laser injection current, is the goal of this chapter. The derived model proposes an explanation to the experimentally observed divergent evolution of the PD and the LV signals with laser injection current.

The flowchart, shown in Fig 2.2, illustrates a brief description of the main steps undergone in order to derive the OFI model equations from the standard rate equations of the laser diode.

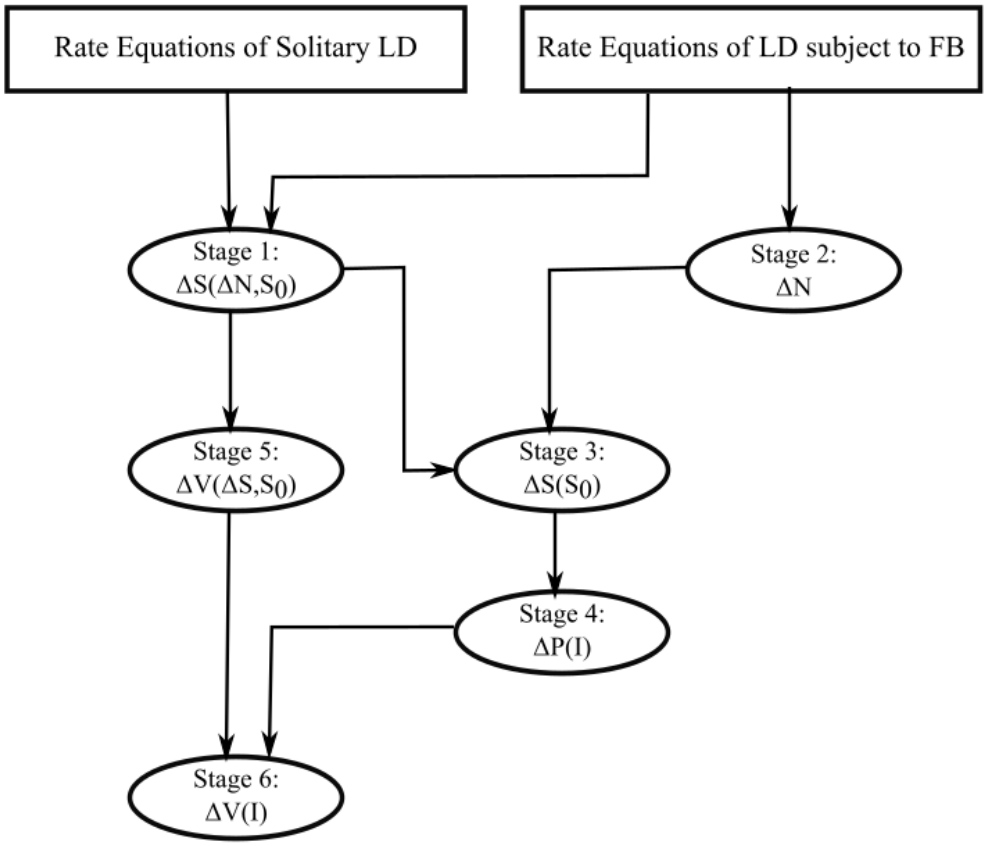

Fig. 2.2: Flowchart that illustrates the main stages undergone to derive the OFI model equations.

The derivation of the rate equations of the laser diode subject to optical feedback that we propose here is a long process and the flowchart in Fig. 2.2 to pave a simple path for the readers to follow during the derivation process shall be used.

The chapter is divided into three main parts. The first part is a re-demonstration of the OFI rate equations for a standalone laser diode and a laser diode subject to optical feedback. Those rate equations are then used to obtain the simple analytical model of PD and LV signals in the second part. The relationship between the photon and the carrier densities plays a major role in the evolution of both OFI signals. The last part focuses mainly on the Fabry-Pérot model and the electric field propagation equations. In this part, the ratio of the modulation indices is expressed as a function of the laser injection current.

2.1 Re-demonstration of OFI Rate Equations Model

As shown in the flow chart before, the derivation of the OFI signals equation model is based on the rate equations of the laser diode subject to optical feedback. In this section, we start the re-demonstration of those rate equations of the complex electric field as well as the photon and the carrier densities for the standalone laser diode since the analysis is way simpler than that of the laser diode subject to optical feedback.

In the previous chapter, we accounted for the optical feedback by replacing the front mirror of the standalone laser diode with an equivalent mirror, which is the combination of the remote target and the laser front mirror. The equivalent mirror had a complex reflection coefficient which was used in the analysis instead of the reflectivity of the front mirror. The same method is applied here to the rate equation model of laser diodes subject to optical feedback by replacing the front mirror real field reflectivity with the equivalent mirror complex reflectivity. Then, the rate equation is modified to account for the interference of the back-scattered electric field and the one within the active cavity.

2.1 Re-demonstration of the OFI Rate Equations Model

2.1.1 Standalone laser diode

We start with the simpler case of a solitary laser diode, where our analysis is based on the structure model of the laser diode introduced in the previous chapter. We modify the expression of the round-trip gain to account for the frequency-and-carrier-density dependent wave number. Thus, the round-trip gain is expressed as a product of frequency-dependent and frequency-independent terms. Once we consider this round-trip gain in the expression of a slowly-varying complex electric field after a round-trip in the laser cavity, the derivation of the rate equations proceeds thoroughly.

In fact, the rate equation of the slowly-varying complex electric field is split into a rate equation of the real electric field amplitude and into one of the electric field phase, while the rate equation of the photon density is derived directly using the expression of the slowly-varying complex electric field.

Considering the Fabry-Pérot model described in Fig. X (in the first chapter), the electric field, while travelling forth and back inside the laser cavity, experiences an amplification. The round-trip gain of the solitary laser diode, G_r, can be expressed as:

$$G_r = r_1 . r_2 . e^{(g-\alpha_s)L} . e^{-j2\beta L} \tag{2.1}$$

In eq. (2.1), β is the wave number of the propagating EM field, and is a function of the refractive index of the amplifying medium:

$$\beta = \frac{\omega}{c} . n_{\text{eff}} \tag{2.2}$$

In the steady state lasing regime, the gain should be unity in order to compensate for the losses within the active cavity. The laser being a complex imbricate system, any change in the laser parameter impacts the other parameters. In particular, the change in the amplifying medium effective refractive index is a function of both the lasing frequency and the carrier density, which relationship can be linearized as [111]:

$$\Delta n_{\text{eff}} = \frac{\partial n_{\text{eff}}}{\partial N}\,(N - N_{\text{th}}) + \frac{\partial n_{\text{eff}}}{\partial \nu}\,(\nu - \nu_{\text{th}}) \tag{2.3}$$

Substituting the change in the effective refractive index from eq. (2.3) into eq. (2.2), the frequency-dependent wave number can be expressed as [111]:

$$\beta = \frac{\omega_{\text{th}}}{c}.\left[n_{\text{eff,th}} + \frac{\partial n_{\text{eff}}}{\partial N}\,(N - N_{\text{th}}) + \frac{n_g}{\omega_{\text{th}}}\,(\omega - \omega_{\text{th}})\right] \tag{2.4}$$

where n_g is the effective group refractive index, which is defined, by taking in consideration the dispersion of the refractive index, as [111]:

$$n_{\text{g}} = n_{\text{eff}} + \nu\,\frac{\partial n_{\text{eff}}}{\partial \nu} \tag{2.5}$$

Hence, due to the dependence of the wave number to the effective refractive index, it also becomes sensitive to changes in the lasing frequency and the carrier density. Substituting eq. (2.4) into eq. (2.1), the later can be rewritten as:

$$G_r = r_1.r_2.e^{(g-\alpha_s)L}.e^{-j\frac{2\omega_{\text{th}}}{c}.\left[n_{\text{eff,th}}+\frac{\partial n_{\text{eff}}}{\partial N}(N-N_{\text{th}})+\frac{n_g}{\omega_{\text{th}}}(\omega-\omega_{\text{th}})\right].L} \tag{2.6}$$

This equation is important in that it links the round-trip gain to both the lasing frequency and the carrier density. In other words, the three parameters are interrelated, and a change in one of the parameters affects the other two.

Now, we simplify the form of the round-trip gain. The derived expression of the round-trip gain can be expressed as the product of two terms: a frequency independent term, G_1:

$$G_1 = |G_1|\,e^{-j\phi_G} \tag{2.7}$$

where

$$|G_1| = r_1.r_2.e^{(g-\alpha_s)L} \tag{2.8}$$

and

$$\phi_G = \frac{2\omega_{\text{th}}L}{c}.\left[\frac{\partial n_{\text{eff}}}{\partial N}\,(N - N_{\text{th}})\right] \tag{2.9}$$

as well as a frequency dependent term, G_2:

$$G_2 = e^{-j\frac{2\omega_{\text{th}}n_{\text{eff,th}}L}{c}}.e^{-j\frac{2n_gL}{c}(\omega-\omega_{\text{th}})} \tag{2.10}$$

Eq. (2.8) is simply the amplitude condition of lasing. The least gain required to overcome the total losses within the active cavity of the laser diode is unity. On the other hand, in eq. (2.10), when the phase lasing condition is satisfied, the argument of the first exponential function is an integer multiple of 2π, and the term is reduced to one. The first term of the argument of the second exponential function is equivalent to the round-trip time delay in the laser cavity, $\tau_L = \frac{2n_gL}{c}$. Thus, the frequency dependent gain can be simplified to:

$$G_2 = e^{-j(\omega-\omega_{\text{th}})\tau_L} \tag{2.11}$$

With this, we have expressed the round-trip gain as a product of two gains; one of them is frequency-dependent. Hence, assuming a slowly-varying complex electric field, the electric field after a round-trip in the laser cavity becomes:

$$E(t) = G_1G_2E(t) \tag{2.12}$$

Substituting the frequency dependent gain from eq. (2.11) into eq. (2.12), we get:

$$E(t) = G_1.e^{j\omega_{\text{th}}.\tau_L}.e^{-j\omega.\tau_L}.E(t) \tag{2.13}$$

The phase containing a term for the source frequency in the phasor domain is equivalent to a time shift in the time domain, a property from the time-frequency conversion properties. Thus, the $e^{-j\omega.\tau_L}.E(t)$ term in eq. (2.13) is equivalent to a time delayed slowly-varying complex electric field expressed as [111]:

$$E(t) = G_1E(t-\tau_L) \tag{2.14}$$

which is equivalent to the electric field one round-trip time before experiencing a gain of G_1. E(t) is a slowly-varying electric field, hence variations of the complex

amplitude are too small during a short round-trip delay, and the rate of change in the amplitude of the slowly-varying electric field can be expressed as [111]:

$$\frac{dE(t)}{dt} = \frac{E(t) - E(t - \tau_L)}{\tau_L} \tag{2.15}$$

The approximation is considered acceptable given the short internal round-trip delay time. Substituting the time-delayed electric field from eq. (2.14) into eq. (2.15), we get:

$$\frac{dE(t)}{dt} = \frac{1}{\tau_L}\left(1 - \frac{1}{G_1}\right)E(t) \tag{2.16}$$

In this equation, we express the change in the amplitude of the slowly-varying complex electric field as a function of the gain G_1 which can be developed from eq. (2.7) as:

$$\frac{1}{G_1} = e^{[\ln\left(\frac{1}{r_1.r_2}\right) - (g - \alpha_s) + j\phi_G]} \tag{2.17}$$

This expression can be simplified using linear approximation. In lasing conditions, the frequency independent gain is close to unity. This allows the usage of the linear approximation $e^x \approx 1 + x$ when $x \ll 0$. Hence, eq. (2.17) is reduced to:

$$\frac{1}{G_1} \approx 1 + ln\left(\frac{1}{r_1.r_2}\right) - (g - \alpha_s)L + j\phi_G \tag{2.18}$$

Substituting eq. (2.18) into eq. (2.16), the rate equation of the complex electric field becomes:

$$\frac{dE(t)}{dt} = \frac{1}{\tau_L}\left(-j\phi_G + (g - \alpha_s)L - ln\left(\frac{1}{r_1.r_2}\right)\right)E(t) \tag{2.19}$$

Hence, we end up with an expression for the change in the amplitude and the phase of the slowly-varying complex electric field. After simplification, this expression will be split into two rate equations; one for the change in the amplitude and the other for the change in the phase of the electric field.

We start by simplifying the imaginary part in the brackets. For that, first we should re-express the phase in eq. (2.9) in terms of the lasing frequency rather than the carrier density variations. The possible lasing angular frequencies are obtained from the phase condition for continuous emission derived in the previous chapter, and given by:

$$\omega = \frac{m\pi c}{n_{\text{eff}}.L} \tag{2.20}$$

If we consider the carrier density at the lasing threshold, eq. (2.20) becomes:

$$\omega_{\text{th}} = \frac{m\pi c}{n_{\text{eff,th}}.L} \tag{2.21}$$

As stated by eq. (2.3), a slight deviation in the carrier density leads to deviations in both the effective refractive index and the angular lasing frequency. Replacing the refractive index in eq. (2.20) by those in equations (2.3) and (2.21), we obtain a relationship between the carrier density variations and the angular frequency variation. This relationship is simplified using the effective group refractive index in eq. (2.5), yielding [111]:

$$\omega - \omega_{\text{th}} = -\frac{\omega_{\text{th}}}{n_g}\frac{\partial n_{\text{eff}}}{\partial N}(N - N_{\text{th}}) \tag{2.22}$$

Hence, the phase of the frequency independent gain, ϕ_G, can be simplified into a linear function of the angular frequency variation given as:

$$\phi_G = -(\omega - \omega_{\text{th}}).\tau_L \tag{2.23}$$

where the round-trip time delay in the laser cavity was used for the simplification of the expression. Substituting the simplified expression of the gain phase into eq. (2.18), we get:

$$\frac{dE(t)}{dt} = \left(j(\omega - \omega_{\text{th}}) + \frac{gL}{\tau_L} - \frac{\alpha_s L + ln\left(\frac{1}{r_1.r_2}\right)}{\tau_L} \right) E(t) \tag{2.24}$$

This expression of the complex electric field evolution consists of two terms: the first term in the right hand side corresponds to the phase change while the other two terms correspond to the electric field amplitude change. Furthermore, the last term in the brackets is half the photon lifetime, τ_p, which is a time constant indicative of the loss rate of photons in the cavity. It is defined as [111]:

$$\frac{1}{\tau_p} = \frac{c}{n_g}\left(\alpha_s + \frac{1}{L} ln\left(\frac{1}{r_1.r_2}\right)\right) \tag{2.25}$$

So far we have simplified the phase term in the brackets, and then we proceed to express the other two terms in as functions of photon lifetime and carrier density. The terms in the brackets of eq. (2.25) are the totals losses in the laser cavity and are equivalent to the threshold gain defined as:

$$g_{th} = \alpha_s + \frac{1}{L} \ln(\frac{1}{r_1 r_2}) \tag{2.26}$$

which should be attained for stationary lasing. Thus, eq. (2.25) can be re-expressed in term of the threshold gain as follows:

$$\frac{1}{\tau_p} = g_{\text{th}} \frac{c}{n_g} \tag{2.27}$$

Hence, eq. (2.24) can be simplified into [111]:

$$\frac{dE(t)}{dt} = \left[j(\omega - \omega_{\text{th}}) + \frac{1}{2}\left(g\frac{c}{n_g} - \frac{1}{\tau_p}\right)\right] E(t) \tag{2.28}$$

As mentioned before, the gain varies with the carrier density. Assuming a linear relationship as generally admitted for small variations, we could express the gain as [45]:

$$g\frac{c}{n_g} = G_n(N - N_{\text{tr}}) \tag{2.29}$$

where G_n is the differential gain coefficient and N_{tr} is the carrier density at transparency. Substituting this expression into the electric field rate equation from eq. (2.28), we get:

$$\frac{dE(t)}{dt} = \left[j(\omega - \omega_{\text{th}}) + \frac{1}{2}\left(G_n(N - N_{\text{tr}}) - \frac{1}{\tau_p} \right) \right] E(t) \tag{2.30}$$

As mentioned before, eq. (2.30) describes the rate of change in the amplitude and phase of the slowly-varying complex electric field. This expression is so important that it is used, directly or indirectly, to derive two out of the other three rate equations. As we will see later in this sub-section, the phase rate equation can be derived using the first term in the brackets. The photon density rate of change can be derived by linking the electric field to the output optical power and the photon density.

The purely real equation of the field amplitude is then expressed as:

$$\frac{dE(t)}{dt} = \frac{1}{2}\left(G_n(N - N_{\text{tr}}) - \frac{1}{\tau_p} \right) E(t) \tag{2.31}$$

Thus, we have derived the rate equation of the electric field amplitude. Then, we proceed to derive the phase rate of change, followed by those of the photon and the carrier densities. In order to derive those rate equations, the photon density and the output optical should be expressed as functions of the electric field, for us to be able to recall eq. (2.30).

The output power of the laser diode is proportional to both the photon density inside the active cavity, $P \propto S$, and the square of the complex electric field magnitude, $P \propto |E|^2$. In order to model the variations of the output power, we assume that the slowly-varying electric field is normalized so that the photon density is equal to the square of the electric field magnitude. Therefore, the photon density can be defined as [111]:

$$S(t) = E(t).E^*(t) = |E(t)|^2 \tag{2.32}$$

where E^* is the complex conjugate of the normalized complex electric field.

The slowly-varying normalized complex electric field can now be expressed in terms of the photon density as:

$$E(t) = \sqrt{S(t)}.e^{j\phi(t)} \tag{2.33}$$

where $\phi(t)$ is the phase of the slowly-varying normalized electric field. This relation allows us to directly derive the photon density rate equation, and thus the output optical power, using the previously derived electric field amplitude rate equation.

Squaring both sides of eq. (2.33) then taking the derivatives with respect to time, we end up with the following expression for the change in the phase of the slowly-varying normalized complex electric field:

$$\frac{d\phi(t)}{dt} = \frac{1}{S(t)}.-j\left(E(t).e^{-j\phi(t)}.\frac{dE(t)}{dt}\right) \tag{2.34}$$

which can be simplified into [111]:

$$\frac{d\phi(t)}{dt} = \frac{1}{S(t)}.Im\left\{E^*(t)\frac{dE(t)}{dt}\right\} \tag{2.35}$$

From eq. (2.30) and eq. (2.32), the phase variation in eq. (2.35) could be expressed as:

$$\frac{d\phi(t)}{dt} = \omega - \omega_{\text{th}} \tag{2.36}$$

Now, we need to replace the right hand term with a function of the threshold gain and the carrier density. As already stated in the previous chapter, the effective refractive index, the threshold gain and the carrier density are mutually interrelated through the following expression [111]:

$$\frac{\partial n_{\text{eff}}}{\partial N}\,(N - N_{\text{th}}) = -\frac{\alpha c}{4\pi\nu_{\text{th}}}\,(g - g_{\text{th}}) \tag{2.37}$$

Substituting eq. (2.37) into eq. (2.22), the change in lasing frequency could be linked to the change in gain through:

$$\nu - \nu_{\text{th}} = \frac{\alpha c}{4\pi n_g}\,(g - g_{\text{th}}) \tag{2.38}$$

All we have to do now is to combine equations (2.36) and (2.38). Then, the rate equation of the phase of the normalized slowly-varying complex electric field can be expressed in terms of the change in the gain through:

$$\frac{d\phi(t)}{dt} = \frac{1}{2}\alpha\left(G_n(N - N_{\text{tr}}) - \frac{1}{\tau_p}\right) \tag{2.39}$$

For a more compact form, the photon lifetime can be expressed in terms of the gain variation with carrier density by evaluating eq. (2.29) at threshold yielding:

$$\frac{1}{\tau_p} = G_n(N_{\text{th}} - N_{\text{tr}}) \tag{2.40}$$

Substituting this expression into eq. (2.39), the rate equation of the phase is simplified to [146]:

$$\frac{d\phi(t)}{dt} = \frac{1}{2}\alpha.\, G_n(N - N_{\text{th}}) \tag{2.41}$$

Here, we obtain our second rate equation, namely the phase rate equation. Then, we continue our analysis with the derivation of the photon and carrier photon densities.

For the photon density rate equation, once we recall eq. (2.32) which expresses the photon density as the square of the complex electric field magnitude, then it can easily be derived from the change rate of the normalized slowly-varying electric field through the following relation [111]:

$$\frac{dS(t)}{dt} = \frac{d\{E(t).E^*(t)\}}{dt} = E(t).\frac{dE^*(t)}{dt} + E^*(t).\frac{dE(t)}{dt} \tag{2.42}$$

Using the expression of the photon density in terms of the normalized complex electric field from eq. (2.32), and the expression of the change rate in the normalized slowly-varying complex electric field from eq. (2.30), we obtain:

$$\frac{dS(t)}{dt} = \left(G_n(N - N_{\text{tr}}) - \frac{1}{\tau_p}\right)S(t) \tag{2.43}$$

With this, we get our third rate equation, which was directly derived from the rate equation of the normalized slowly-varying complex electric field from eq. (2.30). In this equation, the first term in the brackets corresponds to the rate of stimulated emission while the second term corresponds to the rate of losing the photons inside the laser cavity. Expanding the brackets, we get:

$$\frac{dS(t)}{dt} = G_n(N - N_{\text{tr}})S(t) - \frac{S(t)}{\tau_p} \tag{2.44}$$

The fourth rate equation is that of the carrier density. This expression is not directly obtained from the other three rate equation. However, it is still quite easy to derive. The rate equation of the carrier density is expressed as [147]:

$$\frac{dN(t)}{dt} = \frac{I}{qV_a} - \frac{N(t)}{\tau_e} - G_n(N - N_{\text{tr}})S(t) \tag{2.45}$$

where I is the injection current, q is the electron charge, and V_a is the volume of the active cavity. The first term corresponds to the injection rate of carriers in the laser cavity by the current pump. The second term corresponds to the rate at which carriers are lost in the laser cavity due to non-radiative carrier recombination and spontaneous emission. The last term corresponds to the rate at which carriers recombine into photons due to stimulated emission.

So far, we have derived four rate equations for the standalone laser diode; the rate equations of the amplitude and the phase of the complex electric filed as well as the rate equations of the photon and the carrier densities. They are given as:

$$\frac{dE(t)}{dt} = \frac{1}{2}\left(G_n(N - N_{\text{tr}}) - \frac{1}{\tau_p}\right)E(t) \tag{2.46}$$

$$\frac{d\phi(t)}{dt} = \frac{1}{2}\alpha . G_n(N - N_{\text{th}}) \tag{2.47}$$

$$\frac{dS(t)}{dt} = G_n(N - N_{\text{tr}})S(t) - \frac{S(t)}{\tau_p} \tag{2.48}$$

$$\frac{dN(t)}{dt} = \frac{I}{qV_a} - \frac{N(t)}{\tau_e} - G_n(N - N_{\text{tr}})S(t) \tag{2.49}$$

These rate equations are extended in the following subsection to account for the presence of optical feedback. As shown in this subsection, once we obtain the rate equation of normalized slowly-varying complex electric field, deriving the other terms reduces to mere substitutions in pre-defined formulas.

In laser diodes subject to optical feedback, the derivation method is maintained the same, with the only difference being the consideration of a complex field reflection coefficient rather than the real field reflection coefficient of the front mirror.

2.1.2 Laser diode subject to optical feedback

In laser diodes subject to optical feedback, the external cavity is replaced by an equivalent mirror with a complex reflection coefficient. In this subsection, the complex reflection coefficient of the equivalent mirror is used for the analysis instead of the reflectivity of the front mirror. Then, we apply the same derivation method to obtain the rate equations of the complex electric filed, photon density and carrier density. These rate equations differ from the ones obtained before in that they account for the interference of the back-scattered electric field and the one within the active cavity.

In the previous chapter, the complex reflection coefficient was obtained from the analysis of the compound cavity model as:

$$r_{\text{eq}} = r_2(1 + \kappa\, e^{-j\omega\tau_{\text{ext}}}) \tag{2.50}$$

The field reflectivity of the front mirror in eq. (2.24) is then replaced by the complex one from eq. (2.50). This way, we modify eq. (2.24) to account for the optical feedback yielding the rate equation of the slowly-varying normalized complex electric field:

$$\frac{dE(t)}{dt} = \left(j(\omega - \omega_{\text{th}}) + \frac{gL}{\tau_L} - \frac{\alpha_s L + ln\left(\frac{1}{r_1.r_2}\right) - ln\left(1 + \kappa\, e^{-j\omega\tau_{\text{ext}}}\right)}{\tau_L} \right) E(t) \tag{2.51}$$

The first term in the brackets corresponds to the phase change while the second and third terms correspond to the amplitude change due to the round-trip within the active cavity. The last term in the brackets is due to optical feedback, i.e. the round-trip within the external cavity. It is simplified to $\frac{\kappa}{\tau_L} e^{-j\omega\tau_{\text{ext}}}$. This term results in a time-shifting of the normalized electric field. Hence, the rate of change in the slowly-varying normalized complex electric field under optical feedback can be expressed as [42]:

$$\frac{dE(t)}{dt} = \left(j(\omega - \omega_{\text{th}}) + G_n(N - N_{\text{tr}}) - \frac{1}{\tau_p} \right) E(t) + \frac{\kappa}{\tau_L} E(t - \tau_{\text{ext}}) e^{-j\omega\tau_{\text{ext}}} \tag{2.52}$$

This expression is the same as the one in eq. (2.30) except for the additional term that corresponds to the part of the back-reflected complex electric field which is re-injected into the laser cavity. As mentioned before in the previous subsection, the electric field *E(t)* is slowly-varying and the variations of the complex amplitude are too small, satisfying the approximation $E(t) \approx E(t - \tau_{ext})$.

This expression is used for the derivation of the rate equations of the amplitude and the phase of the electric field as well as the rate equation of the photon density. The real part of rate equation of the complex electric field is then obtained from eq. (2.52) as:

$$\frac{dE(t)}{dt} = \frac{1}{2}\left(G_n(N - N_{\text{tr}}) - \frac{1}{\tau_p} \right) E(t) + \frac{\kappa}{\tau_L} E(t - \tau_{\text{ext}}) cos(\omega.\tau_{\text{ext}}) \tag{2.53}$$

Then from eq. (2.52), we retrieve the rate equation of the phase by using the same derivation formula in eq. (2.35) thus leading to:

$$\frac{d\phi(t)}{dt} = \frac{1}{E(t)} \cdot \left((\omega - \omega_{\text{th}}) E(t) - \frac{\kappa}{\tau_L} E(t - \tau_{\text{ext}}) sin(\omega . \tau_{\text{ext}}) \right) \tag{2.54}$$

As equations (2.36) and (2.41) are equivalent, the rate equation of the phase can be simplified into [111]:

$$\frac{d\phi(t)}{dt} = \frac{1}{2} \alpha . G_n (N - N_{\text{th}}) - \frac{\kappa}{\tau_L} \frac{E(t - \tau_{\text{ext}})}{E(t)} sin(\omega . \tau_{\text{ext}}) \tag{2.55}$$

Comparing this expression to the one for the solitary laser diode, the effect of optical feedback is accounted for by the additional second term.

So far we have obtained the rate equations of the amplitude and the phase of the slowly-varying normalized complex electric field under optical feedback. Then, we proceed by using the rate equation of the complex electric field from eq. (2.52) to obtain that of the photon density through the same method as in the previous subsection.

The photon density rate equation can be easily retrieved using the same derivation formula in eq. (2.42) on the rate equation of the slowly-varying normalized electric field under optical feedback from eq. (2.52), yielding:

$$\begin{aligned} \frac{dS(t)}{dt} = & \left(G_n (N - N_{\text{tr}}) - \frac{1}{\tau_p} \right) S(t) \\ & + \frac{\kappa}{\tau_L} \sqrt{S(t) S(t - \tau_L)} \left(e^{j\omega\tau_{\text{ext}}} + e^{-j\omega\tau_{\text{ext}}} \right) \end{aligned} \tag{2.56}$$

The last term is reduced to a cosine using the formula $cos\,(\omega . \tau_{ext}) = 0.5\left(e^{j\omega\tau_{ext}} + e^{-j\omega\tau_{ext}}\right)$. Therefore, the rate equation of the photon density under optical feedback can be expressed as [111]:

$$\frac{dS(t)}{dt} = G_n (N - N_{\text{tr}}) S(t) - \frac{S(t)}{\tau_p} + \frac{2\kappa}{\tau_L} \sqrt{S(t) S(t - \tau_L)} \cos(\omega . \tau_{\text{ext}}) \tag{2.57}$$

Again, by comparing the photon density rate equation of a laser diode subject to optical feedback to that of a standalone laser diode, we observe an additional term that accounts for the optical feedback.

The last rate equation to be retrieved is that of the carrier density. Like the one obtained for the solitary laser diode, this one is obtained directly rather than by using that of the slowly-varying complex electric field. Thus, the rate of change in the carrier density remains unchanged and is expressed as:

$$\frac{dN(t)}{dt} = \frac{I}{qV_a} - \frac{N(t)}{\tau_e} - G_n(N - N_{\text{tr}})S(t) \tag{2.58}$$

This expression may look the same as the one in eq. (2.49). However, the carrier and photon densities are not the same anymore due to optical feedback.

In the previous sub-section, we derived the rate equations of the amplitude and the phase of the slowly-varying complex electric field as well as those of the carrier and photon densities. In this sub-section, we repeated the same derivation method, but for the laser diodes subjected to optical feedback. Here are the four derived rate equations:

$$\frac{dE(t)}{dt} = \frac{1}{2}\left(G_n(N - N_{\text{tr}}) - \frac{1}{\tau_p}\right)E(t) + \frac{\kappa}{\tau_L}E(t - \tau_{\text{ext}})cos(\omega.\tau_{\text{ext}}) \tag{2.59}$$

$$\frac{d\phi(t)}{dt} = \frac{1}{2}\alpha.G_n(N - N_{\text{th}}) - \frac{\kappa}{\tau_L}\frac{E(t - \tau_{\text{ext}})}{E(t)}sin(\omega.\tau_{\text{ext}}) \tag{2.60}$$

$$\frac{dS(t)}{dt} = G_n(N - N_{\text{tr}})S(t) - \frac{S(t)}{\tau_p} + \frac{2\kappa}{\tau_L}\sqrt{S(t)S(t - \tau_L)}\cos(\omega.\tau_{\text{ext}}) \tag{2.61}$$

$$\frac{dN(t)}{dt} = \frac{I}{qV_a} - \frac{N(t)}{\tau_e} - G_n(N - N_{\text{tr}})S(t) \tag{2.62}$$

Not all the four of the derived rate equations will be used in the derivation of the OFI signal model equations. The rate equations of the electric field amplitude and the carrier density are used in the next section to derive an expression for the evolution of the PD signal amplitude with injection current, while only the carrier

density rate equation is used to obtain an expression for the evolution of the LV signal with injection current.

In fact, the rate equation of the electric field amplitude is solved in the steady state to express the photon density variations in terms of those of the carrier density. This relationship is the basis for the derivation of both PD and LV model equations. We demonstrate that the PD and the LV OFI signals behave differently with the increment of laser injection current.

2.2 Amplitudes of LV and PD OFI signals

In the previous section, we derived the rate equations of the laser diode subject to optical feedback. In this section, we will develop, based on these rate equations, a simple analytical model that describes the evolution of the amplitudes of the different OFI signals with the laser injection current.

The OFI signals can be acquired by two different means: (i) by observing the fluctuations in the output power either through the monitoring photodiode usually displayed in front of the laser rear facet (denoted here as the rear PD signal) or through a photodiode that collects a part of the power emitted through the front facet of the laser (denoted here as the front PD signal) while using a beam splitter placed in the optical path between the front facet and the target, or (ii) by amplifying voltage variations across the laser terminals (denoted here as the LV signal). The latter is the only possible measurement approach when a monitoring photodiode is not included in the laser diode package and an external photodiode is not available. For both methods of signal acquisition, in order to achieve the best performance of the OFI sensor it is essential to maintain the signal-to-noise ratio (SNR) at a maximum. In this sub-section, we present an analytical model that describes the evolution of the OFI signals amplitudes with the injection current and the temperature.

2.2.1 Photodetected signal

Here, we will consider the case of a monitoring photodiode integrated inside the laser package. In other words, we only consider the power variations detected from the back facet of the laser diode. This way, we can derive a model equation for the back PD OFI signal amplitude, and then we can modify this equation to describe the evolution of the frontal PD OFI signal strength with laser injection current.

As mentioned before, only two rate equations are used here to derive an expression for the evolution of the PD signal amplitude with laser injection current: the rate equations of the electric field amplitude and the carrier density. By working out the steady state solution of the carrier density for the laser diode subject to optical feedback, we obtain an expression of the variations in photon density, ΔS, as a function of those in the carrier density, ΔN, and the unperturbed photon density S_0. Then, we obtain the steady state solution of the carrier density rate equation for the laser diode subject to optical feedback, where ΔN is expressed in terms of laser parameters. This leaves ΔS as a function of S_0 only. The PD signal equation is then obtained from this relation directly.

We have stated in the previous section that the output power of the laser diode is proportional to the photon density inside the active cavity, $P \propto S$. Hence, the relationship between the photon density variations and the unperturbed photon density applies for the power variations and the output optical power as well. By the end of this chapter, we get an expression of the PD signal amplitude as a function of the laser injection current and the OFI system parameters.

Let's start by expressing the emitted power P_c under optical feedback in terms of the unperturbed power P_0 using the following relation [147]:

$$P_c = P_0(1 + m.cos(\omega.\tau_{\text{ext}})) \tag{2.63}$$

where m is the modulation index. Hence, the output power fluctuations amplitude, ΔP, can be expressed as:

$$\Delta P = m.P_0.cos(\omega.\tau_{\text{ext}}) \tag{2.64}$$

However, as the output optical power can be expressed in terms of the photon density as [147]:

$$P = \frac{\hbar\omega V_a}{\tau_p} S \tag{2.65}$$

where $\hbar$ is the reduced Planck's constant.

Expression (2.64) can be applied to the photon densities, yielding:

$$\Delta S = m.S_0.cos(\omega.\tau_{\text{ext}}) \tag{2.66}$$

Therefore, if we can express the photon density variations in terms of the unperturbed photon density, the modulation index can be obtained, and thus an expression of the PD signal amplitude can be derived.

We start by solving the rate equations of the carrier densities for the solitary laser diode, eq. (2.49), and for the laser diode subject to optical feedback, eq. (2.62), in the steady state respectively:

$$\frac{I}{qV_a} = \frac{N_{\text{th}}}{\tau_e} + G_n(N_{\text{th}} - N_{\text{tr}})S_0 \tag{2.67}$$

$$\frac{I}{qV_a} = \frac{N_{\text{c}}}{\tau_e} + G_n(N_{\text{c}} - N_{\text{tr}})S_c \tag{2.68}$$

where $N_c = N_{\text{th}} + \Delta N$ is the carrier density of the laser diode subject to optical feedback at threshold, and $S_c = S_0 + \Delta N$ is the photon density of the laser diode subject to optical feedback at threshold. The last term in the right hand of eq. (2.68) can be expanded into two terms as follows:

$$\frac{I}{qV_a} = \frac{N_{\text{c}}}{\tau_e} + G_n(N_{\text{c}} - N_{\text{th}})S_c + G_n(N_{\text{th}} - N_{\text{tr}})S_c \tag{2.69}$$

By subtracting eq. (2.67) from eq. (2.69), we get:

$$0 = \frac{N_{\text{c}} - N_{\text{th}}}{\tau_e} - G_n(N_{\text{c}} - N_{\text{th}})S_c - G_n(N_{\text{th}} - N_{\text{tr}})(S_c - S_0) \tag{2.70}$$

which could be simplified, by using eq. (2.40), into:

$$0 = \frac{\Delta N}{\tau_e} + G_n.\Delta N(S_0 + \Delta S) + \frac{\Delta S}{\tau_p} \tag{2.71}$$

The product of ΔS and ΔN is a second order term with a much lower magnitude compared to the other terms ($\Delta N < N_{\text{th}}\ and\ \Delta S < S_0$), which is neglected. Thus, eq. (2.71) becomes:

$$\Delta S = -\Delta N \frac{\tau_p}{\tau_e}(1 + G_n \tau_e S_0) \tag{2.72}$$

The variation in photon density is a function of that of the carrier density as well as the photon density of the standalone laser diode. This expression is labelled as the *first* stage in the flowchart of Fig. 2.2. The next step is to get rid of ΔN. Therefore, we evaluate the steady state solution of the electric field amplitude rate equation from eq. (2.59), which yields:

$$\Delta N = -\frac{2\kappa}{G_n \tau_L} cos(\omega.\tau_{\text{ext}}) \tag{2.73}$$

In eq. (2.73), which is labelled as the *second* stage in the flowchart, the change in the threshold carrier density due to the optical feedback is expressed in terms of the feedback and the gain coefficients. Substituting this expression into eq. (2.72), we get:

$$\Delta S = \frac{2\kappa}{G_n \tau_L} \frac{\tau_p}{\tau_e}(1 + G_n \tau_e S_0)\ cos(\omega.\tau_{\text{ext}}) \tag{2.74}$$

which can be further simplified into:

$$\Delta S = \frac{2\kappa\tau_p}{\tau_L}\left(1 + \frac{1}{G_n \tau_e S_0}\right) S_0.cos(\omega.\tau_{\text{ext}}) \tag{2.75}$$

which expresses the photon density variation in terms of the unperturbed photon density and the system parameters. This expression is labelled as the *third* stage in Fig. 2.2. By comparing this expression to the one in eq. (2.66), we deduce that [148]:

$$m = \frac{2\kappa\tau_p}{\tau_L}\left(1 + \frac{1}{G_n\tau_e S_0}\right) \tag{2.76}$$

We still can't use this form of the modulation index before replacing the unperturbed photon density term with injection current. That is to introduce the dependence of ΔP on the laser injection current. By solving eq. (2.49) at threshold when there is no emission, we get:

$$\frac{I_{\text{th}}}{qV_a} = \frac{N_{\text{th}}}{\tau_e} \tag{2.77}$$

Dividing eq. (2.77) by eq. (2.67), the ratio of injection current to threshold current can be expressed as a function of the photon density of the standalone laser diode:

$$\frac{I}{I_{\text{th}}} = 1 + \frac{\tau_e}{N_{\text{th}}}\, G_n(N_{\text{th}} - N_{\text{tr}})S_0 \tag{2.78}$$

This is done in order to re-express the term in brackets in eq. (2.76) in terms of laser injection current and carrier density. Hence, eq. (2.78) can be rearranged into:

$$G_n\tau_e S_0 = \left(\frac{N_{\text{th}}}{N_{\text{th}} - N_{\text{tr}}}\right)\left(\frac{I - I_{\text{th}}}{I_{\text{th}}}\right) \tag{2.79}$$

which can be used to re-express the modulation index as:

$$m = \frac{2\kappa\tau_p}{\tau_L}\left(1 + \left(\frac{N_{\text{th}} - N_{\text{tr}}}{N_{\text{th}}}\right)\left(\frac{I_{\text{th}}}{I - I_{\text{th}}}\right)\right) \tag{2.80}$$

or

$$m = \frac{2\kappa\tau_p}{\tau_L}\left(\frac{I - \frac{N_{\text{tr}}}{N_{\text{th}}}I_{\text{th}}}{I - I_{\text{th}}}\right) \tag{2.81}$$

which is an expression of the optical feedback modulation index in terms of the injection current, threshold current and injection current at transparency. At high injection currents, the second term becomes close to one and the modulation index

equation can be approximated by the first term only. By substituting the modulation index from eq. (2.81) into eq. (2.64) of the amplitude of power fluctuations due to optical feedback, ΔP, we get:

$$\Delta P = \frac{2\kappa\tau_p}{\tau_L}\left(\frac{I - \frac{N_{\mathrm{tr}}}{N_{\mathrm{th}}} I_{\mathrm{th}}}{I - I_{\mathrm{th}}}\right) P_0 \tag{2.82}$$

In this equation, the PD signal amplitude is a function of the laser injection current and the unperturbed output optical power. This expression needs further simplification by expressing the output unperturbed power as a function of injection current itself.

By combining eq. (2.67) and eq. (2.77), we can express the photon density of the standalone laser diode as a function of injection current as follows:

$$S_0 = \frac{\tau_p}{qV_a}(I - I_{\mathrm{th}}) \tag{2.83}$$

which if inserted in eq. (2.65), we get:

$$P_0 = \eta(I - I_{\mathrm{th}}) \tag{2.84}$$

where η is the laser diode slope efficiency, which is constant for an ideal laser diode. In practice, constant slope efficiency is impractical and the slope efficiency would be expressed as [147]:

$$\eta = \frac{\hbar\omega}{q}.\eta_{ex} \tag{2.85}$$

where η_{ex} is the external differential quantum efficiency, which is the product of the internal quantum efficiency and the ratio of the mirror losses to the total losses within the active cavity.

Substituting the power expression from eq. (2.84) into eq. (2.82) of the PD OFI signal amplitude, we end up with [149]:

$$\Delta P = \frac{2\kappa\tau_p}{\tau_L}\eta\left(I - \frac{N_{\mathrm{tr}}}{N_{\mathrm{th}}}I_{\mathrm{th}}\right) \tag{2.86}$$

Eq. (2.86), labelled as the *fourth* stage in Fig. 2.2, explicitly describes the PD signal changes with respect to the parameters of the OFI system, and in particular with the laser injection current. For an ideal laser diode, the slope efficiency is constant with regards to injection current changes. Hence, the PD signal is a linearly increasing function of the injection current, which means that the higher the injection current the higher the signal amplitude.

In practice, this quantity, ΔP, can't be measured directly. Usually, a photodetector in front of either facet of the laser diode is needed for the detection of the power fluctuations. However, just a small portion of the output optical power emitted by the laser diode is coupled into the monitoring photodiode. The ratio of the coupled power to the emitted power is called the coupling efficiency η_{coupl}.

Only the incident photons absorbed by the depletion region result in the generation of electron-hole pairs, and thus in a flow of the photocurrent when those pairs move away from the depletion region towards the opposite polarities.

The ratio of the photocurrent to the coupled power is called the responsivity, R_λ, and is defined as:

$$R_\lambda = \frac{I_{\mathrm{PD}}}{\eta_{\mathrm{coupl}}.P} \tag{2.87}$$

where I_{PD} is the photocurrent. From eq. (2.87), the photocurrent can be expressed as a function of the emitted optical power yielding:

$$I_{\mathrm{PD}} = \eta_{\mathrm{coupl}}.R_\lambda.P \tag{2.88}$$

From which, the variations in the photocurrent signal due to optical feedback can be expressed as:

$$\Delta I_{\mathrm{PD}} = \eta_{\mathrm{coupl}}.R_\lambda.\Delta P \tag{2.89}$$

Substituting the expression of the power variations due to optical feedback from eq. (2.86) into eq. (2.89), we get:

$$\Delta I_{\mathrm{PD}} = \eta_{\mathrm{coupl}}.R_{\lambda}.\frac{2\kappa\tau_p}{\tau_L}\eta\left(I - \frac{N_{\mathrm{tr}}}{N_{\mathrm{th}}}I_{\mathrm{th}}\right) \tag{2.90}$$

Hence, by obtaining the evolution of the photocurrents variations amplitude with the laser injection current, we can deduce the evolution of the power output fluctuations with laser injection current.

2.2.2 Voltage signal

In case of the inability to use a monitor photodiode to detect the fluctuations in the output optical power, we still can obtain an OFI signal by amplifying the voltage variations in the laser junction. In this subsection, we will derive a model equation that links the voltage variations amplitude to the bias current. The model is derived based on the derived rate equations in the previous section.

Here, we start by expressing the voltage variations in the laser junction as a function of the carrier density variations. To eliminate the carrier density term, we replace it by the photon density variations through the relationship derived in the previous subsection. That relationship was obtained by solving the rate equation of the carrier density of a laser diode subject to optical feedback in the steady state.

The junction voltage of the laser diode is related to the carrier density through [150]:

$$N = N_i.e^{\frac{qV}{2kT}} \tag{2.91}$$

where N_i is the intrinsic carrier density, k is Boltzmann's constant and T is the laser temperature in Kelvin. Any change in the carrier density leads to a corresponding change in the voltage across the laser junction, to which we refer as the LV OFI signal.

In the standalone laser, the threshold carrier density can be expressed in terms of junction voltage as:

$$N_{\text{th}} = N_i . e^{\frac{qV_{\text{th}}}{2kT}} \tag{2.92}$$

whereas, in the laser diode subject to optical feedback, the threshold carrier density is expressed as:

$$N_c = N_i . e^{\frac{q(V_{\text{th}}+\Delta V)}{2kT}} \tag{2.93}$$

where V_{th} is the threshold voltage and ΔV is the voltage variation. Then, the change in carrier density can be written as:

$$\Delta N = N_i . e^{\frac{qV_{\text{th}}}{2kT}} \left(e^{\frac{q\Delta V}{2kT}} - 1 \right) \tag{2.94}$$

The exponential function in the bracket is close to one. Hence, the change in carrier density can be approximated into the following linear relation:

$$\Delta N = \frac{q\Delta V}{2kT} . N_i . e^{\frac{qV_{\text{th}}}{2kT}} \tag{2.95}$$

which can be simplified using the expression of the threshold carrier density from eq. (2.92). The LV signal can then be expressed in terms of the carrier density change as follows [151]:

$$\Delta V = \frac{2kT}{qN_{\text{th}}} \Delta N \tag{2.96}$$

Due to optical feedback, the threshold values of carrier density and injection currents are changed. Then, we proceed to the next step which is expressing the carrier density variations as a function of the photon density variations.

In eq. (2.72), the photon density change is expressed in terms of the carrier density variations. Hence, we can get an expression of the carrier density variations in terms of the change in photon density as follows:

$$\Delta N = -\frac{\tau_e}{\tau_p} \left(\frac{\Delta S}{1 + G_n S_0 \tau_e} \right) \tag{2.97}$$

which is labelled as the *fifth* stage in Fig. 2.2. It can re-expressed in terms of injection current using eq. (2.79) as:

$$\Delta N = -\frac{\tau_e}{\tau_p}\Delta S\left(\frac{I_{\text{th}} - \frac{N_{\text{tr}}}{N_{\text{th}}}I_{\text{th}}}{I - \frac{N_{\text{tr}}}{N_{\text{th}}}I_{\text{th}}}\right) \tag{2.98}$$

Then, we have to replace ΔS by ΔP, which can be expressed as a function of laser injection current. The change in photon density is linked to the power variations through eq. (2.65). Hence, the change in carrier density can be written as a function of the PD signal yielding:

$$\Delta N = -\frac{\tau_e}{\hbar\omega V_a}\Delta P\left(\frac{I_{\text{th}} - \frac{N_{\text{tr}}}{N_{\text{th}}}I_{\text{th}}}{I - \frac{N_{\text{tr}}}{N_{\text{th}}}I_{\text{th}}}\right) \tag{2.99}$$

Substituting the expression of the PD signal from eq. (2.86), the change in carrier density is reduced to:

$$\Delta N = -\frac{\tau_e}{\hbar\omega V_a}\frac{2\kappa\tau_p}{\tau_L}\eta\left(I_{\text{th}} - \frac{N_{\text{tr}}}{N_{\text{th}}}I_{\text{th}}\right) \tag{2.100}$$

where the carrier density is mainly a function of injection current. Then, the LV signal can be expressed as:

$$\Delta V = -\frac{2kT}{qN_{th}}\frac{\tau_e}{\hbar\omega V_a}\frac{2\kappa\tau_p}{\tau_L}\eta\left(I_{\text{th}} - \frac{N_{\text{tr}}}{N_{\text{th}}}I_{\text{th}}\right) \tag{2.101}$$

By arranging the terms, eq. (2.101) becomes:

$$\Delta V = -\frac{4\kappa\tau_p}{\tau_L}\frac{kT}{\hbar\omega}\eta\left(\frac{I_{\text{th}}}{qV_a}\frac{\tau_e}{N_{\text{th}}}\right)\left(1 - \frac{N_{\text{tr}}}{N_{\text{th}}}\right) \tag{2.102}$$

From eqn. (2.77), the product of the terms in the brackets on the left equals one. Therefore, the expression of the LV signal is reduced to [149]:

$$\Delta V = -\frac{4\kappa\tau_p}{\tau_L}\frac{kT}{\hbar\omega}\eta\left(1-\frac{N_{\mathrm{tr}}}{N_{\mathrm{th}}}\right) \tag{2.103}$$

Equation (2.103), labelled as the *sixth* stage in Fig. 2.2, explicitly describes the LV signal changes with respect to the OFI system parameters. By comparing the expressions of the PD and LV signals, we can notice few major differences. The first noticeable difference is the negative sign in the LV signal expression which indicates that both signals are out of phase.

The second major difference is the absence of the injection current term in the LV signal expression. This means that for an ideal laser diode, the amplitude of LV signal doesn't depend on the injection current, unlike the amplitude of the PD signal which is linearly proportional to injection current. This difference in the behaviour and the evolution of both OFI signals amplitudes with injection current is shown in Fig. 2.3.

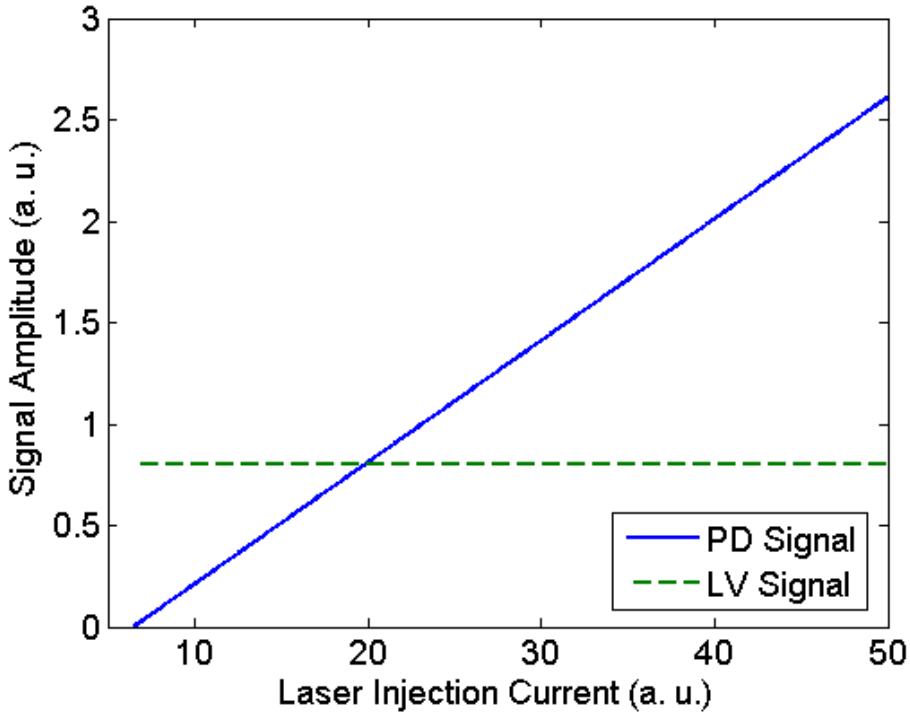

Fig. 2.3: Evolution of the PD and LV OFI Signals strengths with laser injection current.

The third major difference is the direct dependence of the LV signal amplitude on the temperature of the laser junction. For an ideal laser diode, the LV signal amplitude increases linearly with the increase of temperature while the PD signal

amplitude doesn't deepened on the operating temperature. Fig 2.4 shows the evolution of the amplitudes of both OFI signals with the operating temperature.

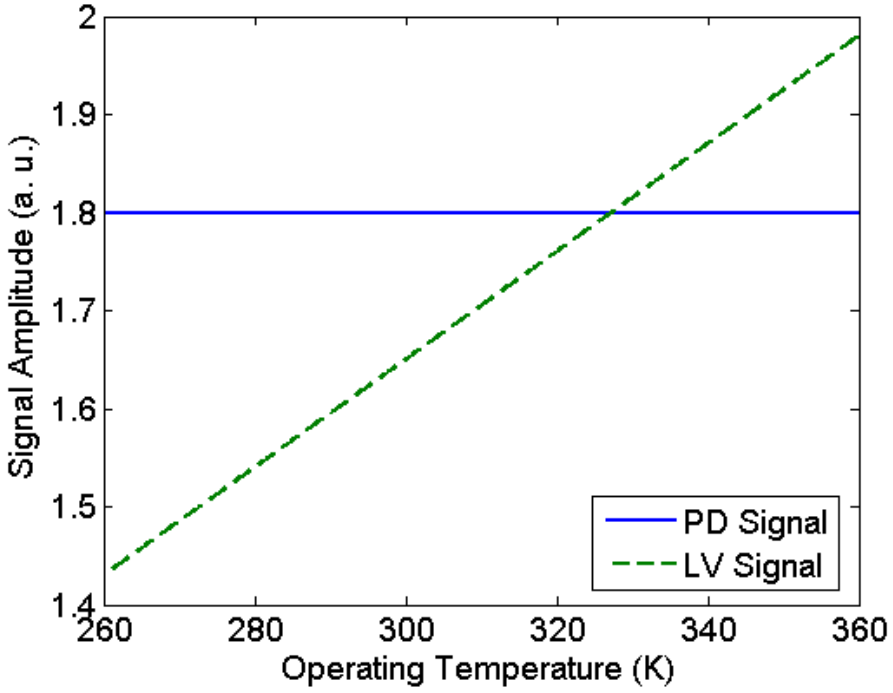

Fig. 2.4: Evolution of the PD and LV OFI Signals strengths with the operating temperature.

2.3 Analysis of the Front PD Signal

Either facet of the laser diode can be used for power detection. Usually, a photodiode is displayed in front of the rear facet to monitor the back emission. However, an external photodiode is needed for power detection when a monitoring photodiode is not included in the laser diode package. In this case, the external photodiode would be displayed on the side of a beam splitter that is placed in the optical path between the front facet and the target.

The rear and front PD signals are expected to have the same power modulation index as expressed in eq. (2.81). However, in the presence of a remote target, part of the back-reflected electric field, E_{ref}, is reflected from the front facet of the laser diode subjected to optical feedback back towards the target [152]. A schematic representation of the OFI configuration is shown in Fig. 2.5.

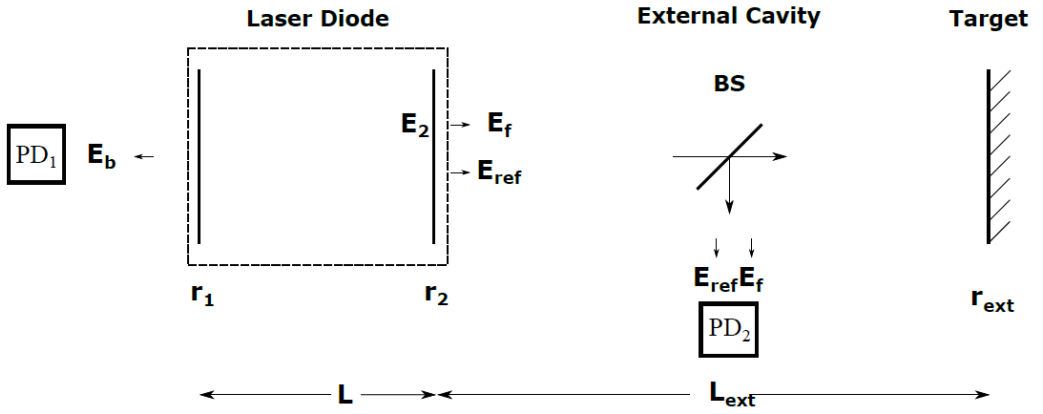

Fig. 2.5: A schematic representation of the back and front photodetection configuration.

Considering Fig. 2.5, the interferometric signals can be observed in two different positions: using the electric field that propagates from the active cavity through the rear facet and is acquired by the rear photodiode, E_b, and the electric field that propagates through the front facet, E_f, and is acquired by the front photodiode. For a standalone laser diode, the amplitudes of the electric fields can be expressed as:

$$E_{\mathrm{b0}} = E_0 . r_2 . e^{0.5(g-\alpha_s)L} . t_1 \tag{2.104}$$

$$E_{\mathrm{f0}} = E_0 . t_2 \tag{2.105}$$

where E_0 is the amplitude of the electric field assumed initially by the inner side of the front facet while t_1 and t_2 are the electric field transmission coefficients of the rear and front facets, respectively. E_{b0} can be simplified into:

$$E_{\mathrm{b0}} = E_0 . \sqrt{\frac{r_2}{r_1}} . t_1 \tag{2.106}$$

The steady state solution of eq. (2.77) in terms of the electric fields yields:

$${E_{\mathrm{x0}}}^2 = \frac{\tau_p}{qV} (I - I_{\mathrm{th}}) \tag{2.107}$$

where E_{x0} is the amplitude of the unperturbed electric field at either facet of the laser diode.

In the presence of a remote target, both E_f and E_{ref} are acquired by the front photodiode. Hence, the amplitudes of the electric fields can be expressed as:

$$E_b = E.\sqrt{\frac{r_2}{r_1}}.t_1 \tag{2.108}$$

$$E_f = E.t_2 - E.t_2.r_{\text{ext}}.r_2.cos\,(\omega.\tau_{\text{ext}}) \tag{2.109}$$

The negative sign of the second term in eq. (2.109) is due to the reflection from a denser medium into a less dense medium. Eq. (2.66) of the photon density under optical feedback is then solved in the steady state for the electric fields yielding:

$$E_x{}^2 = E_{\text{x0}}{}^2(1 + m.cos\,(\omega.\tau_{\text{ext}})) \tag{2.110}$$

where E_x is defined as:

$$E_{\text{x}} = E_{\text{x0}} + \Delta E_x \tag{2.111}$$

where the change in the electric field amplitude, ΔE, and $\Delta E_x \ll E_{\text{x0}}$. Expanding the squared terms in both sides of eq. (2.110) after substituting the terms of the electric fields from eq. (2.111), we obtain:

$$E_{\text{x0}}{}^2 + 2.E_{\text{x0}}.\Delta E_x + \Delta E_x{}^2 = E_{\text{x0}}{}^2(1 + m.cos(\omega.\tau_{\text{ext}})) \tag{2.112}$$

Cancelling the common terms on both sides and neglecting the last term on the left side, we end up with:

$$\Delta E_x = \frac{1}{2}.m.E_{\text{x0}}.cos(\omega.\tau_{\text{ext}}) \tag{2.113}$$

Substituting eq. (2.113) into eq. (2.108) and eq. (2.109), we get:

$$E_b = \left(E_0 + \frac{1}{2}.m.E_0.cos(\omega.\tau_{\text{ext}})\right).\sqrt{\frac{r_2}{r_1}}.t_1 \tag{2.114}$$

$$E_f = \left(E_0 + \frac{1}{2}.m.E_0.cos(\omega.\tau_{\text{ext}})\right).t_2(1 - r_{\text{ext}}.r_2.cos(\omega.\tau_{\text{ext}})) \tag{2.115}$$

which can be simplified into:

$$E_b = E_{\text{b0}}\left(1 + \frac{1}{2}.m.cos(\omega.\tau_{\text{ext}})\right) \tag{2.116}$$

$$E_f = E_{\text{f0}}\left(1 + \left(\frac{1}{2}.m - r_{ext}.r_2\right).cos(\omega.\tau_{\text{ext}})\right) \tag{2.117}$$

where the last term of the front facet electric field expression has been neglected. Then, the change in the electric fields can be written as:

$$\Delta E_b = \frac{1}{2}.m.cos(\omega.\tau_{\text{ext}}) \tag{2.118}$$

$$\Delta E_f = \left(\frac{1}{2}.m - r_{\text{ext}}.r_2\right).cos(\omega.\tau_{\text{ext}}) \tag{2.119}$$

The ratio of the front facet to the rear facet modulation indices of the electric fields, M_R, can now be expressed as:

$$M_R = \frac{\frac{1}{2}.m - r_{\text{ext}}.r_2}{\frac{1}{2}.m} \tag{2.120}$$

or

$$M_R = 1 - \frac{2.r_{\text{ext}}.r_2}{m} \tag{2.121}$$

Substituting the expression of the power modulation index from eq. (2.84) into eq. (2.121), we get:

$$M_R = 1 - \frac{\tau_L}{\tau_p}\frac{r_{ext}.r_2}{\kappa}\left(\frac{I - I_{th}}{I - \frac{N_{tr}}{N_{th}}I_{th}}\right) \tag{2.122}$$

Using the expression of the feedback coupling coefficient from eq. (2.21), eq. (2.122) can be simplified into [153]:

$$M_R = 1 - \frac{\tau_L}{\tau_p}\frac{R_2}{T_2}\left(\frac{I - I_{th}}{I - \frac{N_{tr}}{N_{th}}I_{th}}\right) \tag{2.123}$$

where R_2 and T_2 are the power reflection and transmission coefficients of the front facet, respectively.

Expression (2.123) explicitly describes the evolution of the modulation indices ratio with injection current. Fig. 2.6 shows the calculated ratio of modulation indices against laser injection current. Just above threshold, the ratio is positive, and then it gradually decreases with the increment of injection current until it becomes zero indicating no detection of the frontal PD signal. A further increment of the current leads to a negative ratio as the frontal PD signal changes sign. For high values of the injection current, the last term becomes close to one and the ratio becomes almost constant. Furthermore, the difference in the evolution of the normalised amplitudes of both PD signals with laser injection current is shown in Fig. 2.7.

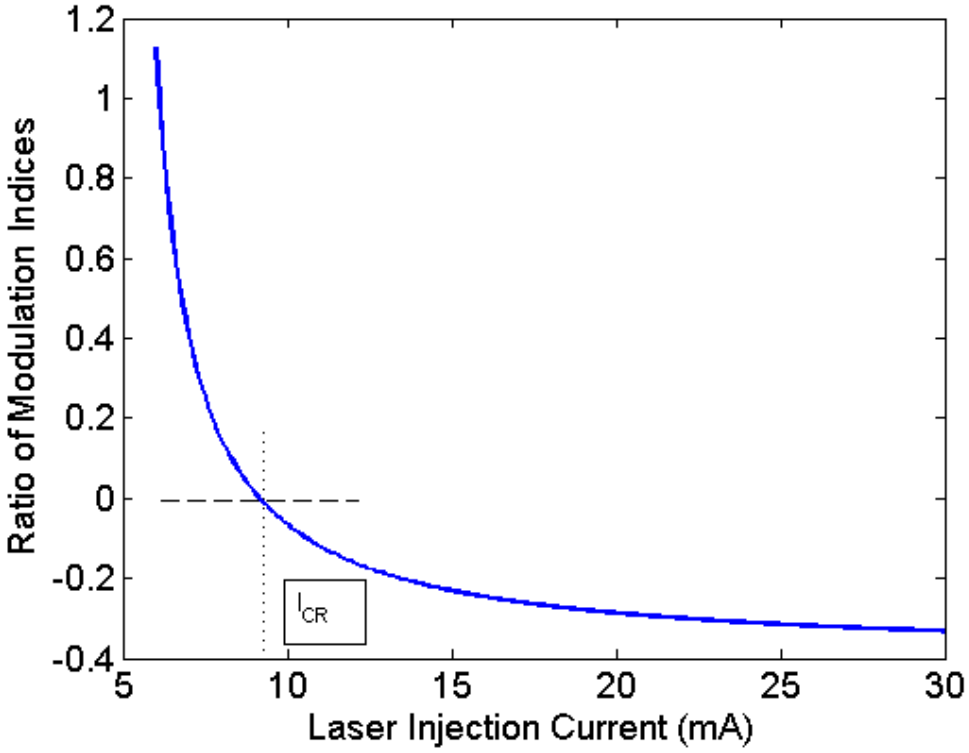

Fig. 2.6: The ratio of modulation indices as a function of injection current.

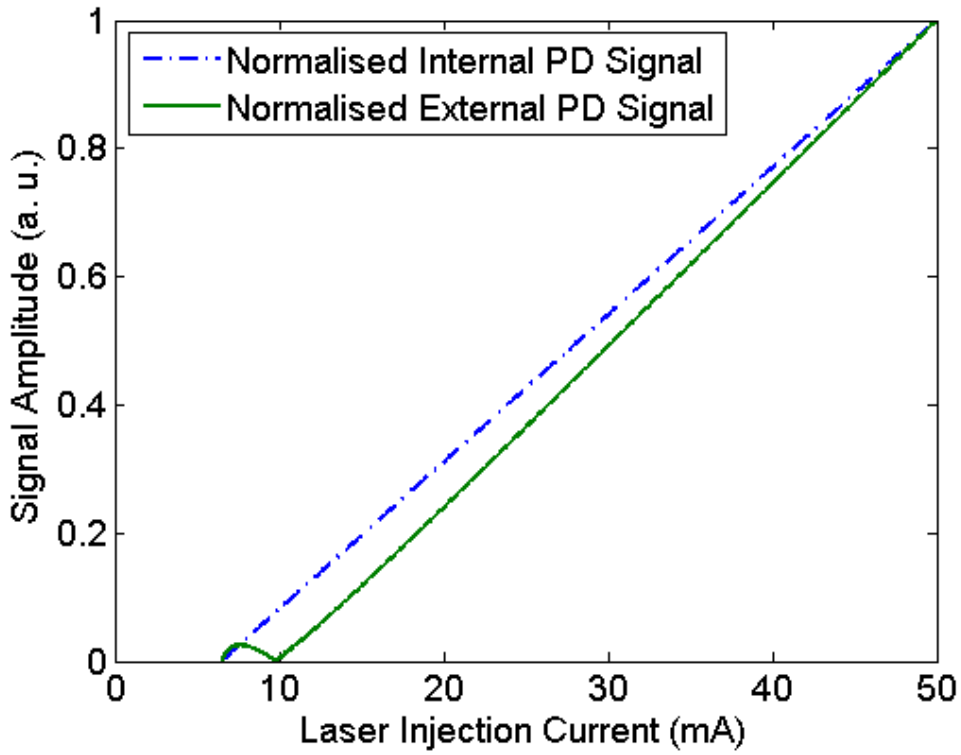

Fig. 2.7: Evolution of the front and the back PD signals normalised strengths with laser injection current.

2.4 Conclusion

In this chapter, we have introduced an analytical simple model to describe the evolution of the different OFI signals. The model equations are expressed as follows:

$$\Delta P_{\text{back}} = m.P_{0,\text{back}} \tag{2.124}$$

$$\Delta P_{\text{front}} = (m - 2.r_2.r_{\text{ext}}).P_{0,\text{front}} \tag{2.125}$$

$$\Delta V = -\frac{4\kappa\tau_p}{\tau_L}\frac{kT}{\hbar\omega}\eta\left(1 - \frac{N_{\text{tr}}}{N_{\text{th}}}\right) \tag{2.126}$$

The first two equations describe the back and the frontal PD signals, respectively, while the third equation describes the LV signal.

The model explains the experimentally observed phase relationship change from an in-phase to an out-of-phase relationship at some injection current, which we call the crossover current. The model also explains the inability to detect the frontal PD signals at this injection current. On the other hand, the model predicts a permanent out-of-phase relationship between the back PD and the LV signal.

Moreover, PD signals behave differently with the injection current from the LV signal. The LV signal is expected to remain constant, for constant slope efficiency as the injection current increases while the back PD signal is linearly increasing with the injection current. The frontal PD signal encounters a gradual increment followed by a gradual decrement then the signal vanishes at the crossover current, which is close to the threshold. With further increment of the injection current, the frontal PD signal will start increasing linearly with the injection current, exactly like the back PD signal.

Chapter 3

Experimental Validation of the OFI Signal Modelling

In the previous chapter, we have presented the theoretical background that describes through the rate equations model the behaviour of a laser diode in the presence of optical feedback. From these equations, we have derived an analytical model that describes the evolution of both the photodetected signals (Internal PD and External PD) and the laser voltage (LV) signals with the system intrinsic parameters and especially the laser injection current. For the sake of simplicity, this model describes the behaviour of a single-mode laser diode, however it is interesting to evaluate to what extent one could hope that it could be used to describe any type of laser diode under optical feedback.

In this chapter, we propose first to evaluate the validity of the model for two different types of laser diodes: a distributed feedback (DFB) laser and a vertical-cavity surface-emitting laser (VCSEL). Second we investigate the model pertinence in the case of multimode laser diodes: a transverse multimode VCSEL and a longitudinal multimode Fabry-Pérot type laser diode.

Experiments are performed over a large range of laser injection currents and operating temperatures in order to validate the major influence of these parameters on the OFI signals amplitudes that are predicted by the model.

3.1 Validation of the model for single-mode laser diodes

3.1.1 Description of the Experimental Setup

In order to experimentally validate the dependency of the OFI signals on injection current and temperature, we have performed a set of measurements at different injection currents and operating temperatures using the experimental setup shown in Fig. 3.1.

The experimental setup is a simple arrangement of an OFI based Doppler velocimeter, which components are explicitly described in the block diagram shown in Fig. 3.2.

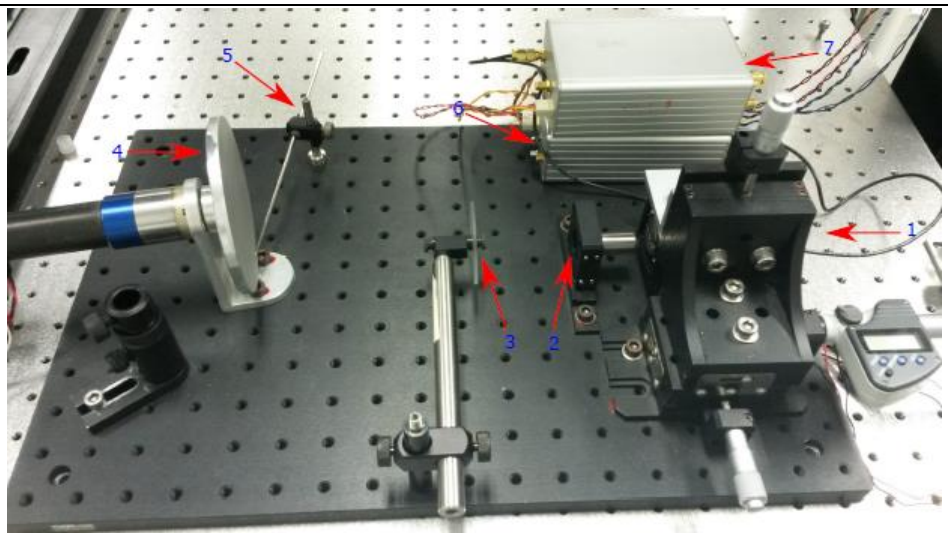

Fig. 3.1: Photography of the experimental setup for measuring velocity of a rotating disk: 1) a micrometric 3-axis mechanical stage, 2) lens, 3) neutral density, 4) rotating disk (target), 5) needle, 6) laser driver, and 7) amplifier.

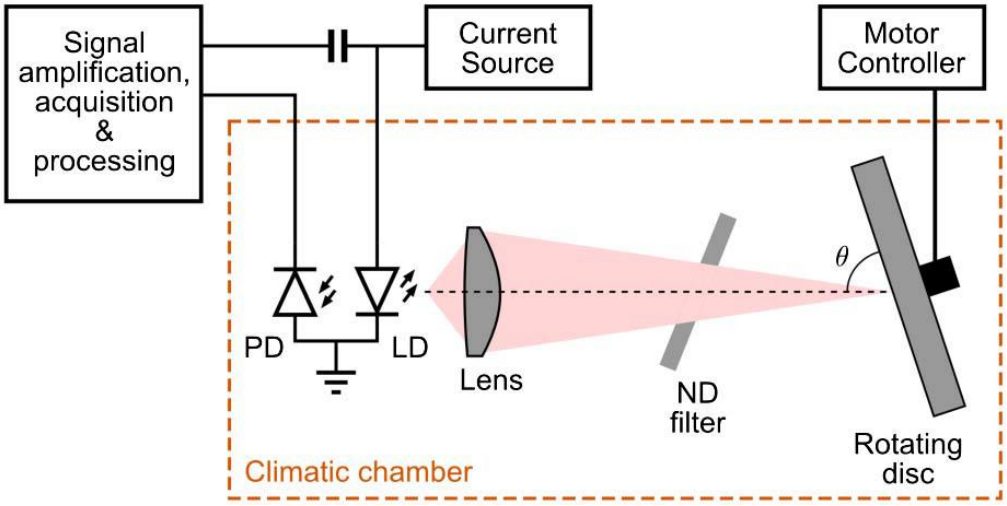

Fig. 3.2: Block diagram of the experimental setup inside the climatic chamber.

All tested lasers were mounted into a 5.6 mm TO can package type that includes a monitoring photodiode. The collimation lens used to focus the laser beam onto the target was a Thorlabs C240TME, with an 8 mm focal length, a numerical aperture NA of 0.5 with an ad hoc antireflective coating (1050–1620 nm or 600-1050 nm) depending on the emission wavelength of the laser under test.

The target was a sandblasted aluminium disk assembled with a step motor controlled by a custom made PID driver so as to ensure a stable and reliable rotation velocity. A drastic effort has been realized to ensure repeatability of the signal amplitude measurement: in this setup, the rotating target is in a fixed

position (constant distance with the laser and constant angle with the laser optical axis), same goes for the focusing lens which position cannot be modified. The only degree of freedom for the alignment and focus sharpness is the laser diode that was mounted on a micrometric 3-axis mechanical stage. To further ensure the repeatability of the performed experiments, a removable sharp-edge needle was attached to the setup so that the laser beam hit the disk at the same distance from its centre. Eventually, the focus sharpness is fixed by the optimization of the OFI signal amplitude while the signal FFT is observed in real-time with a dedicated Labview VI.

A neutral density filter was introduced into the optical path (with a fixed position and angle with the propagation axis) between the lens and the target thus allowing a minimal control on the amount of optical feedback.

The complete opto-mechanical system was assembled on a portable board so that it could be placed in a climatic chamber (model: EXCAL 2221-TA), which provides temperature control over the range of −40 °C - 80 °C.

The laser was driven by a current source (a custom built laser driver) that is controlled by an external voltage source.

A National Instruments data acquisition card (model: NI-6251) ensures both the control of the laser driver and the acquisition of PDs and LV signals that are at a sampling rate of 1 MS⁄s. The acquired signals are first amplified using custom built transimpedance and voltage amplifiers respectively. The trans-impedance amplifier has a plateau gain of 126 $dB_{V/A}$, the voltage amplifier for the LV signal has a plateau gain of 114 dB, while all amplifiers have an amplification bandwidth from 0.5 kHz to 780 kHz.

A Labview VI drives all functions of the NI-6251 acquisition card and in the mean time performs the initial signal processing that consists of a series of 20 consecutive Fast Fourier transforms that were then averaged thus providing a spectral analysis of the OFI signals.

In a second time, a post processing of the frequency domain signals is performed to determine the amplitude of the OFI signal and the noise level at the central Doppler frequency using the Matlab's *fminsearch* derivative-free fitting method

on a Gaussian function as first proposed by Kliese et al. [154] to ensure accurate and reliable determination of the SNR.

3.1.2 Detailed description and characterization of both laser diodes

For the sake of simplicity, we have considered in the model presented in chapter 2 an ideal laser diode which would be similar to a Fabry-Pérot structure but with a pure single-mode emission.. However, it is far more complex when dealing with practical laser diodes since Fabry-Pérot laser diodes are emitting several longitudinal modes while pure single-mode devices have more complex structures including various implementations of Bragg reflector in the cavity. This means that it is quite difficult to develop a single model that perfectly describes the behaviour of all different laser diodes when subjected to optical feedback. As mentioned before, for the validation of our model, we performed a set of experiments on two different types of laser diodes: a DFB and a VCSEL thus considering that the impact of multimode emission on the laser behaviour is more important than the cavity structure effects.

The DFB laser (ML725B11F, λ = 1310 nm) is a single-mode Mitsubishi InGaAsP laser diode from the ML7XX11 series operating around 1310 nm. A photodiode, for optical output monitoring, is already implemented inside a 5.6 mm TO-can package with a flat window cap. The laser's anode is connected to the photodiode's cathode making it a common-anode device.

The other laser is a single-transverse and a single-longitudinal Lasermate VCSEL from the VCT-F85A32-IS-V2 model, operating around 850 nm, with a build-in monitor photodiode inside a 4.6 mm TO-can package, with a tilt window. The device is three-pin common-anode as the laser's anode is connected to the photodiode's cathode.

The absolute maximum ratings of both laser diodes, as described in their datasheets, are introduced in Table 3.1.

Parameter	DFB	VCSEL	Unit
Output power	100.0	2.0	mW

Forward current	150.0		8.0		mA
Operating temperature	Min.	Max.	Min.	Max.	˚C
	- 40.0	+ 85.0	0.0	+ 70.0	

Table 3.1: A comparison of the absolute maximum ratings of the lasers.

Other typical parameters of the both laser diodes are introduced in Table 3.2.

Parameter	DFB			VCSEL			Unit
Threshold current	Case Temp.	Typ.	Max.	Typ.	Max.		mA
	25℃	6.0	12.0	1.8	3.0		
	85℃	30.0	40.0				
Operating current	Case Temp.	Typ.	Max.	Power	Typ.	Max.	mA
	25℃	16.0	30.0	1 mW	3.0		
	85℃	50.0	75.0	2 mW	5.0		
Peak wavelength	Min.	Typ.	Max.	Min.	Typ.	Max.	nm
	1290	1310	1330	840	850	860	
Slope efficiency	Min.	Typ.	Max.	Min.	Typ.	Max.	W/A
	0.3	0.5		0.5	0.6	0.8	
Operating voltage	Min.	Typ.	Max.	Min.	Typ.	Max.	V
		1.1	1.5	1.9	2.2	2.4	
Beam divergence		Typ.	Max.	Min.	Typ.	Max.	Degree
	Parallel	25.0	35.0	6.0	7.0	10.0	
	Perpendicular	30.0	40.0				

Table 3.2: A comparison of the important parameters of the lasers.

As can be expected, the VCSEL has a greater slope efficiency and a smaller divergence angle than those of the DFB. The operating current of the VCSEL is much smaller but this laser propose a much smaller bias current range than the DFB, which is also supposed to operate over a larger range of temperatures. The slope efficiencies, as given by the manufacturer are similar, while due to the difference in the semiconductor alloy and laser structure, the VCSEL operating voltage is expected to be twice of that of the DFB.

Those are the generic parameters of both the DFB and the VCSEL as provided by the manufacturers. However, the work developed in the previous chapter has shown the major role played by the threshold current and the slope efficiency of the laser in the evolution of the OFI signals amplitudes. These parameters have to be characterized with greater attention. The experimentally obtained characteristic L-I curves of both lasers as well as the deduced actual values of the corresponding parameters are presented below:

a) ML725B11F DFB laser

We have measured the light-current curves of the DFB over the entire range of laser injection current, described in tables 3.1 and 3.2, at different operating temperatures. Fig. 3.3 shows the output optical power of the DFB measured for temperatures ranging from −40 °C to 80 °C in steps of 5 °C. Power measurements were realized using the monitoring photodiode coupled with a dedicated low-noise trans-impedance amplifier (60 $dB_{V/A}$). The relationship between the voltage output of the amplifier and the emitted power of the laser had been formerly calibrated.

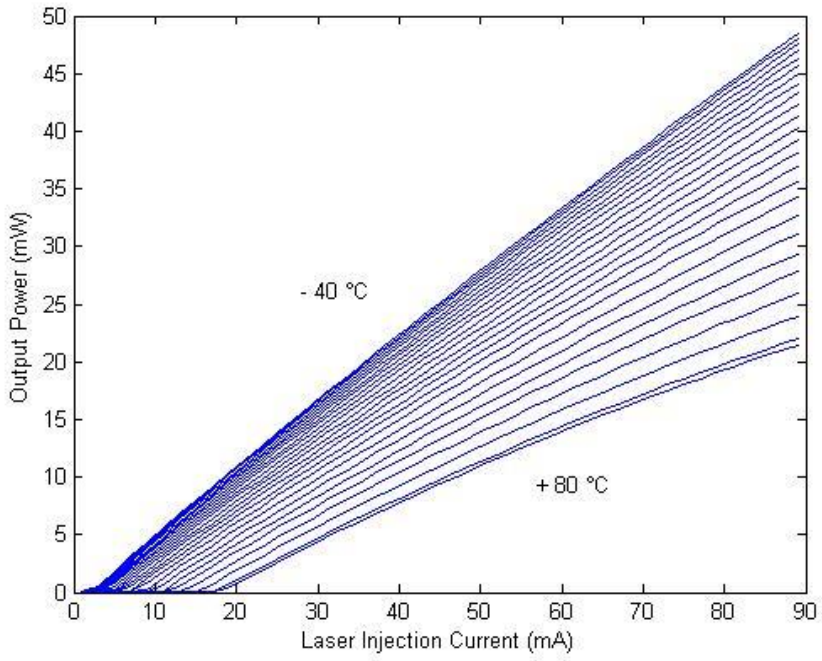

Fig. 3.3: Output optical power of the DFB laser as a function of laser injection current measured at different operating temperatures (ranging from -40˚C to 80˚C in steps of 5˚C).

We observe a decrement in the output power at a given bias current as the operating temperature increases. This decrement is accompanied by an increment in the threshold current. Furthermore, the slope efficiency is almost constant with injection current at low temperatures, while it shows a more sensible gradual decrement at high temperatures.

Solid lines in Fig. 3.4 show the extrapolated evolutions of the threshold current derived using the second derivative method (solid blue) and of the maximum slope efficiency obtained from the first derivative of the L-I curve; solid green) [155]. Over this wide range of temperatures, an increase of the threshold current from 2.3 to 18.3 mA is observed together with a decrease from 0.66 to 0.38 W/A of the maximum slope efficiency.

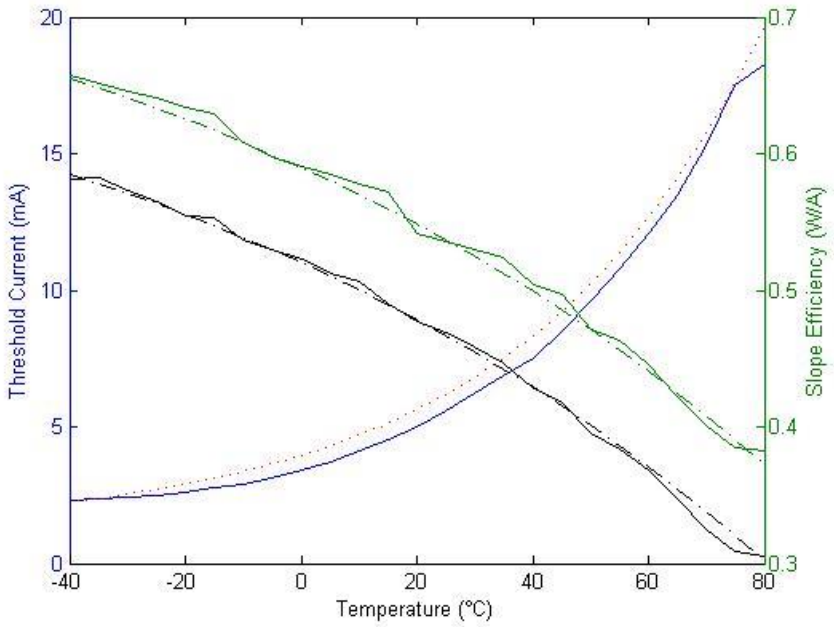

Fig. 3.4: Measured (solid lines) and fitted (dashed and dotted lines) slope efficiency and threshold current of the DFB laser diode as a function of the operating temperature. The upper slope efficiency curve is the maximum while the lower one is the average.

To account for the effects of temperature on the laser threshold current and slope efficiency in our rate equation model - namely that an increase of the temperature induces an increase of the threshold current and a decrease of the slope efficiency, we model both parameters evolution by exponential functions [147]:

$$I_{\text{th}}(T + \Delta T) = I_{\text{th}}(T).e^{\frac{\Delta T}{T_0}} \tag{3.1}$$

$$\eta(T + \Delta T) = \eta(T).e^{\frac{-\Delta T}{T_\eta}} \tag{3.2}$$

where T_0 and $T\eta$ are the characteristic temperatures of the laser diode, which determine the sensitivity of the laser diode to temperature changes.

Dashed and broken lines superimposed on Fig. 3.4 are the fitted curves of the forms (3.3) and (3.4), resulting in characteristic temperatures T_0 = 42 °C and $T\eta$ = 120 °C, which show good agreement with experimental data.

b) VCT-F85A32-IS-V2 Lasermate VCSEL

Similarly, the light-current curves measured of the VCSEL over the entire range of injection currents and for temperatures ranging from 0 °C to 70 °C in steps of 5 °C are shown in Fig. 3.5. The measurements were performed in similar conditions of those used for the DFB (monitoring photodiode with a dedicated low-noise trans-impedance amplifier (60 $dB_{V/A}$)).

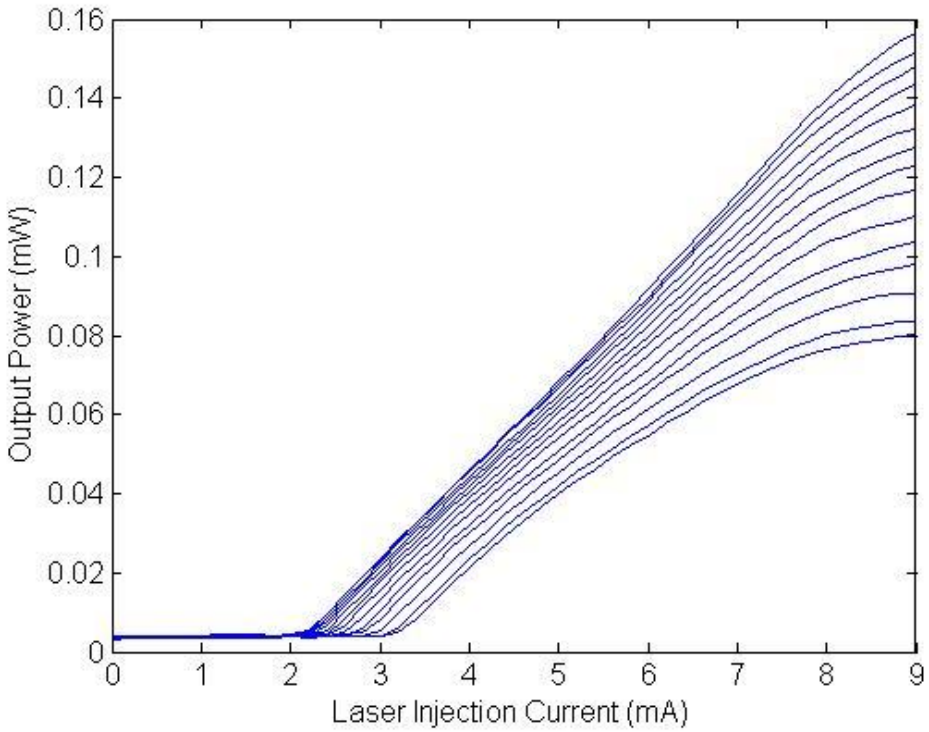

Fig. 3.5: Output optical power of the VCSEL as a function of laser injection current measured at different operating temperatures (ranging from 0˚C to 80˚C in steps of 5˚C).

As expected, we observe a decrement in the output optical power as the operating temperature increases accompanied by an increment of the threshold current. The decrement of the slope efficiency with the laser injection current and the temperature is much more important than for the DFB laser especially at high temperatures.

Fig. 3.6 shows the evolution of both the threshold current (solid blue) and the slope efficiency (solid green) with temperature. As predicted by eq. (3.1) and eq. (3.2), the threshold current increases from 2.2 to 3.4 mA while the slope efficiency decreases from 0.61 to 0.33 W/A due to thermal effects. Fitted curves show geed agreement with experiment for the characteristic temperatures T_0 = 39 °C and $T\eta$ = 130 °C.

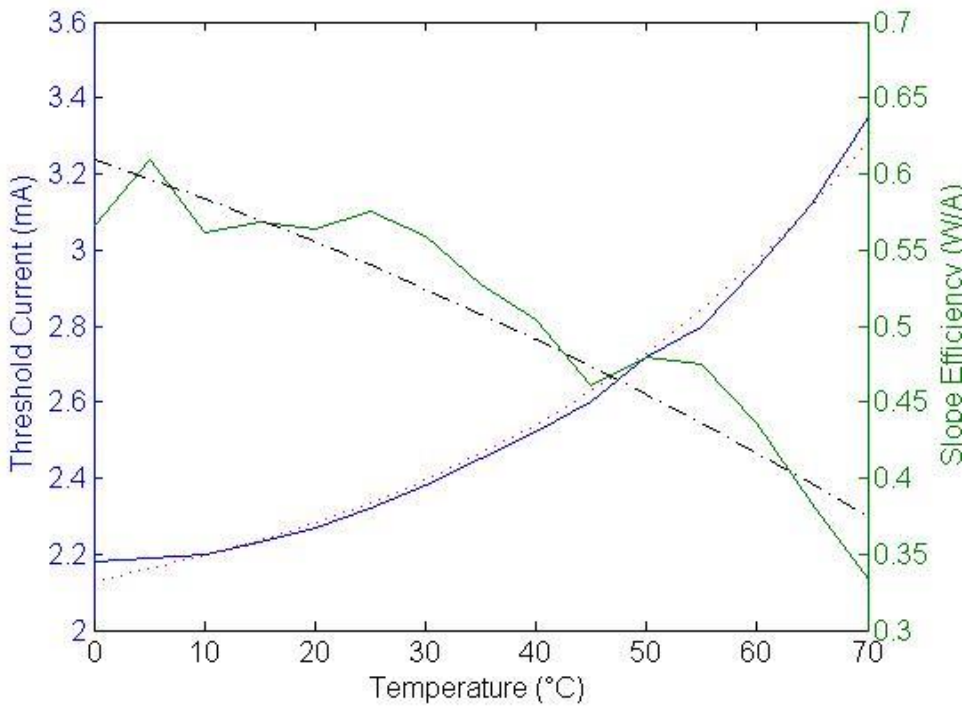

Fig. 3.6: Slope efficiency and threshold current of the VCSEL as a function of the operating temperature.

3.2 Experimental Validation

The experimental setup, thoroughly explained in the previous section, has been used to perform the experimental measurements of the OFI Doppler signal amplitude on both laser diodes in order to validate the analytical model. We firstly introduce the DFB results, and then we introduce the results of the more complex-structured VCSEL in comparison.

3.2.1 A DFB laser diode subject to optical feedback

a) Methodology

As mentioned before, the OFI signal is analyzed in the frequency domain after an FFT has been performed then the spectrum has been truncated around the Doppler average frequency so as to facilitate the fitting of the Doppler peak by a Gaussian based function expressed as:

$$G(f) = A\, e^{\frac{(f-f_D)^2}{B}} + C.f + D \tag{3.3}$$

where A is what could be defined a Carrier to Noise Ratio (CNR) i.e. the ratio of the signal amplitude at the Doppler frequency to the noise floor at the same frequency, f_D is the Doppler frequency, B is related to the full width at half maximum (FWHM), the parameter D represents the noise floor, and $C.f$ is a linear function that takes into account the noise curve decay or increment observed at the vicinity of the Doppler peak. Fig. 3.7 shows the result of the fitting process for a given acquisition. The noise should be flat, yet the noise is higher around 100 kHz due to the noise of the electronics.

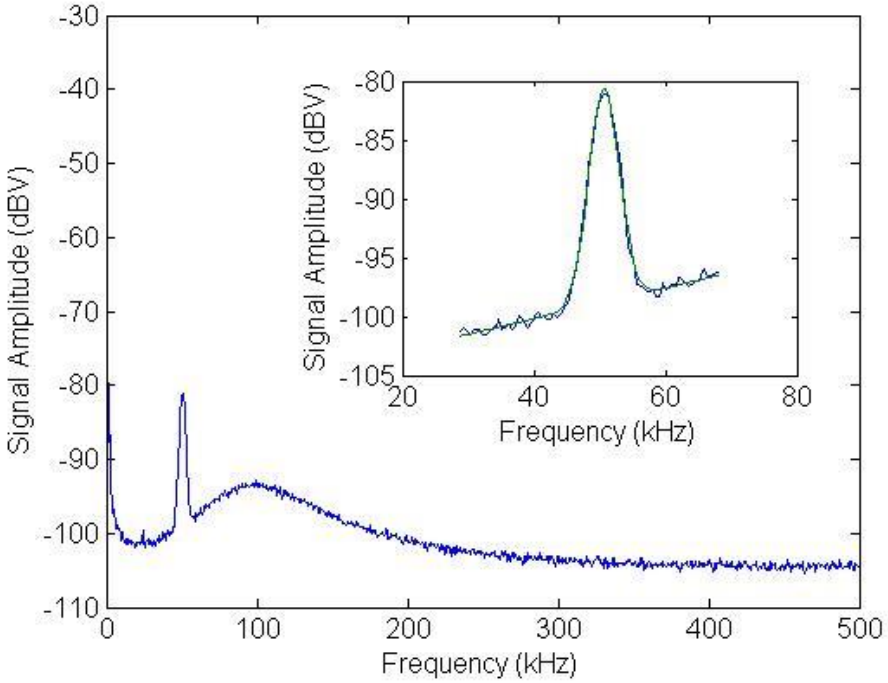

Fig. 3.7: The Doppler signal spectrum. The inset shows the fitting of the measured spectrum (black) to a combination of a Gaussian function and a linear function fitting the noise floor (green).

b) Impact of the injection current

The measurement of the OFI signal amplitude acquired through the monitoring PD, over the laser injection current, and for T=25°C, is presented in Fig. 3.8 (red solid line). The evolution of the signal amplitude as predicted by the model given in eq. (2.86) is presented on the same figure. To highlight the impact of the slope efficiency on the amplitude evolution, both the results predicted by the model with constant slope efficiency (green broken line) and with the actual slope efficiency (blue solid line) are compared to the measurement. It is to be noted that all the intrinsic laser parameters required for the simulation were taken from [147] and that the only fitting action consists in a scaling factor included to shift vertically the simulated curves in logarithmic scale. By taking into account the actual slope efficiency, the model shows good agreement with measurement over a wide range of injection current levels.

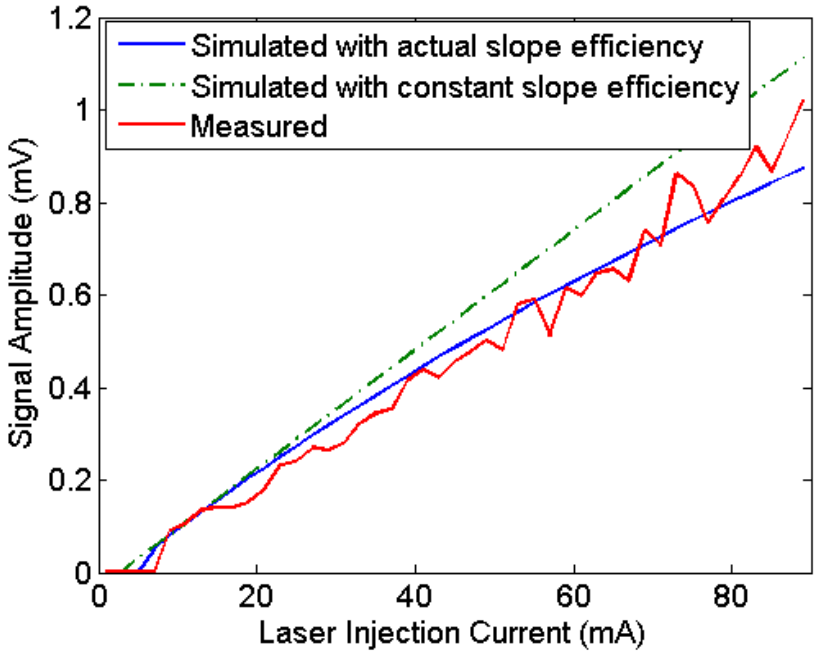

Fig. 3.8: Evolution of the PD signal amplitude of the DFB with laser injection current: measured (red solid); modelled (constant slope efficiency of an ideal laser diode, green dashed); modelled (actual slope efficiency, blue solid).

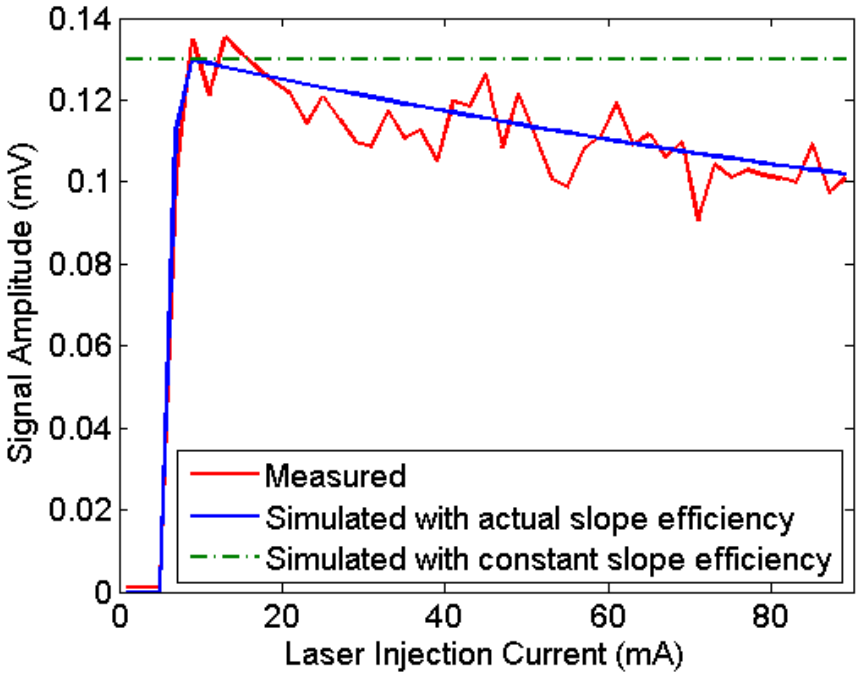

Fig. 3.9: Evolution of the LV signal amplitude of the DFB with laser injection current: measured (red solid); modelled (constant slope efficiency of an ideal laser diode, green dashed); modelled (actual slope efficiency, blue solid).

Figure 3.9 shows similar measurement and simulation results for the LV signal at T = 25 °C (red solid line) and two model curves: (i) constant slope efficiency (green broken line), and (ii) actual slope efficiency (blue solid line). The major result of Fig. 3.9 is that the amplitude of the LV signal has a peak slightly above threshold, and then it monotonically decreases with the increment of injection current. Thus, comparing the simulation with constant and actual slope efficiencies, this decay in amplitude with the laser injection current is perfectly explained by the corresponding decay in slope efficiency.

c) Impact of the temperature

The effect of temperature on the PD and LV signal strengths at a laser injection current of 59 mA (up to 25 times the threshold current) is shown in Fig. 3.10 and Fig. 3.11, respectively. In Fig. 3.10, the amplitude of the PD signal shows a monotonic decrement with the increment of the operating temperature. At low operating temperatures, the slope efficiency decreases less with the increment of injection current, thus the decrement of the PD signal amplitude is not steep. However, as the operating temperature increases, the slope efficiency decreases severely while the injection current increases, resulting in the steep decrement observed in Fig. 3.10. This result is coherent with the model's prediction in eq. (2.86), and the decay in amplitude is exclusively linked to the decay of the slope efficiency with temperature.

However the LV signal, shown in Fig. 3.11, shows a different behaviour. As demonstrated in the previous chapter, there are two actions of the temperature on the strength of the LV signal: the LV signal amplitude as expressed in eq. (2.103) is directly proportional to the temperature, but in the mean time, the slope efficiency that decreases with temperature leads to the decrement of the signal amplitude.

As mentioned above, the slope efficiency of the DFB is almost constant over the entire range of injection current at low temperature. Thus, the dominant parameter controlling the strength of the LV signal is the operating temperature, which induces an increment of the signal amplitude. However, for higher temperatures, the diminution of the slope efficiency becomes more important thus leading to it being the dominant parameter. Hence, in Fig. 3.11 we observe a different

evolution for the LV signal amplitude that presents a maximum at usual room temperatures and decreases at lower or higher temperatures.

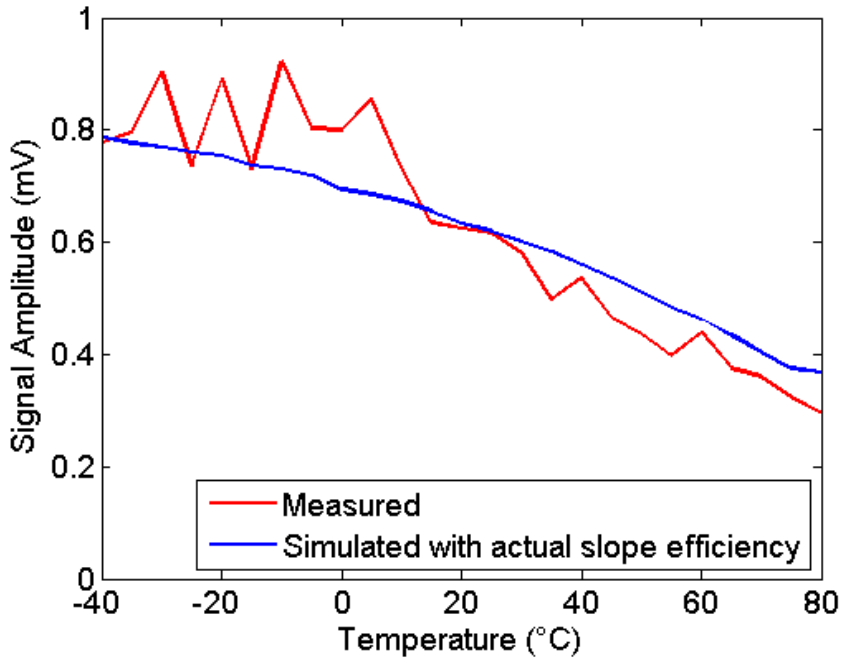

Fig. 3.10: Evolution of the PD signal amplitude of the DFB with the operating temperature: measured (red solid); modelled (actual slope efficiency, blue solid).

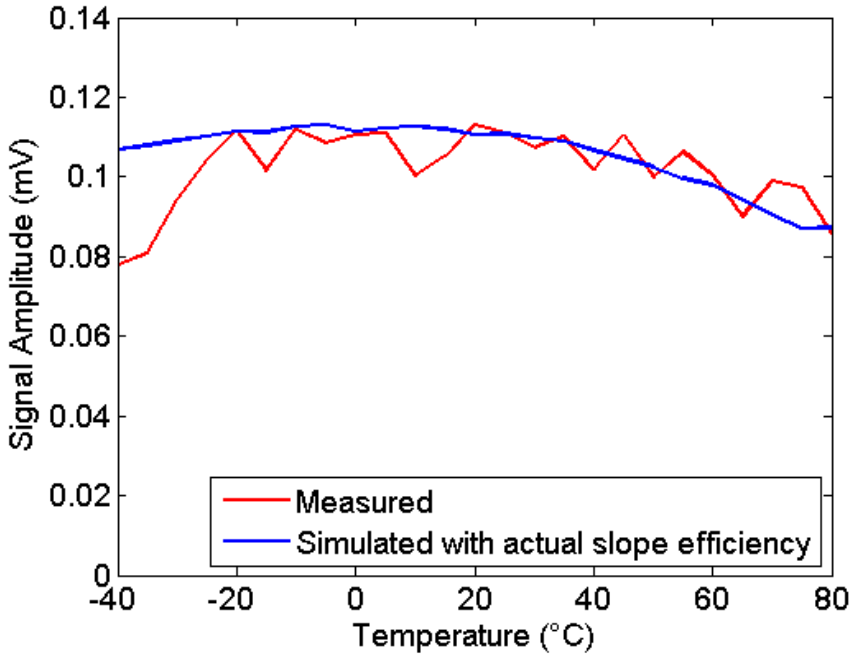

Fig. 3.11: Evolution of the LV signal amplitude of the DFB with the operating temperature: measured (red solid); modelled (actual slope efficiency, blue solid).

In both Figures, the model using actual slope efficiency (blue solid line) agrees well with the experimentally observed evolution of the signal strength with temperature (red solid line), thus highlighting the importance of the temperature-dependent behaviour of the slope efficiency. These results show that an increase in either laser injection current or temperature results in a decrease in slope efficiency which in return affects the OFI signals amplitudes. Therefore, it is important to capture the simultaneous impact of laser injection current and temperature on OFI signal strength.

Figures 3.12 and 3.13 show the measured and modelled PD and LV signals, respectively, as a function of both the laser injection current and temperature. The PD signal, modelled with the actual slope efficiency [Fig. 3.12(b)], shows good agreement with the measured signal [Fig. 3.12(a)] over the entire range of injection currents and temperatures. The influence of the slope efficiency on the PD signal strength can be directly observed through the decrease of the signal strength at high temperatures. The exponential increment of the threshold current with temperature can also be observed.

Similarly, the LV signal, simulated with the actual slope efficiency [Fig. 3.13(b)], shows good agreement with the measured signal [Fig. 3.13(a)]. The LV signal is a maximum for mid-range temperatures: the low-temperature range is dominated by the direct relationship between voltage and temperature while, at higher temperatures, the decrease in slope efficiency becomes the dominant factor, and the net result is a sharp decrease in signal strength. Again, the exponential increment of the threshold current with the operating temperature is observed. The unexpected sever decay of the LV signal amplitude at the lowest temperature may be due to difference between the laser junction and the operating temperatures.

Here, the model has been validated experimentally for the DFB laser diode. Both the PD and the LV signals show good agreement with the model. Unlike the PD signal, the LV signal is not linearly increasing with the injection current, but it decreases with the increment of injection current. The effect of the slope efficiency on the PD signal is observed at high injection current as it becomes greater. To conclude, the influence of the slope efficiency on the amplitudes of the PD and the LV signals has been demonstrated theoretically and experimentally.

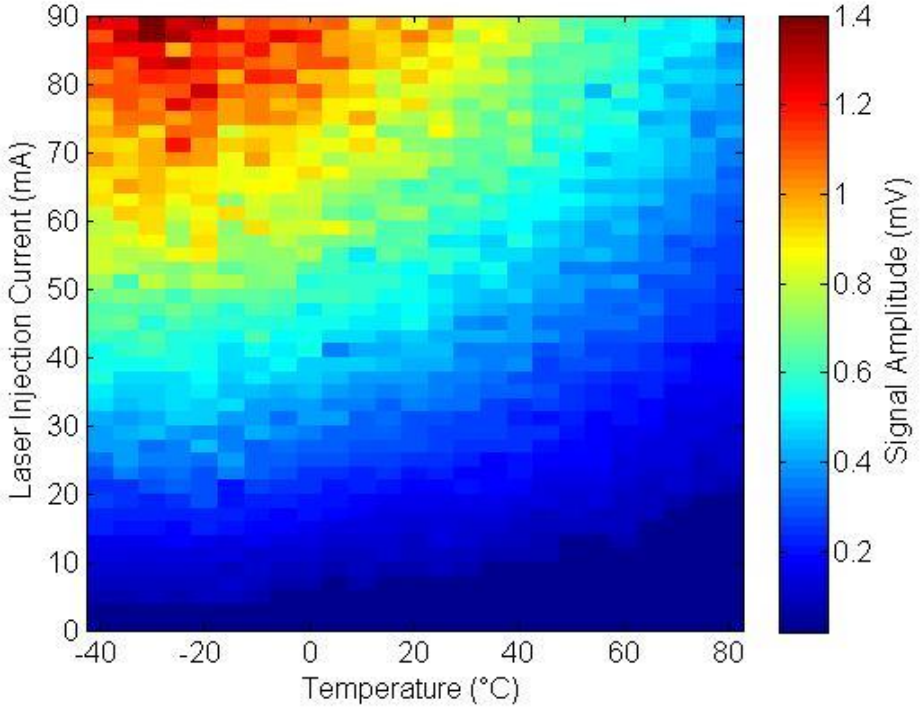

(a)

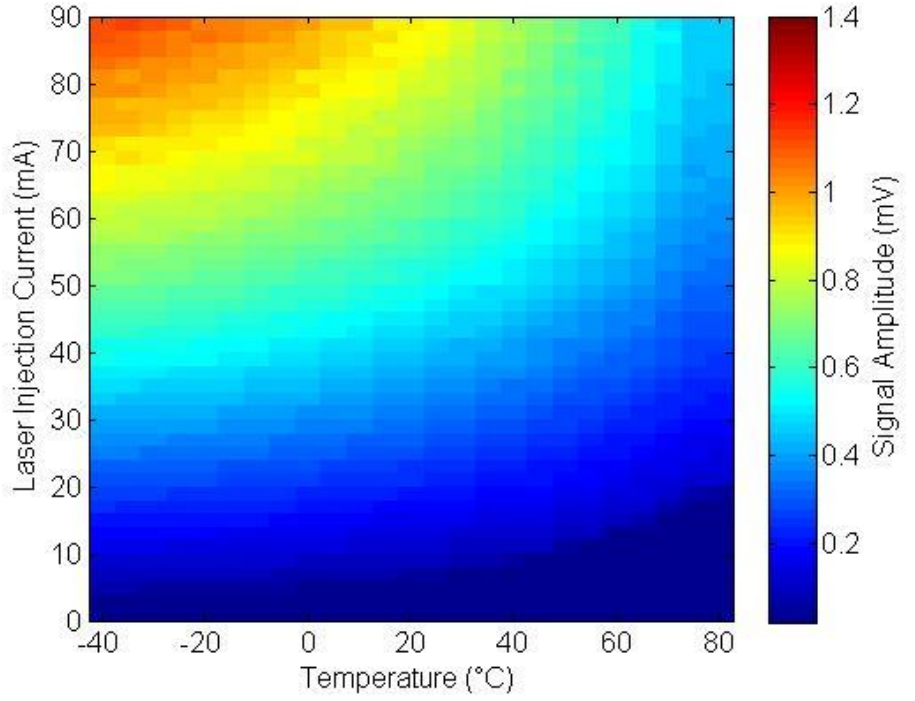

(b)

Fig. 3.12: PD signal strength of the DFB laser diode as a function of the laser injection current and the operating temperature: (a) measured and (b) modelled.

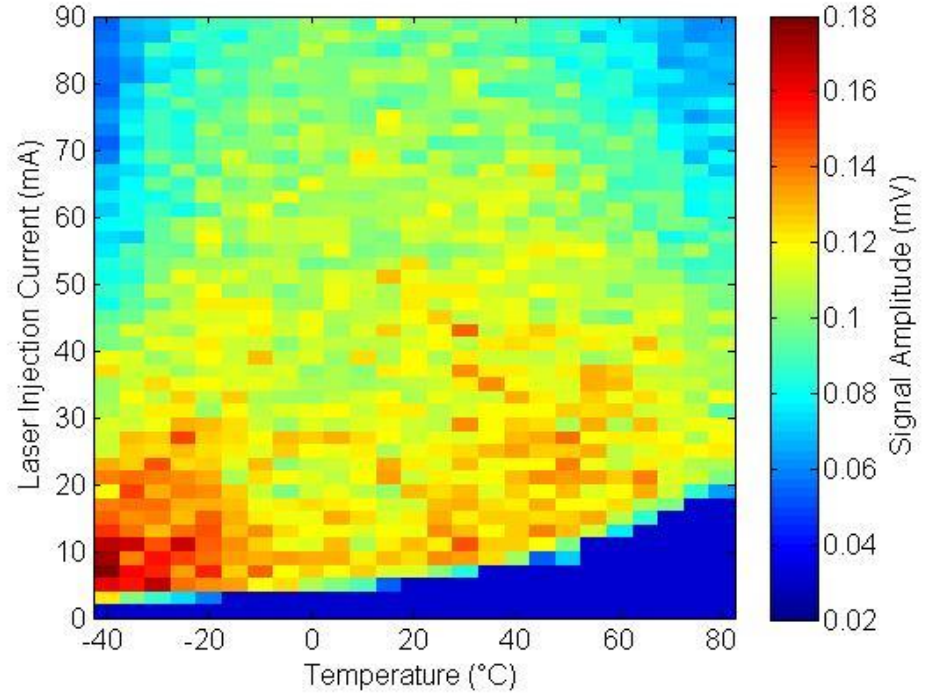

(a)

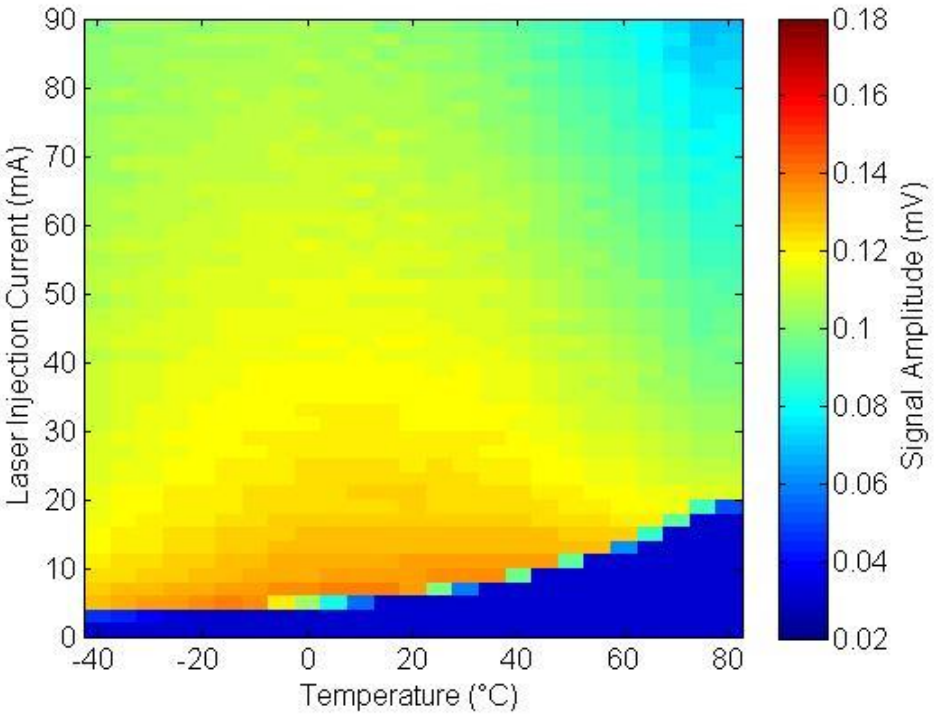

(b)

Fig. 3.13: LV signal strength of the DFB laser diode as a function of the laser injection current and the operating temperature: (a) measured and (b) modelled.

3.2.2 A VCSEL subject to optical feedback

The same experiments were performed using the VCSEL over the temperature range of 0 °C - 70 °C. Figure 3.14 shows the measured OFI PD signal at T = 20 °C (red solid line) and two curves modelled by considering: (i) the constant slope efficiency (green broken line), and (ii) the actual slope efficiency (blue solid line). The model shows good agreement with measurement over a wide range of injection current levels when the actual slope efficiency is considered.

One unexpected result shown in Fig 3.14 and 3.15 is that there is a difference between the threshold for the lasing condition and the threshold for the OFI which is sensibly higher. To our knowledge, such behaviour has not been reported in literature.

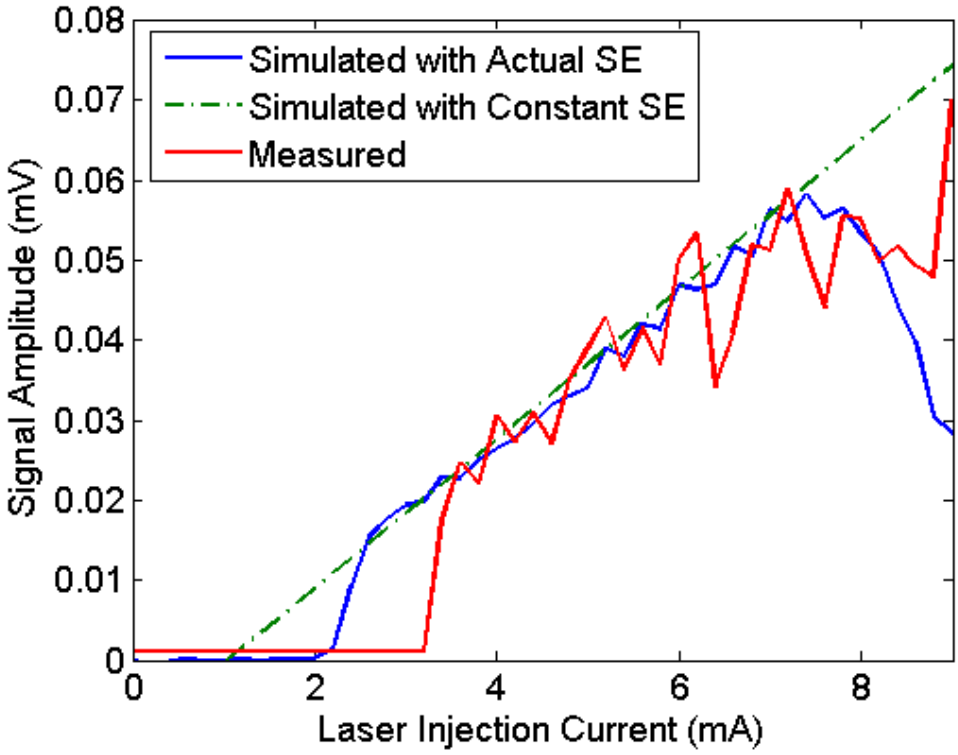

Fig. 3.14: Evolution of the PD signal amplitude of the VCSEL with laser injection current at 20℃: measured (red solid); modelled (constant slope efficiency of an ideal laser diode, green dashed); modelled (actual slope efficiency, blue solid).

The LV signal measured at T = 20 °C (red solid line) and two curves modelled by taking in account: (i) a constant slope efficiency (green broken line), and (ii) the actual slope efficiency (blue solid line) are shown in Fig. 3.15. The LV signal has a peak just slightly above threshold, and then it decreases with the increment of injection current. The variations observed at mid-range injection currents are related to the rough fitting due to the low averaging. Again, the difference in the threshold values is observed.

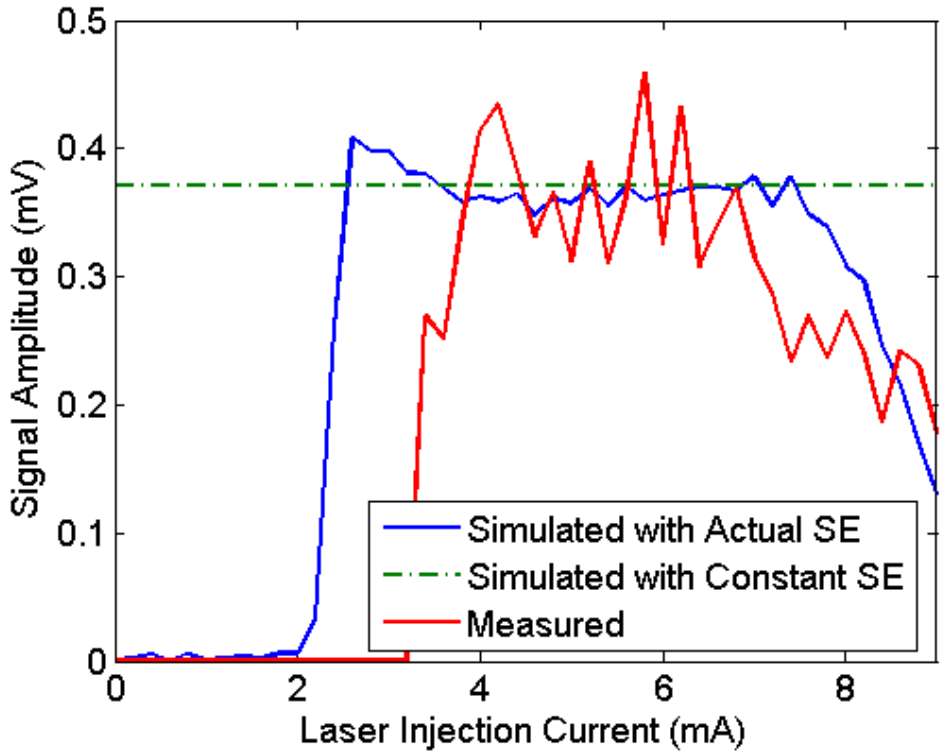

Fig. 3.15: Evolution of the LV signal amplitude of the VCSEL with laser injection current: measured (red solid); modelled (constant slope efficiency of an ideal laser diode, green dashed); modelled (actual slope efficiency, blue solid).

Alternatively, the injection current was fixed at 6 mA over the entire range of the operating temperature. The temperature effect on the PD and LV signal amplitudes are shown in Figs. 3.16 and 3.17, respectively. From Fig. 3.16, the model using actual slope efficiency (blue solid line) agrees well with the experimentally observed decrease in signal strength (red solid line), highlighting the importance of the temperature-dependent slope efficiency. As predicted by the analytical model, the decrement of the signal amplitude is monotonic with temperature.

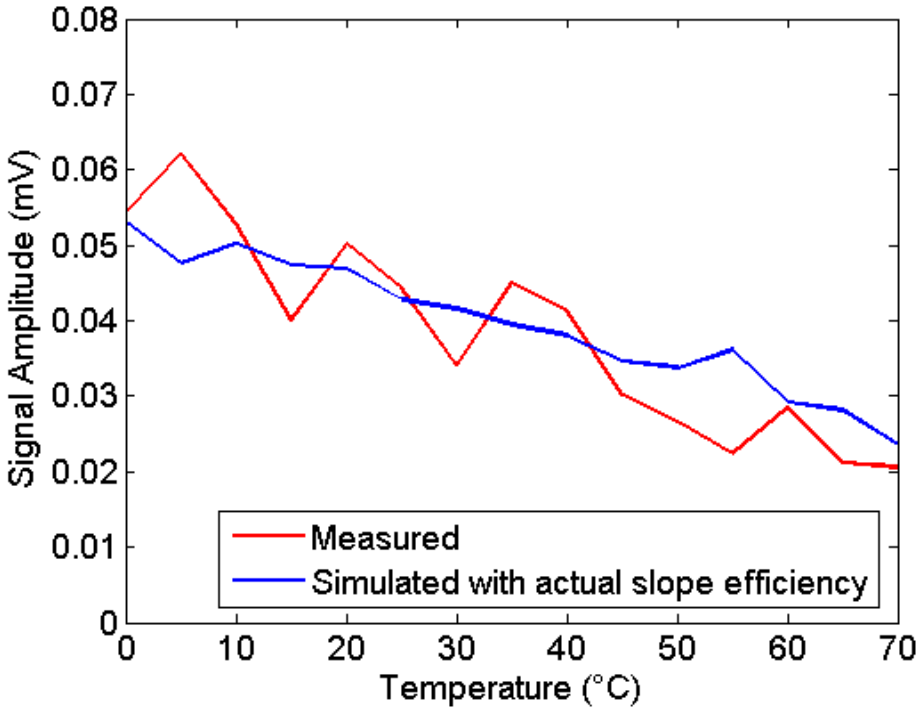

Fig. 3.16: Evolution of the PD signal amplitude of the VCSEL with the operating temperature: measured (red solid); modelled (actual slope efficiency, blue solid).

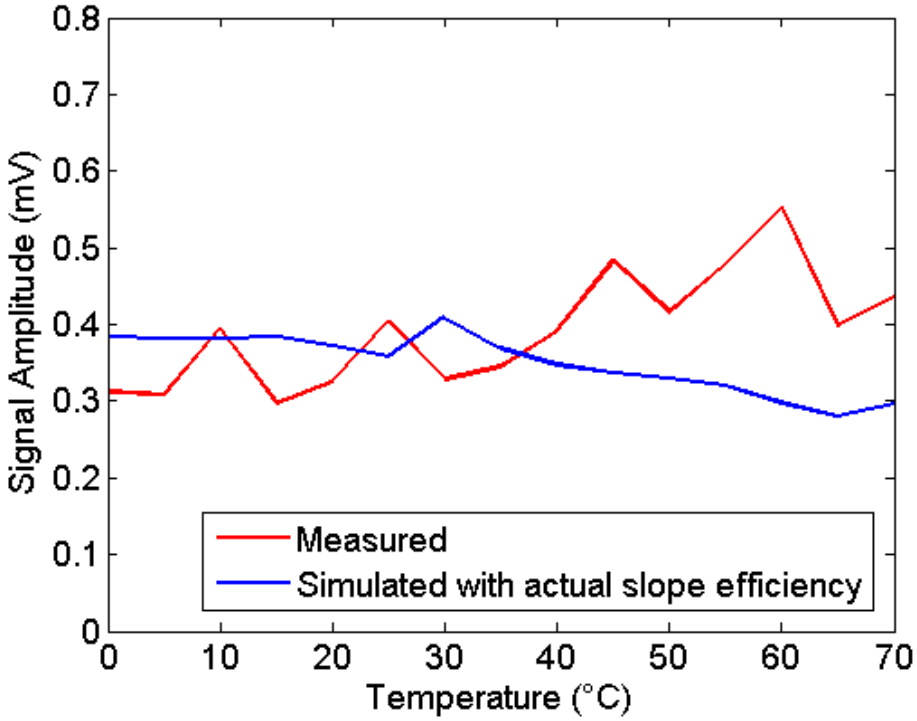

Fig. 3.17: Evolution of the LV signal amplitude of the VCSEL with the operating temperature: measured (red solid); modelled (actual slope efficiency, blue solid).

However, as shown in Fig. 3.17, contrary to what is predicted by the model, the LV signal amplitude increases with the increment of temperature. This could be due to the interaction between injected carriers and the distributed Brag reflector (DBR) mirrors resulting in a higher series resistance. As mentioned before, effect of complex laser structures on the OFI signal amplitude was not considered in the model analysis.

Fig. 3.18 and Fig. 3.19 show the measured and modelled OFI signals as a function of both injection current and temperature. As shown in Fig. 3.18(b), the PD signal modelled with the actual slope efficiency shows good agreement with the measured signal [Fig. 3.18(a)] over a wide range of injection current ad temperature. Other than the difference in threshold currents and the divergence at high injection currents from the measured values, the modelled signals show good agreement with measurements over a wide range of injection current levels when the actual slope efficiency is considered. The difference in slope efficiency may be due to the strong attenuation. Moreover, the predicted decrement in the modelled PD signals is a result of the steep decrement in the slope efficiency, which may be due to an appearance of a second mode.

Similarly, the LV signal, simulated with the actual slope efficiency [Fig. 3.19(b)], shows good agreement with the measured signal [Fig. 3.19(a)] for a wide range of injection currents. However, a strong divergence between modelled and measured signals is observed at high temperatures as the model predicts the decrease of the signals amplitudes while - in practice - they increase with temperature. As explained earlier, this may be related to the more- complex VCSEL structure effect on the OFI signals amplitudes.

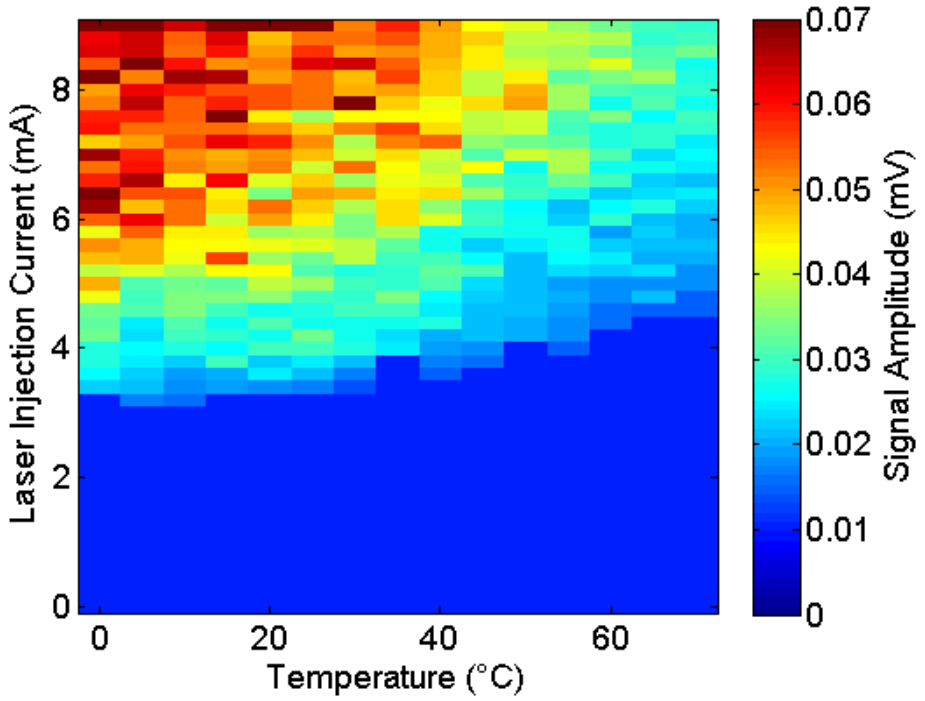

(a)

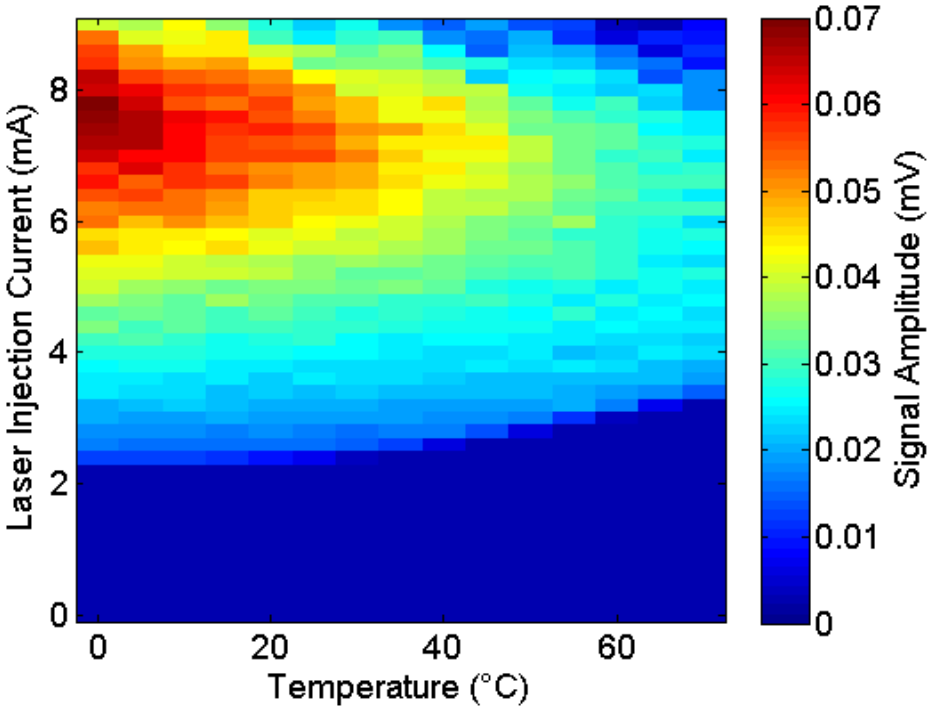

(b)

Fig. 3.18: PD signal strength of the VCSEL as a function of the injection current and the operating temperature: (a) measured and (b) modelled.

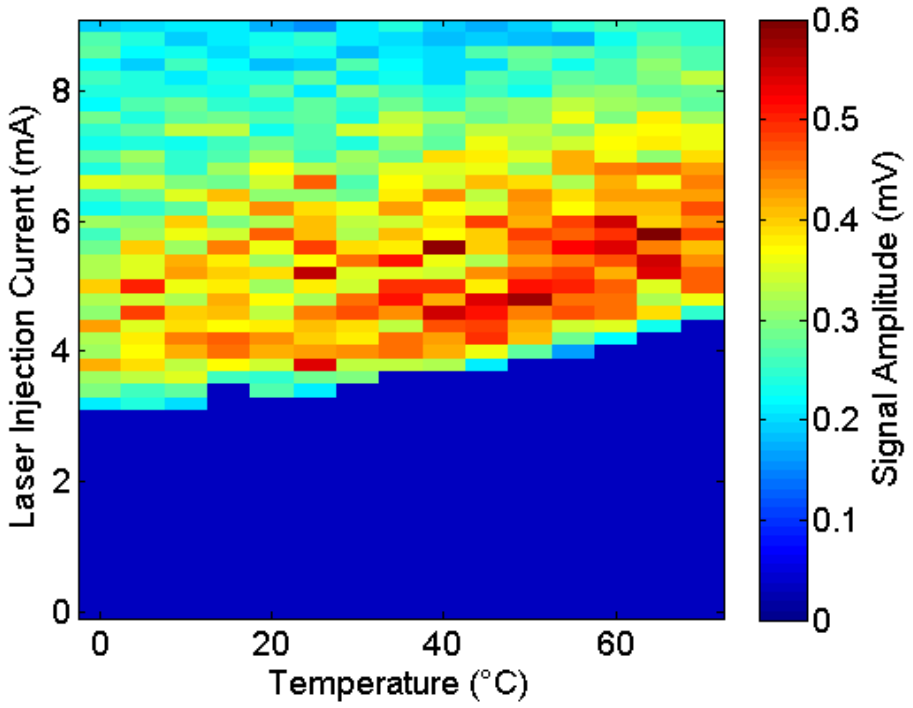

(a)

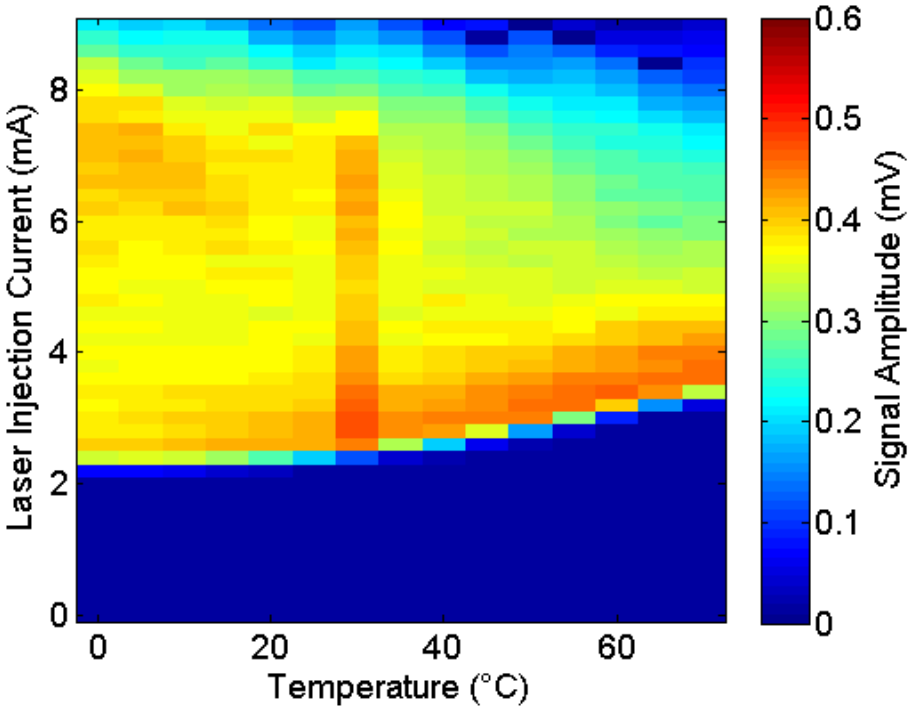

(b)

Fig. 3.19: LV signal strength of the VCSEL as a function of the injection current and the operating temperature: (a) measured and (b) modelled.

In brief, the model has been validated experimentally for the VCSEL as well. Both the PD and the LV signals show good agreement with the model over a wide range of injection currents and temperatures. However, the model doesn't consider the exact structure of the each laser diode, which results in predicting the decrease of the LV signals amplitudes with temperature while they increase in practice. Also, the model predicts a sharp decrease in the amplitude of the PD signal at high injection currents which could be explained by the appearance of a second mode.

3.3 OFI signals strengths evolution for multimode lasers

In the previous section, we proposed the experimental validation of our analytical model for both DFB and VCSEL lasers. In this section, we compare the OFI signals obtained from the single-mode laser diodes, in the previous section, and those obtained from multimode laser diodes. This measurement are performed in order to determine to what extent our model, which is developed based on the rate equations of single-mode laser diodes, can be applied to multimode laser diodes as well.

a) Two-mode VCSELs

At first we have performed the measurements with an Optowell VCSEL (model PS67-F1P1U-KC). This VCSEL is interesting in that it exhibits both single-mode and multimode operations. At low injection currents, it operates as a single-mode device, while at high injection currents; a second mode appears as shown in Fig. 3.20(a), where the mode hopping is observed, and in Fig. 3.20(b) where the detected power of each mode is displayed.

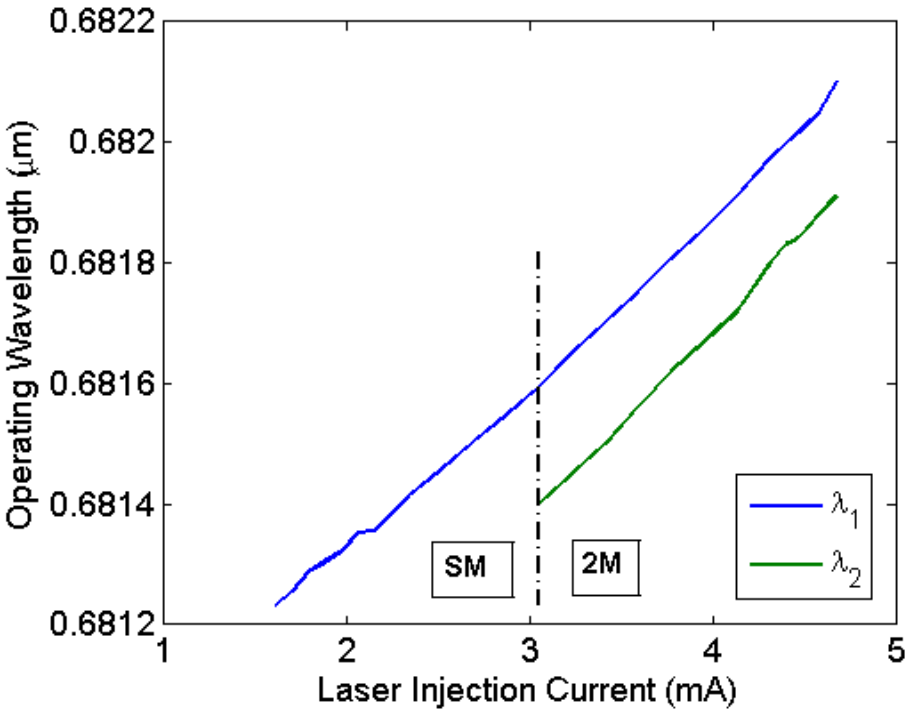

(a)

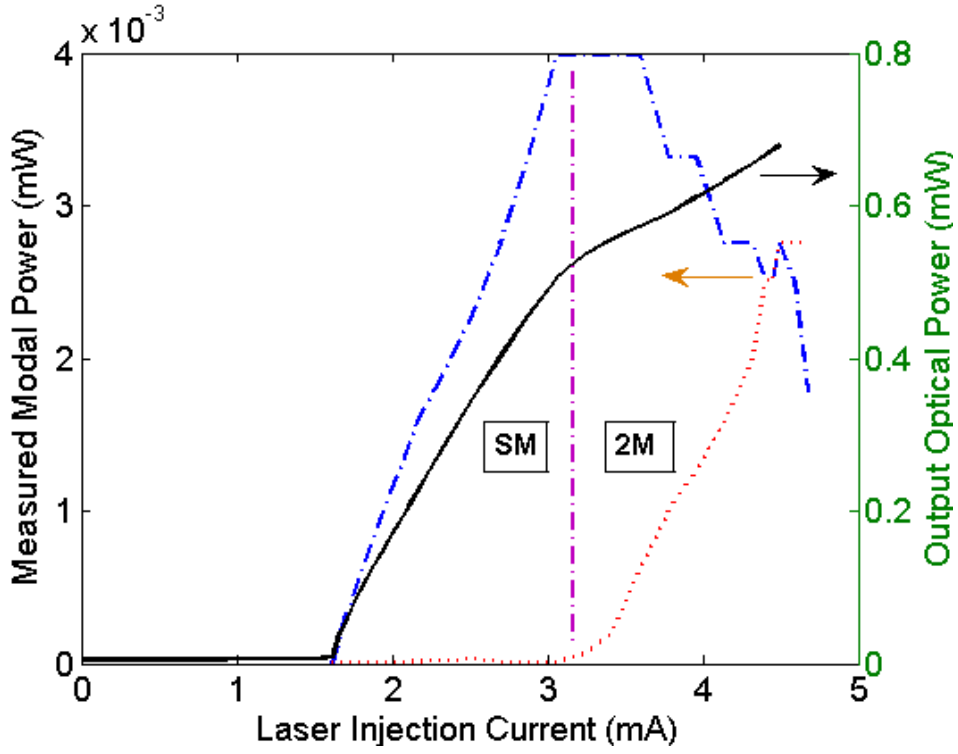

(b)

Fig. 3.20: The two-mode operation of the VCSEL a) the operating wavelength and b) the total output power and detected power of each mode.

Figure 3.21 shows the evolution of the PD signal amplitude with injection current for this VCSEL. PD signals are linearly increasing with injection current as long as the laser diode is operating on single-mode. Whenever a second mode appears, a decrease in the signal amplitude is observed followed by a non-linear growth of the signal.

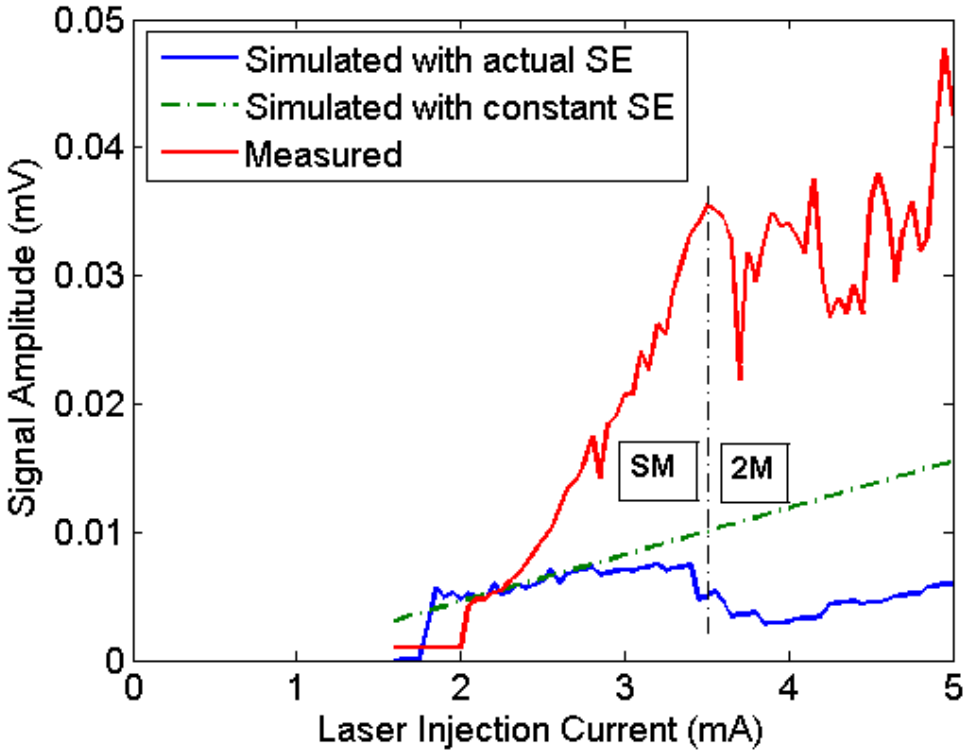

Fig. 3.21: Evolution of the PD OFI signal amplitude with the laser injection current in the two-mode VCSEL. Solid blue line: simulated taking into account the actual slope efficiency; dashed line: simulated with constant slope efficiency; red solid line: measured.

Figure 3.22 shows the evolution of the voltage signals amplitudes with injection current for the two-mode VCSELs. For low injection currents, the laser diode is operating on single-mode and the voltage signals amplitudes are decreasing with injection current resulting on a good agreement with the derived model. As soon as a second mode appears, it leads to the increment of the voltage signal amplitude with laser injection current.

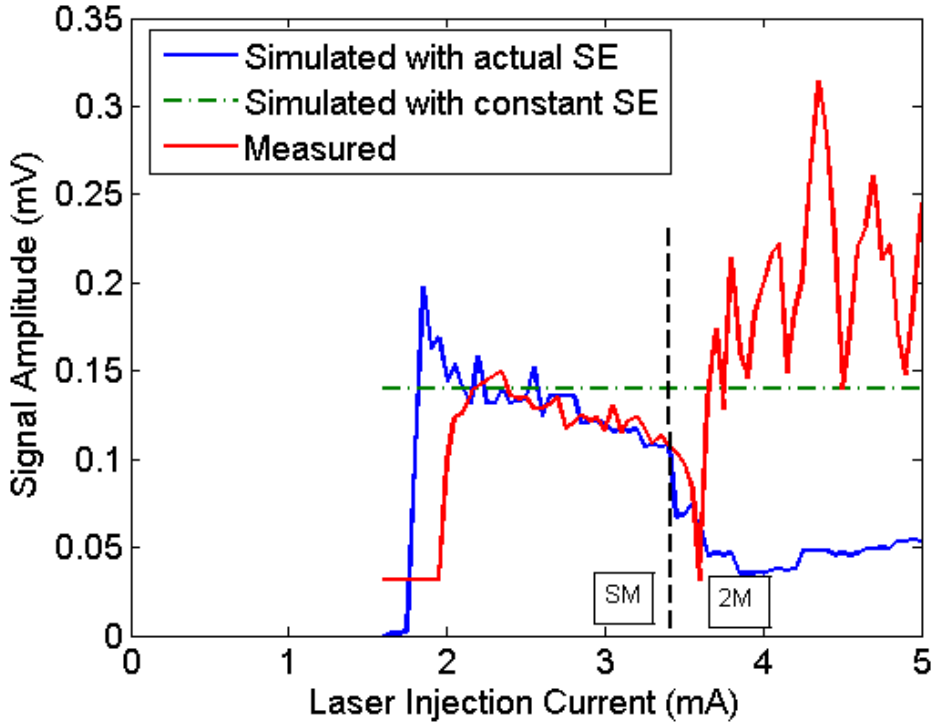

Fig. 3.22: Evolution of the amplitude of the voltage OFI signal with laser injection current in the two-mode VCSEL. Solid blue line: simulated taking into account the actual slope efficiency; dashed line: simulated with constant slope efficiency; red solid line: measured.

b) Multimode VCSEL

The same experiment has been performed using a multimode VCSEL from Optek (model OPV310Y). Fig. 3.23 shows the evolution of the PD signal amplitudes (measured signal and signals simulated using either an ideal and the actual slope efficiencies) with laser injection current for this VCSEL. At low injection currents, the amplitude of the PD signal increases with injection current. However, despites it keeps increasing for higher injection currents, the signal amplitude is pretty unstable and does not seem to be strongly correlated to the laser biasing level.

As for the LV signals, the evolution of the amplitudes in multimode laser diodes is quite interesting compared to those of single-mode laser diodes. In single-mode laser diodes, the LV signals amplitudes would decrease with the increment of injection current due to the decrement of the slope efficiencies with injection current. However, as shown in Fig. 3.24, the LV signal in the multimode VCSEL increases strongly with laser injection current after 4 mA.

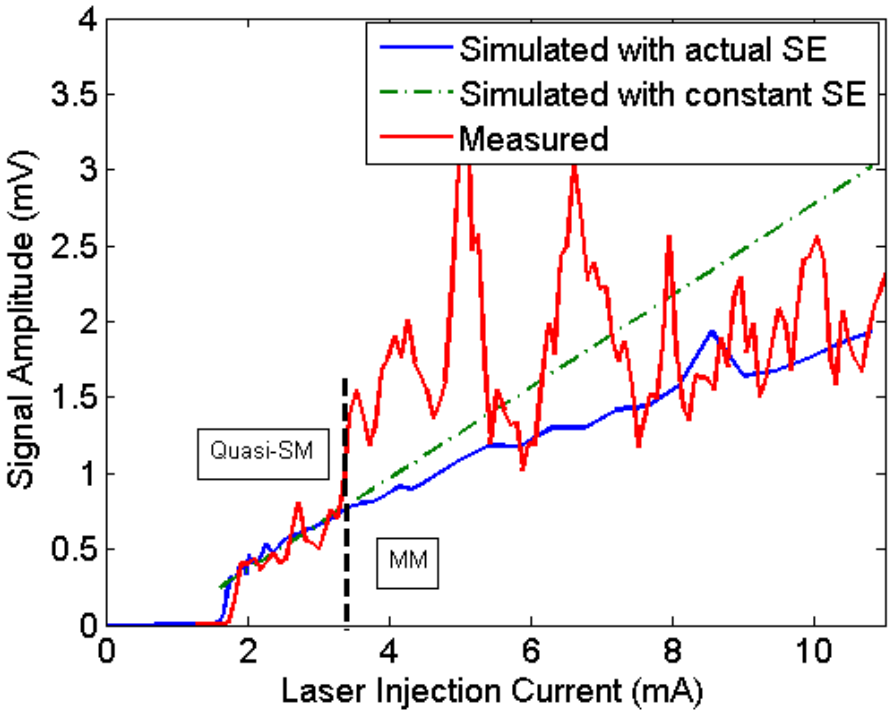

Fig. 3.23: Evolution of the PD OFI signal amplitude with laser injection current in the two-mode VCSEL.

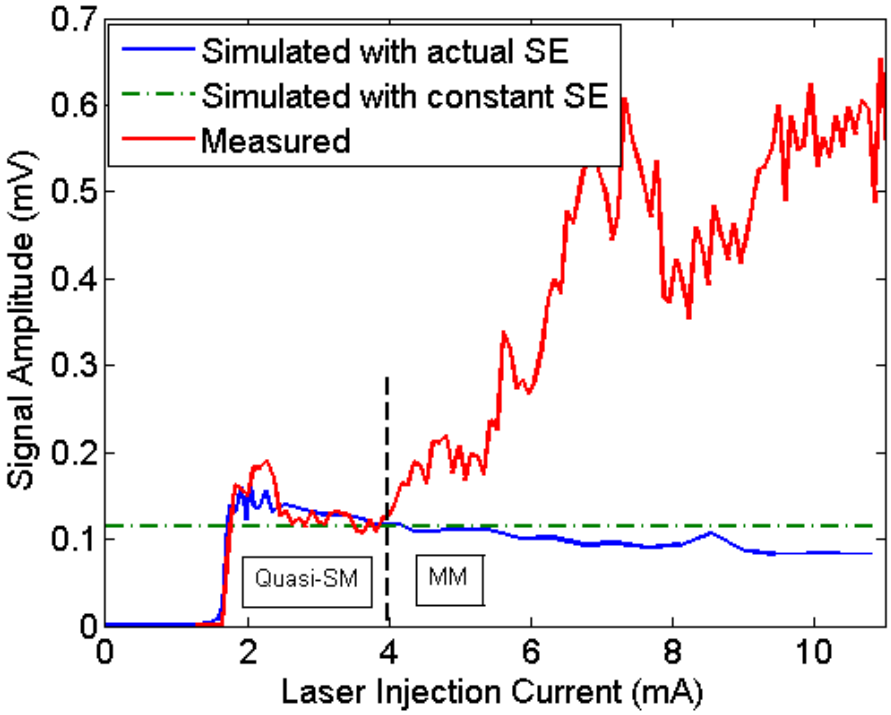

Fig. 3.24: Evolution of the amplitude of the voltage OFI signal with laser injection current in the multimode VCSEL.

Therefore, it is quite clear for us right now that the model shows good agreement with experimental results for single-mode laser diodes. Moreover, in laser diodes that operate on a single-mode for part of the injection current range before more modes appear, the analytical model is still validated for both PD and LV signals. Once a laser diode is operating on multi-modes, the LV signal is not decreasing anymore with the injection current.

3.4 The case of the front PD signal

So far in this chapter, we have discussed the experimentally obtained OFI PD and LV signals in a DFB laser diode and a VCSEL. The laser power photodetected (PD) signals were obtained through the photodiode displayed in the laser diode package that is usually used to monitor the laser output power. In the case of in-plane laser diodes (such as: Fabry-Pérot, DFB and DBR) the monitor photodiode is placed at the rear facet of the laser diode. However, when a monitoring photodiode is not included in the laser diode package or when it is not possible to have it placed at the rear facet (as with VCSELs), a portion of the front facet output power can be used to acquire the OFI signal.

In this section, we compare the evolution of the experimentally obtained PD signals from both acquisition schemes, in both phase and amplitude, with laser injection current.

3.4.1 Comparison of the amplitudes of the front and the back PD signals

In chapter 2, we have derived the following expression that describes the evolution of the modulation indices ratio with injection current:

$$M_R = 1 - \frac{\tau_L}{\tau_p}\frac{R_2}{T_2}\left(\frac{I - I_{th}}{I - \frac{N_{tr}}{N_{th}}I_{th}}\right) \tag{3.5}$$

Expression (3.5) predicts a sign inversion which corresponds to a 180 phase shift between the front and back PD signals at a given injection current. Let's call this current the crossover current and let's denote it as I_{CR}. Then, just above threshold, while the condition $I<I_{CR}$ is achieved, the ratio is positive and both PD signals are in-phase. Increasing the laser injection current leads to a gradual decreasing in the ratio, which means that the front PD signal increases less than the back PD one, or even that it decreases. At the crossover current, the ratio becomes zero thus meaning that the front PD signals cancels out. A further increment of the injection current leads to a negative ratio thus indicating that both signals are out-of-phase and that the front PD signal increases with the laser injection current again.

Furthermore, despite the fact that the divergence of both PD signal is a direct consequence of the back-scattered power that is reflected by the laser front mirror, the expression states that the ratio does not depend directly on any external cavity/target parameter and amongst them, most surprisingly the external reflectivity R_{ext} and thus the optical feedback strength. To confirm the prediction of the model, we have performed the measurements of both signal amplitudes for the full range of the laser injection current and for different attenuation levels and we have extracted the corresponding ratios.

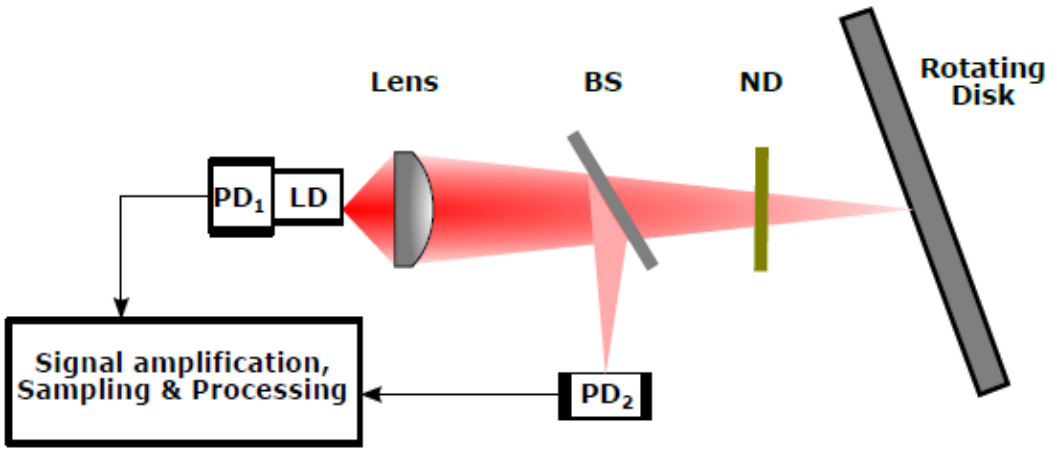

Fig. 3.25: Experimental setup used for the simultaneous measurement of the front and back PD signals.

The measurements presented here were performed on the DFB laser diode described in section 1 using the experimental setup shown in Fig. 3.25. Both PD signals were measured concurrently, and were fed to similar trans-impedance

amplifiers. However, due to slightly different configurations of the amplification circuits, an intrinsic phase difference of 50° was measured at the Doppler frequency.

Fig. 3.26 shows the temporal back PD signal (top) and the front PD signal (bottom) measured at different values of injection current when no attenuators are introduced to the optical path. In Fig. 3.26(a), the injection current of 6 mA is slightly above threshold and both signals are in-phase. Increasing the injection current to 9 mA, the front PD signal is reduced to mere noise as shown in Fig. 3.26(b) indicating that it is very close to the crossover current. At 16 mA, the front PD signal changes sign of the amplitude which corresponds to a phase shift of 180° and both PD signals are out-of-phase.

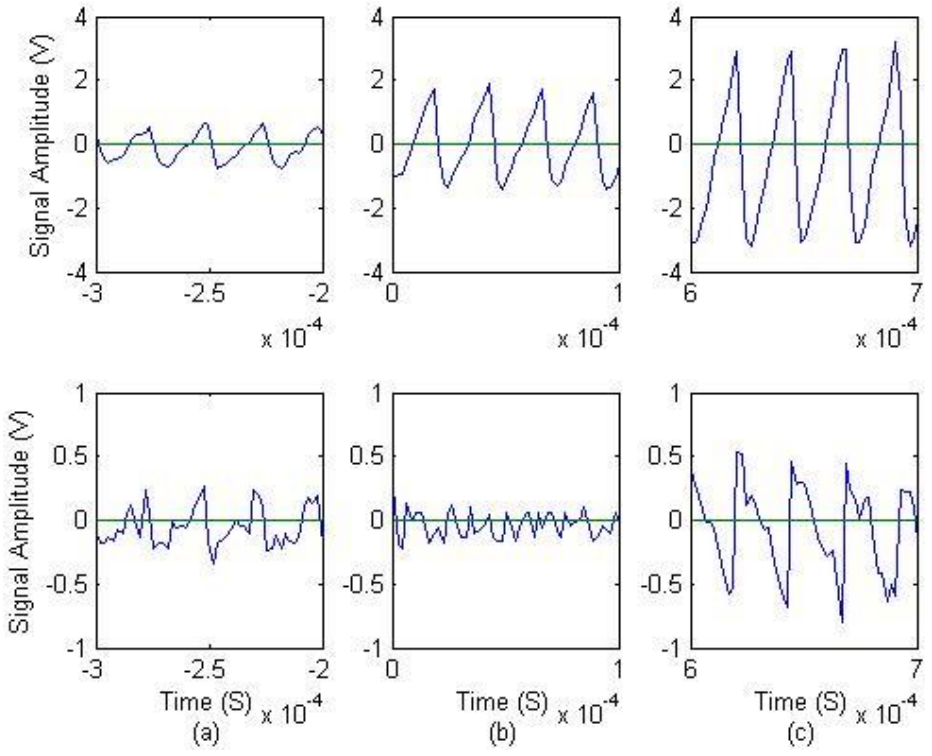

Fig. 3.26: Back (upper plots) and front (lower plots) PD signals at different bias currents: a) I = 6 mA, PD signals are in-phase, b) I = 9 mA, front PD signal vanishes, c) I = 16 mA, signals are out-of-phase.

The PD model equation derived in the previous chapter shows that the amplitude of the PD signal increases linearly with injection current. This result has been validated in this chapter for the back PD signal. Here, we compare the evolution

of the amplitudes of both PD signals with injection currents for different optical feedback levels, as show in Fig. 3.26.

Fig. 3.27(a) shows the evolution of their amplitudes when no neutral densities are introduced to the optical path and the optical feedback is the strongest. As validated before, the back PD signal amplitude is a linearly increasing function of injection current. On the other hand, the front PD signal has a peak just above threshold, and then it decreases with the increment of injection current until it becomes zero at 9 mA, the crossover current. Beyond this current, the front PD signal is almost a linearly increasing function of the injection current.

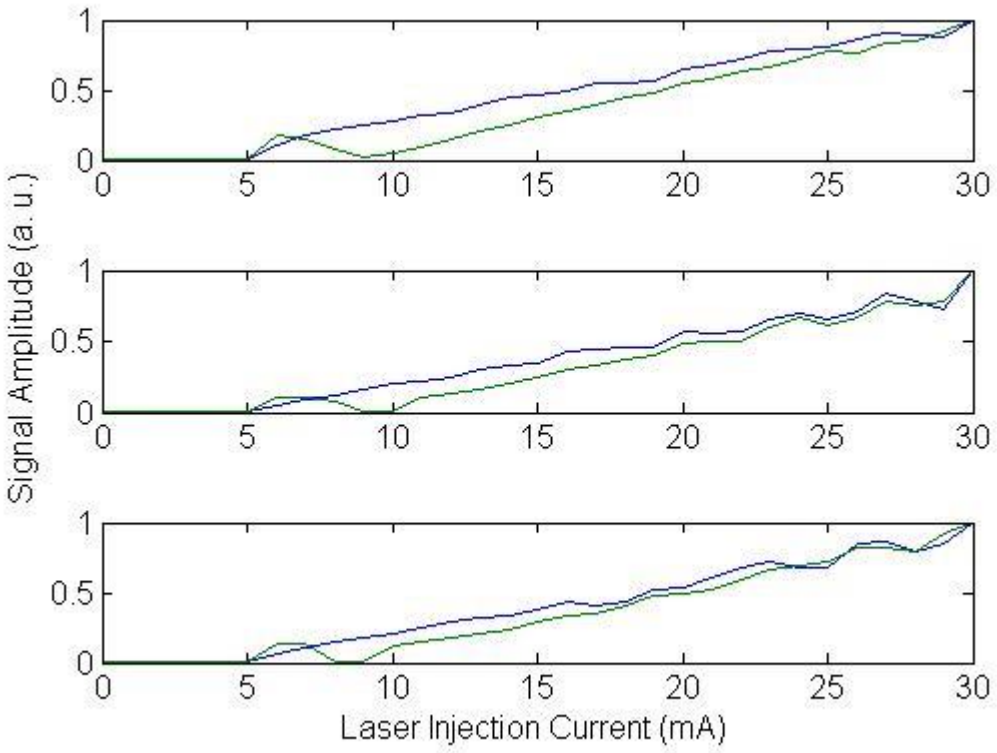

Fig. 3.27: Evolution of the amplitudes of the back (blue trace) and front (green trace) PD signals with laser injection current at different attenuation levels: top) No neutral density is introduced to the optical path; middle) Attenuation level is 16 dB; bottom) Attenuation level is 20 dB.

Fig. 3.27(b) and 3.27(c) shows the evolution of both PD signals with injection current when the round-trip attenuation is 16 dB and 20 dB respectively. The behaviour of both signals is absolutely identical as the ones observed without optical densities in the path.

Fig. 327(c) shows the evolution of both PD signals with injection current when the attenuation level is 20 dB. The corresponding average photocurrents measured over the injection current range with the monitoring and the external photodiodes for the three different configurations are shown in Fig. 3.28. As expected, the introduction of neutral densities in the optical path after the beam splitter does not affect the mean power photodetected.

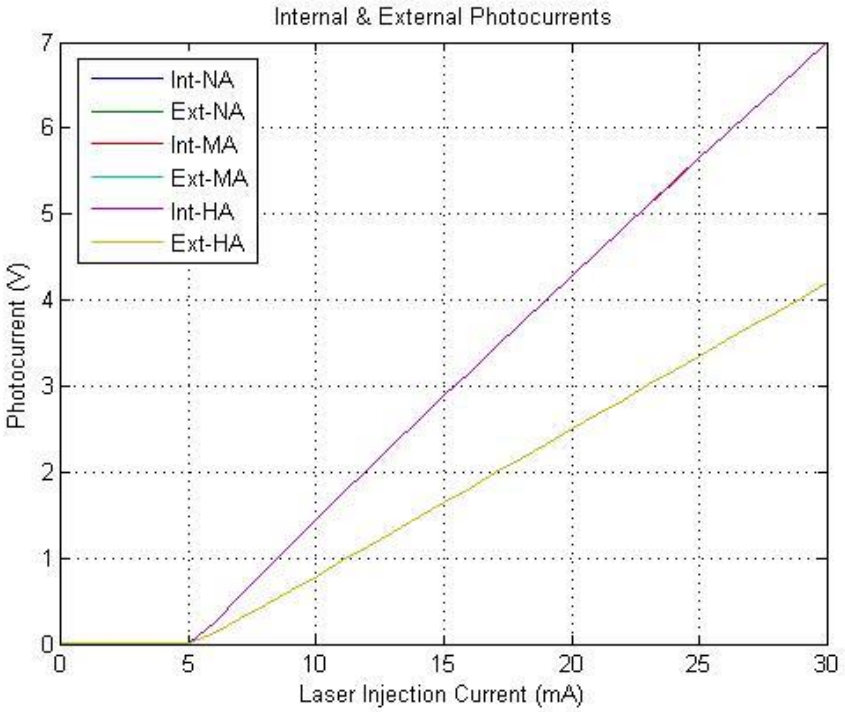

Fig. 3.28: Photocurrents as a function of the laser injection current measured at different attenuation levels (purple solid line for the external photodiode, and golden solid line for the built-in monitoring photodiode).

3.4.2 Phases of front and back PD signals

As mentioned before, the derived model predicts a 180° phase shift in the phase of the front PD signal for injection currents higher than the crossover current. However, at low injection current and/or with high attenuation in the external cavity, the low amplitudes of the signals as compared to the noise levels do not allow an easy and direct observation of the phase shift between the two signals in time domain. In order to validate ours model, Matlab's FFT algorithm

was applied to the acquired signals and the phase difference between the FFT phases spectra was calculated.

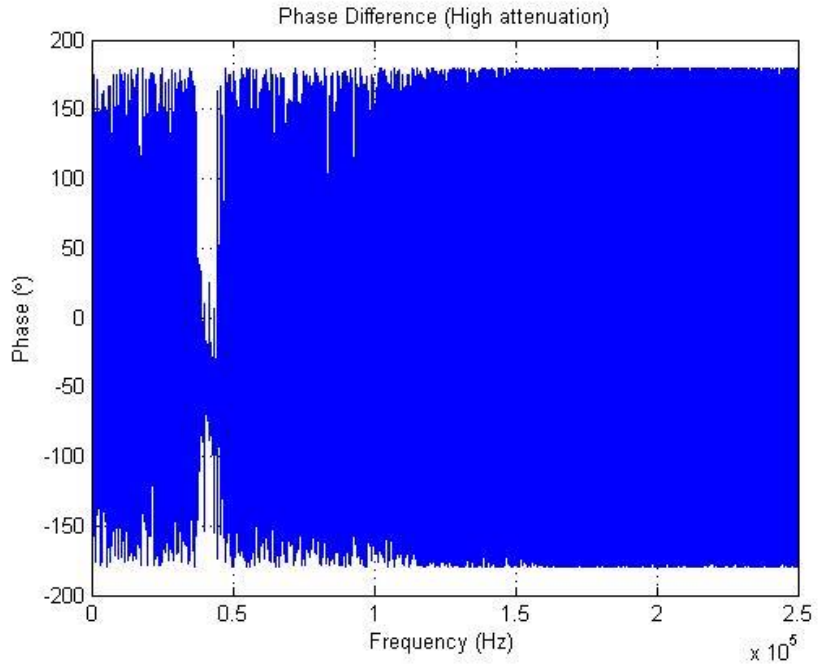

(a)

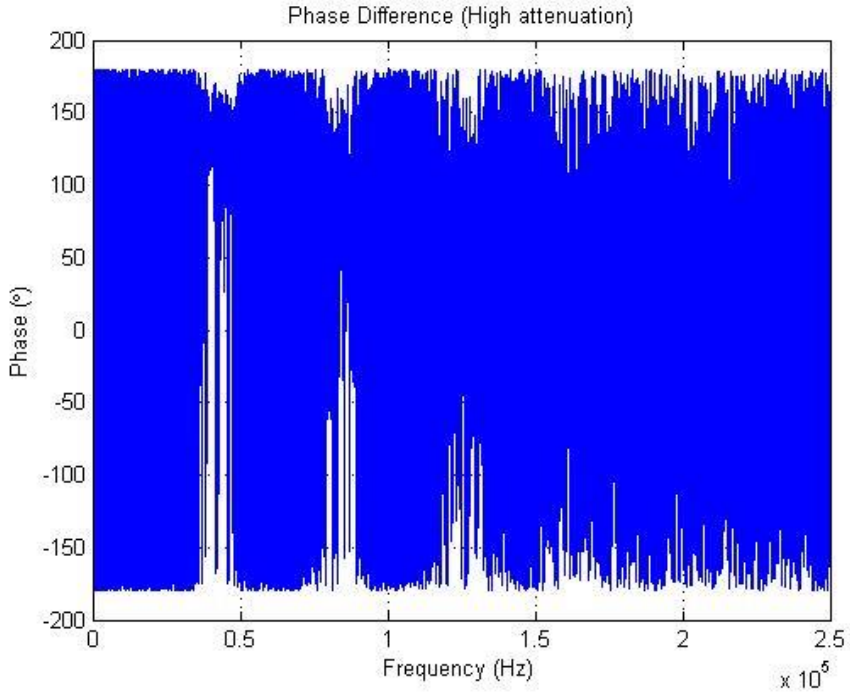

(b)

Fig. 3.29: The phase difference as a function of frequency at: a) 7 mA, and b) 27 mA.

As an illustration, the phase difference as a function of the frequency with I = 7 mA and no neutral densities is shown in Fig. 3.29(a) while similar plot for I = 27 mA (>I_c) is shown at Fig. 3.29(b).

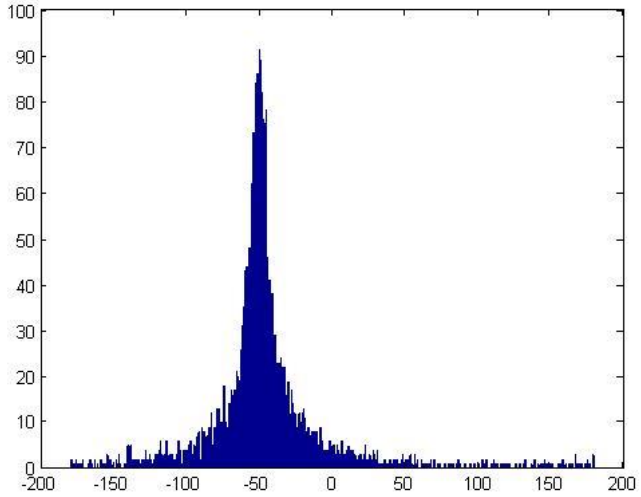

(a)

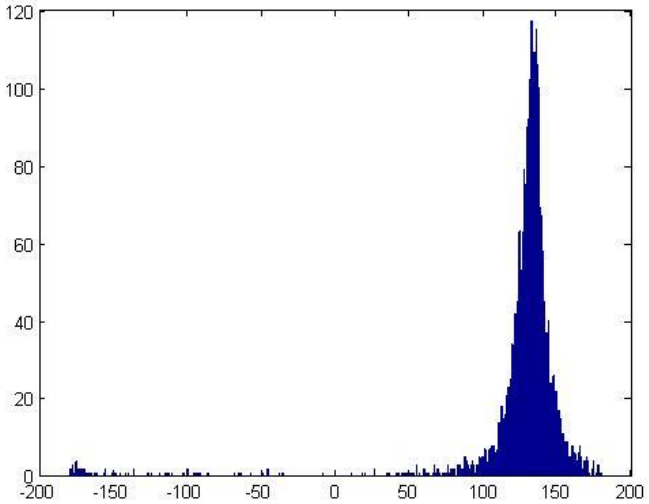

(b)

Fig. 3.30: Histogram of the phase difference at: a) 7 mA, and b) 27 mA.

From Fig. 3.29, the phase difference around the Doppler frequency ranges from -40° to - 60° at 7 mA and ranges from 120° to 150° at 27 mA. The deviation from zero in phase difference at 7 mA is due the pre-mentioned phase shift of the two amplifiers at the Doppler frequency.

Afterwards, the histograms of the frequencies which lie within the interval bounded by 0.9 and 1.1 of the Doppler frequency were generated. Fig. 3.30(a) shows the histogram of the phase difference at 7 mA while Fig. 3.30(b) shows the phase difference histogram at 27 mA. The corrected phase-shifts (by the addition of 50° to each value) are shown in Fig. 3.31.

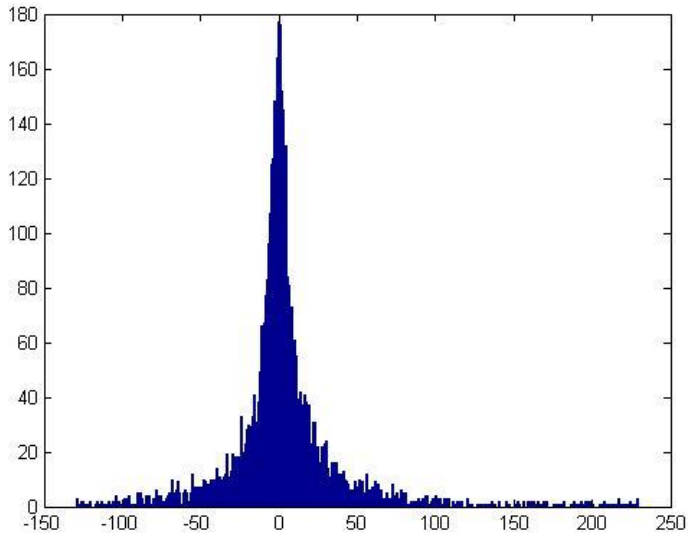

(a)

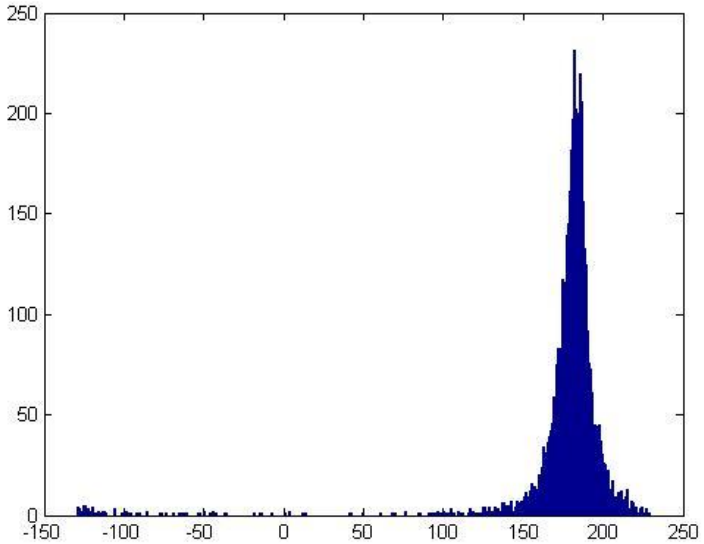

(b)

Fig. 3.31: Histogram of the corrected phase difference at: a) 7 mA, and b) 27 mA.

Gaussian fitting is then applied to the histograms to allow precise determination of the phase difference mean value. Therefore, at 7 mA, the phase difference is 0° while at 27 mA it is 180°.

Applying the same process at every injection current along the entire current range for the different attenuations levels, we end up with the phase differences as a function of injection current shown in Fig. 3.32.

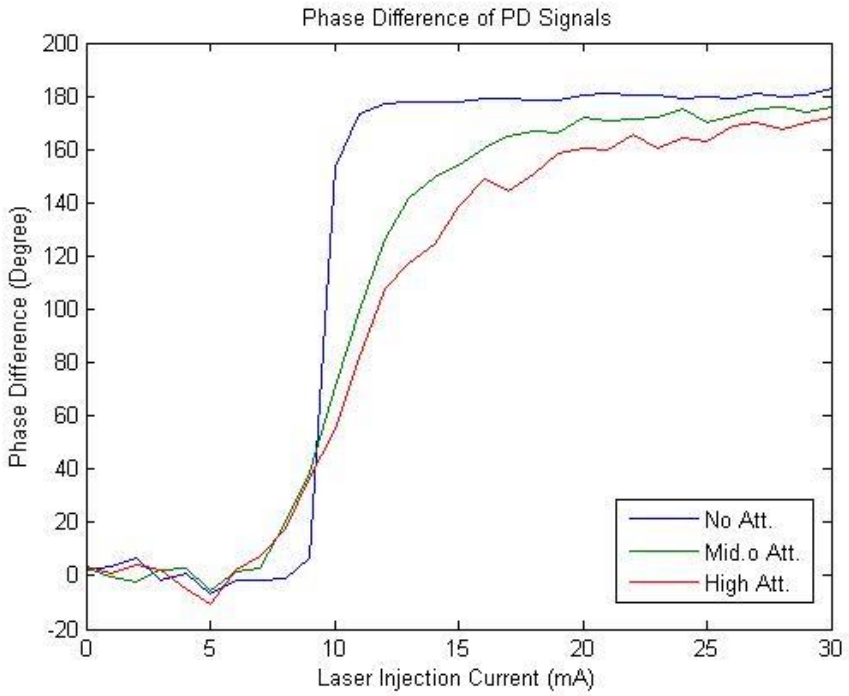

Fig. 3.32: Phase differences as a function of the laser injection current measured at different attenuation levels (blue solid line for the case of no attenuation; green solid line for the case of 16 dB attenuation; and red solid line for the case of 20 dB attenuation).

As predicted by the model, the back and the front PD signals are in-phase for injection currents lower than the crossover current while they are out-of-phase for higher injection currents. The value of the cross-over does not depend on the optical feedback level or any external cavity parameters.

3.4.3 Ratio of modulation indices

In this section, we combine both the phase and amplitude evolution of the back and front PD signals with injection current in one term which is the ratio of the modulation indices expressed in eq. (3.5).

The ratio of modulation indices was modelled with the consideration of the intrinsic laser parameters given in Table 3.3. The photon lifetime and the internal round-trip delay time are the standard values given in [147], while the values of the power reflection coefficient of the front mirror and the ratio of the carrier densities at transparency and threshold were calculated so that the measurement and simulation curves fit. A comparison of the standard values of the ratios (the ratio of the carrier densities at transparency and at threshold, and the ratio of the power reflectivity to the power transmission coefficient of the front facet) given in [147] and the fitted values are shown in Table 3.4.

Parameter	Value
n	3.21
L	250 μm
τ_L	5.35 ps
τ_P	2.77 ps
N_{tr}/N_{th}	0.7
R_2/T_2	0.72

Table 3.3: Laser parameters used for the calculation of the model curves

Parameter	Standard Value	Fitted Value
N_{tr}/N_{th}	0.42 [147]	0.70
R_2/T_2	0.11	0.72

Table 3.4: Comparisons of the fitted and the standard values of: (i) the ratios of the carrier densities at transparency and at threshold, and (ii) the ratio of the power reflectivity to transmission coefficients of the front facet.

Fig. 3.33 shows the modelled ratio as well as the experimentally obtained ones for the three different levels of optical feedback. The modelled curve shows good agreement with experiments. The experimental curves show a fairly good agreement with the analytical model curves, proving that the ratio of the modulation indices does not depend on any external cavity parameters, and in particular R_{ext}. Moreover, the measurement of the ratio of modulation indices of a laser diode can be used to determine some of the laser parameters such as the ones listed in Table 3.4.

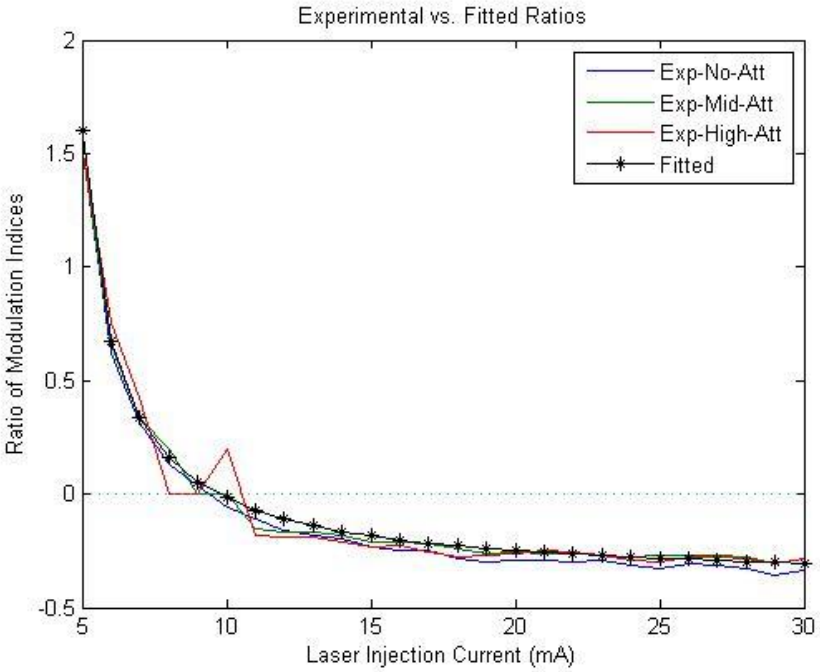

Fig. 3.33: Ratio of modulation indices as a function of the injection current both modelled (black solid line) and measured at different attenuation levels (blue solid line for the case of 0 dB attenuation; green solid line for the case of 16 dB attenuation; and red solid line for the case of 20 dB attenuation).

Chapter 4

Improvement of the OFI Sensor Sensitivity using Multiple Acquisition Schemes

Acquisition of OFI signals, as discussed in previous chapters is possible from three different available sources: the laser junction voltage, the photodetection of the front emission power and the photodetection of the back emission power. In the previous chapters, we have experimentally demonstrated the proposed analytical model that describes the evolution of both photodetected signals (PD) and the amplified laser voltage signal (LV) with the laser injection current, the temperature and the system intrinsic parameters. Furthermore, the phase and amplitude relationships of the front and back PD signals have been investigated thoroughly.

In this chapter, we investigate different signal processing techniques on either two of the three OFI signals, and then we compare the results in search of any noticeable improvements in the characteristics of the signals, and in particular the SNR. The proposed investigation is based on the hypothesis that the acquisition of the same informative signal through two different sources shall be emphasizing the signal while suppressing the noise. Signal processing techniques performed in this chapter are autocorrelation, cross-correlation, and the simple arithmetic addition/subtraction operations.

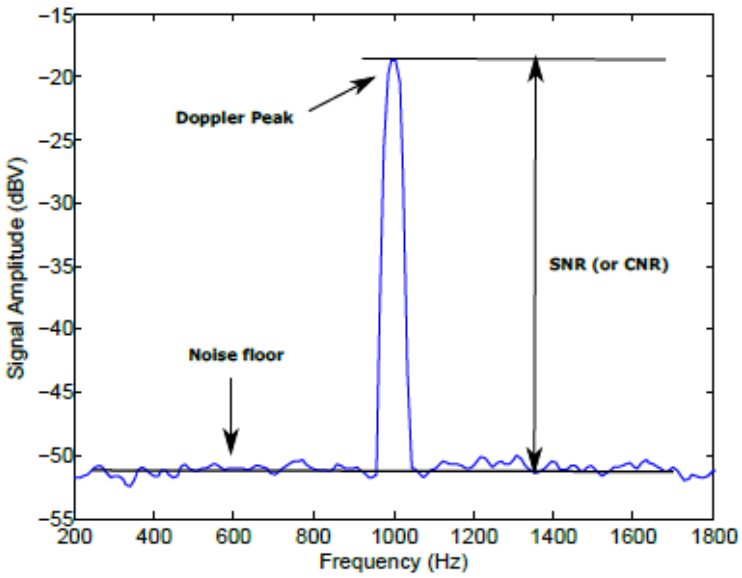

Fig. 4.1: Spectrum of a noisy sinusoidal signal with a frequency of 1 kHz and an amplitude of 1, accompanied by a white Gaussian noise with a standard deviation of 0.2. The SNR in decibel is measured as the difference between the signal amplitude at 1 kHz and the average noise level elsewhere

The criteria used to evaluate the improvement due to signal processing is the carrier-to-noise ratio (CNR) rather than the SNR. The CNR, analogous to the term used in telecommunications, is defined as the ratio of the carrier power (i.e. the power at the Doppler frequency in our case) to the noise power at the carrier frequency. Fig. 4.1 shows a graphical explanation of such term. However for sake of simplicity, in this chapter the term SNR will be used.

4.1 Description of the Experimental Setup

In order to permit the application of signal processing techniques accurately, OFI signals should be acquired concurrently. Therefore, we have performed a set of measurements at different values of injection currents using the simple Doppler velocimeter shown in Fig. 3.25.

The measurements were performed using the same DFB laser diode (ML725B11F, λ = 1310nm) from the model validation measurements (chapter 3). The setup itself is quite similar to the one used to validate the rate equation modelling: same target, lens, beam splitter and neutral density filters.

In the previous chapter, the amplified OFI signals were fed to a DAC where a Labview program was used to save the data. In this experiment, the DAC was replaced by an oscilloscope with a sampling rate of 20 M samples/s. The high sampling rate that was not achievable with NI DAC system allows concurrent display without any noticeable acquisition induced phase shift and strongly limits the aliasing noise in the acquired signals. Up to 2.5 M samples of each signal were saved in every measurement for signal processing.

All signal processing has been performed using Matlab^{TM} algorithms. SNRs of these signals, once processed were calculated in the frequency domain, at the central Doppler frequency, using the exact same method described in the previous chapter.

4.2 Theoretical Background

As OFI signals acquired from different sources have different amplitudes and noise characteristics, it is essential to first understand the concepts of the signal processing techniques before applying them on those signals. Hence, we start with a brief introduction to every signal processing technique, followed by the processing of two model monochromatic noisy signals. Different scenarios are considered for the amplitudes, phases and noise levels of the model signals to widen the scope of the conclusion.

4.2.1 Noise sources in different acquisition schemes

Despite a more accurate study would be required to model the noise in OFI sensors, a brief analysis of the origin of the noise in the OFI sensing context is useful to identify qualitatively the contributions to noise.

In the case of the photodetected signals, the main noise sources are:

1. laser intensity noise,
2. photodiode Shottky noise,
3. amplifier noise

In the case of the voltage signal, the main noise sources are:

1. laser diode Shottky noise
2. amplifier noise.

In the usual frequency domain of the OFI sensing (1 kHz – 100 MHz), all these noise contributions can be considered as white noise source.

Also, one can notice that combining both photodetected signals, the photodiode Schottky noise and the amplifier noise are independent noise sources while the laser intensity noise remains the only common noise source. In the case of a combination of the laser voltage signal with any of the photodetected signals, only the laser diode Shottky noise will remain common to the two signals since it is strongly present in the laser intensity noise [111].

4.2.2 The applied signal processing techniques

Let's now consider two continuous-time noisy signals represented as:

$$x(t) = f_1(t) + n_1(t) \tag{4.1}$$

$$y(t) = f_2(t) + n_2(t) \tag{4.2}$$

where $f_*(t)$ is the clean source signal while $n_*(t)$ is the corresponding additive white noise signal. In the frequency domain, we get:

$$X(f) = F_1(f) + N_1(f) \tag{4.3}$$

$$Y(f) = F_2(f) + N_2(f) \tag{4.4}$$

The SNRs of either signal then can be defined as:

$$SNR_* = \frac{S_*}{N_*} \tag{4.5}$$

where S_* and N_* denote the powers of the signal and the noise, respectively. Since the considered noise is a white Gaussian noise with a zero mean and a variance of σ^2, it will have a perfectly flat power spectrum, with $N = \sigma^2$.

Given two continuous-time signals, $x(t)$ and $y(t)$, the autocorrelation of $x(t)$ is defined as:

$$r_{xx}(\tau) = \lim_{T\to\infty} \frac{1}{2T} \int_{-T}^{T} x(t).x(t-\tau)\, dt \tag{4.6}$$

while the cross-correlation functions between the two signals are defined as:

$$r_{xy}(\tau) = \lim_{T\to\infty} \frac{1}{2T} \int_{-T}^{T} x(t).y(t-\tau)\, dt \tag{4.7}$$

$$r_{yx}(\tau) = \lim_{T\to\infty} \frac{1}{2T} \int_{-T}^{T} y(t).x(t-\tau)\, dt \tag{4.8}$$

From the mathematical definitions given above, the correlation functions can be simply thought of as the mean of the products of all pairs of points of a signal and the time-shifted version of itself for autocorrelation or of the other signal for cross-correlation [156, 157]. The correlation functions are applied to measure the similarity between the input signals as a function of the time-lag, and used in finding repeating patterns, such as the presence of a periodic signal obscured by noise, or identifying the missing fundamental frequency in a signal implied by its harmonic frequencies. For real signals, expressions (4.7) and (4.8) are equal.

Substituting eq. (4.1) in the expression of autocorrelation from eq. (4.6), we obtain:

$$\begin{aligned} r_{\mathrm{xx}}(\tau) = x(t) \star x(t) &= [f_1(t) + n_1(t)] \star [f_1(t) + n_1(t)] \\ &= f_1(t) \star f_1(t) + f_1(t) \star n_1(t) + n_1(t) \star f_1(t) \\ &+ n_1(t) * n_1(t) \end{aligned} \tag{4.9}$$

From eq. (4.9), we get that for a noisy signal, the autocorrelation function could be interpreted as the sum of the autocorrelation of the clean source signal, the autocorrelation of the noise signal and the cross-correlations of each signal with the conjugate of the other. The middle terms are equal in the case of purely real signals.

The power spectral density can be computed from eq. (4.9) as follows:

$$|X(f)|^2 = |F_1(f)|^2 + F_1(f).{N_1}^*(f) + {F_1}^*(f).N_1(f) + |N_1(f)|^2 \tag{4.10}$$

The last three terms on the right side of the eq. (4.8) cannot be measured directly, but they could be estimated. The SNR of the autocorrelation output then can be evaluated using the following expression:

$$SNR_{\mathrm{XX}} = \frac{{S_1}^2}{\sqrt{(S_1.N_1)^2 + (N_1.S_1)^2 + ({N_1}^2)^2}} \tag{4.11}$$

If the noise and the signals are independent, then they are uncorrelated [156, 158] and the terms $F_1(f).N_1{}^*(f)$ and $F_1{}^*(f).N_1(f)$ reduce to zero. Thus, eq. (4.11) can be simplified into:

$$SNR_{\mathrm{XX}} = \frac{{S_1}^2}{{N_1}^2} = {SNR_X}^2 \tag{4.12}$$

From which, we can clearly notice that the SNR of the autocorrelation output is the square of the SNR of the input signal. The SNR is usually expressed in the logarithmic decibel scale. Hence, eq. (4.12) means that the SNR of the output is twice that of the input noisy signal.

Likewise, when we substitute eq. (4.1) and eq. (4.2) in the expression of autocorrelation from eq. (4.7), we get:

$$\begin{aligned} r_{\mathrm{xy}}(\tau) = x(t) \star y(t) &= [f_1(t) + n_1(t)] \star [f_2(t) + n_2(t)] \\ &= f_1(t) \star f_2(t) + f_1(t) \star n_2(t) + n_1(t) \star f_2(t) \\ &\quad + n_1(t) \star n_2(t) \end{aligned} \tag{4.13}$$

From which, we can represent the cross-correlation of two noisy signals as the sum of the cross-correlation of the clean signals, the cross-correlation of the noise signals and the cross-correlations of each clean signal with the conjugate of the noise signal of the other.

Then, the power spectral density of the cross-correlation output $\left|R_{xy}(f)\right|^2$ can be expressed as:

$$\begin{aligned} \left|R_{\mathrm{xy}}(f)\right|^2 &= |F_1(f)|.|F_2(f)| + F_1(f).N_2{}^*(f) + F_2{}^*(f).N_1(f) \\ &\quad + |N_1(f)|.|N_2(f)| \end{aligned} \tag{4.14}$$

and the SNR of the cross-correlation output can be calculated using the following equation:

$$SNR_{\mathrm{XY}} = \frac{S_1.S_2}{\sqrt{(S_1.N_2)^2 + (N_1.S_2)^2 + (N_1.N_2)^2}} \tag{4.15}$$

Again, if the noise and the signals are independent, then they are uncorrelated. Omitting the middle terms on the right side of eq. (4.14), eq. (4.15) is simplified into:

$$SNR_{\mathrm{XY}} = \frac{S_1.S_2}{N_1.N_2} = SNR_X.SNR_Y \tag{4.16}$$

or that the SNR of the cross-correlation output is the product of those of the input signals. Hence, in logarithmic scale, the SNR of the cross-correlation output is equivalent to the sum of the SNRs of the input noisy signals.

Both autocorrelation and cross-correlation signal processing techniques are evaluated and compared in this chapter.

A third technique is compared to these two techniques, which is the arithmetic addition or subtraction of the two input signals. However this last method depends on the phase-shift, θ, between the input signals.

Now, let's assume that the clean signals given in (1) and (2) are two periodic functions, where one signal can be expressed from the other as follows:

$$f_2(t) = K.e^{-j\theta}.f_1(t) \tag{4.17}$$

where K is a constant and Θ is the phase difference between the two signals. The sum of those two signals can then be expressed as:

$$\begin{aligned} x(t) + y(t) &= f_1(t) + n_1(t) + f_2(t) + n_2(t) \\ &= \{(1 + K.cos(\Theta)).f_1(t) + jK.sin(\Theta).f_1(t)\} \\ &\quad + n_1(t) + n_2(t) \end{aligned} \tag{4.18}$$

Hence, the SNR of their sum can be evaluated through:

$$\begin{aligned} SNR_{\mathrm{sum}} &= \frac{S_1(1 + K.cos(\Theta))^2 + S_1.K^2.sin^2(\Theta)}{N_1 + N_2} \\ &= \frac{(1 + 2K.cos(\Theta) + K^2).S_1}{N_1 + N_2} \end{aligned} \tag{4.19}$$

If both input signals have equal amplitudes and noise levels (i.e. $K=1$ *and* $N_1 = N_2$), then the SNR of the sum can be expressed in terms of the SNR of either input signal as follows:

$$SNR_{\text{sum}} = \frac{(1 + cos(\Theta)).2S_1}{2N_1} = (1 + cos(\Theta)).SNR_X \tag{4.20}$$

In this case, the highest improvement in SNR using the addition of equivalent deterministic signals is achieved when both signals are in-phase, yielding:

$$SNR_{\text{sum}} = \frac{4S_1}{2N_1} = 2.SNR_X \tag{4.21}$$

which means that the improvement in the SNR of output clean signal is 6 dB, whereas the rise in the resultant noise level is 3 dB. Thus, the SNR of the sum signal is merely 3 dB higher than that of the SNR of input signals. However, if the phase shift was π/2, no improvement in the SNR will be achieved. Moreover, for a phase shift of π, both input signals will cancel out each other leaving the noise only.

In general, when the two input signals have equal amplitudes and noise levels, their sum would yield up to 3 dB improvement in SNR for $0 \leq \theta < \frac{\pi}{2}$, and less than the SNR of either input signal for. $\frac{\pi}{2} < \theta \leq \pi$. Actually, for the latter case, the SNR of the difference is what should be evaluated in order to improve the SNR using the following equation:

$$\begin{aligned} SNR_{\text{diff}} &= \frac{S_1(1 - K.cos(\Theta))^2 + S_1.K^2.sin^2(\Theta)}{N_1 + N_2} \\ &= \frac{(1 - 2K.cos(\Theta) + K^2).S_1}{N_1 + N_2} \end{aligned} \tag{4.22}$$

Even when the input signals are in-phase, the 3 dB improvement won't be achieved except when the input signals have equal amplitudes and noise levels. Other than that, the SNR of both the sum and the difference would always be less than 3 dB higher than the highest SNR of the input signals.

4.2.3 Validation on ideal signals

In this subsection, we apply the signal processing techniques discussed above on ideal signals. The model signals are monochromatic noisy signals,

where the noise term is a zero-mean additive white Gaussian noise. The literal expressions of these signals are:

$$x(t) = A.sin(2\pi f_0 t) + B.n_1(t) \tag{4.23}$$

$$y(t) = C.sin(2\pi f_0 t + \Theta) + D.n_2(t) \tag{4.24}$$

where A and C are the amplitudes of the clean sinusoidal signals, B and D are the standard deviations of the noise signals, f_0 is the frequency of the sinusoidal signals, and θ is the phase difference between the clean sinusoidal signals (also called the phase shift of $y(t)$). The additive white Gaussian noise signal, $n_*(t)$, is represented by the zero-mean normal distribution function **randn**, which amplitude is the standard deviation, σ.

This phase shift has a great impact on the SNR of the arithmetic signal processing technique output. In the previous chapter, we have already investigated the phase relationships among the OFI signals. Moreover, we have demonstrated that the PD signals are in-phase below the cross-over current, and out-of-phase above it. Hence, we will first demonstrate the influence of the phase shift on the outputs of the different signal processing techniques.

The SNR of a sinusoidal signal with amplitude of A, accompanied by a white noise with a standard deviation of σ, is given by:

$$SNR_{\mathrm{dB}} = 10\ log_{10}\frac{0.5\ A^2}{\sigma^2} \tag{4.25}$$

a) The impact of the phase shift on the SNR of the sum

Here, we will consider the case where both input signals are equal in amplitudes and noise levels. Hence, each input signal is a sinusoidal signal with a frequency of 1 kHz, an amplitude of 1 (i.e. A = C = 1), and a standard deviation of 0.2 (i.e. B = D = 0.2). From eq. (2.5), such a signal has a SNR of 10.97 dB. Table 4.1 shows the calculated and the obtained SNRs for different values of the phase shift.

Phase Shift θ	Calculated SNR_{sum}	Evaluated SNR_{sum}	Calculated SNR_{XY}	Evaluated SNR_{XY}
0	14	14	21.9	21.9
π/4	13.3	13.4	21.9	21.8
π/2	11	10.9	21.9	21.9
3π/4	5.6	5.7	21.9	22.0
π	0	0.2	21.9	21.9

Table 4.1: SNRs of the output signals: a) calculated using the presented formulas, and b) evaluated from the simulated spectra.

The SNRs of the sum output were calculated using eq. (4.20), whereas the SNR of the cross-correlation was calculated using eqn. (4.16) for the in-phase relationship only. Here, it is clear that the phase shift has a negligible effect on the outputs of the correlation functions which is to be expected since the correlation functions themselves are based on the shifting of one signal relative to the other, which has a minor effect on the results when performed on a signal with a large number of oscillations. However, the phase shift has a major effect on the outputs of the arithmetic operations as explained earlier in this chapter.

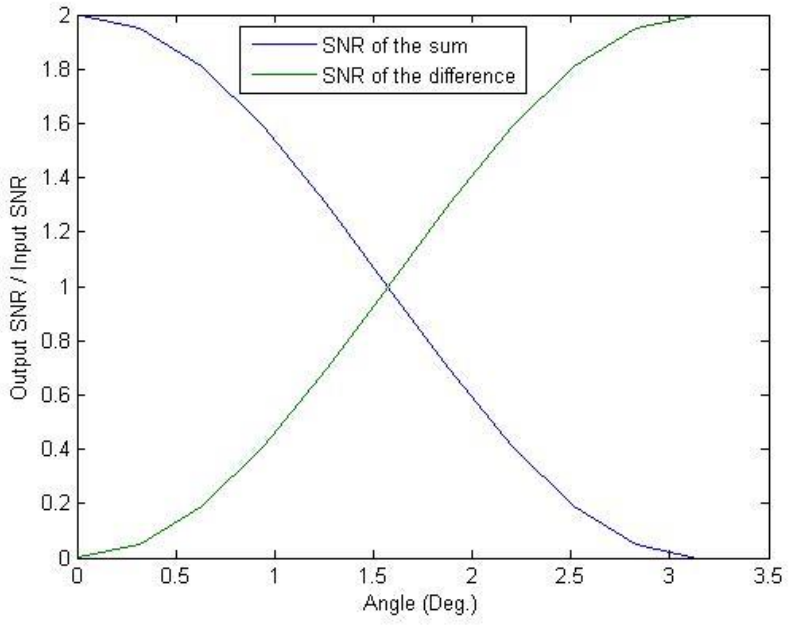

Fig. 4.2: The sum and the difference SNRs of the input signals as a function of the phase shift (solid blue is the sum, and solid green is the difference). The SNRs of the input signals are equal and are normalised at 0.

From the table, a maximum of 3 dB improvement in the SNR is obtained for in-phase signals while both signals cancel out each other when they are out-of-phase. Moreover, an improvement in the SNR of the sum signal occurs only when the phase shift is less than $\pi/2$. The evolutions of the SNRs of both the sum and the difference of the input signals with the phase shift are shown in Fig. 4.2.

b) The impact of the signals amplitudes and Noise levels on the SNR of the sum

Now, we will consider the case of in-phase input signals with different amplitudes and noise levels. Calculated and evaluated SNRs of the sum of the in-phase input signals are listed in Table 4.2.

Parameters A, B, C & D	Calculated SNR_X	Calculated SNR_Y	Calculated SNR_{sum}	Evaluated SNR_{sum}
3, 4, 0.2, 0.2	20.5	23.0	24.9	24.9
2, 2, 0.1, 0.3	23.0	13.5	19.0	19.1
3, 6, 0.7, 0.2	9.6	26.5	18.8	18.9
6, 3, 0.7, 0.2	15.7	20.5	18.8	18.9

Table 4.2: Calculated and evaluated SNRs of the sum of the in-phase input signals.

As expected, SNR improvement is hardly achieved when the amplitudes of the input signals and the noise levels differ. In fact, most of the time, the SNR of the output will be less than the highest SNR of the input signals, rendering the arithmetic technique useless in this case.

4.3 Experimental Results

In the previous sections, we have introduced the mathematical representations of the correlation and the arithmetic signal processing techniques, followed by the validation of those techniques on ideal signals. The influence of the phase shift on the SNRs of the outputs of the arithmetic operation techniques has also been demonstrated. Therefore, in this section, we will apply the different signal processing techniques to the front PD, back PD and LV signals, which were

experimentally obtained at different injection currents and optical feedback levels to demonstrate the impact of the phase difference and the signal amplitudes, respectively.

The performed experiments can be divided into two main groups: i) in the first part, the measurements were performed at two laser injection currents for different attenuation levels in order to determine the influence of the optical feedback level on the SNRs of the outputs of the performed signal processing techniques; the laser injection currents were chosen to be one below and the other above the crossover current in order to account for the change of the phase of the front PD signal at the latter injection current, and ii) in the second part, the measurements were conducted at five different values of the laser injection current, with no neutral density filters added to the optical path, to further demonstrate the impact of the phase sign flip beyond the crossover current. In both parts, every measurement was performed five times to ensure repeatability.

4.3.1 Different feedback levels

As stated in the previous section, neutral density filters with different attenuation coefficients were introduced into the optical path in order to control the optical feedback level. The measurements for different feedback levels were performed at two different injection currents: one below and one above the crossover current, since the arithmetic addition and subtraction operations are phase-sensitive.

4.3.1.1 below the crossover current

The first experiment was performed at 6.5 mA, just slightly above threshold current. This injection current was chosen so that the front and the back PD signals are in-phase.

a) SNRs of OFI signals

Three neutral density filters with different attenuation coefficients were used in the experiments. Their round-trip attenuation coefficients were experimentally

measured at 1.31 µm and found to be 12 dB, 15 dB and 21 dB. A combination of the 12 dB and 21 dB was used during the experiments, which mean that we had five attenuation levels, including the case where no neutral density filters were present.

Fig. 4.3 shows the SNRs of the OFI signals measured at 6.5 mA for the different attenuation levels. As expected, we observe that the higher is the attenuation level, the weaker is the signal amplitude. At the highest attenuation level, both the LV and the front PD signals are lost due to the suppression by the high noise levels.

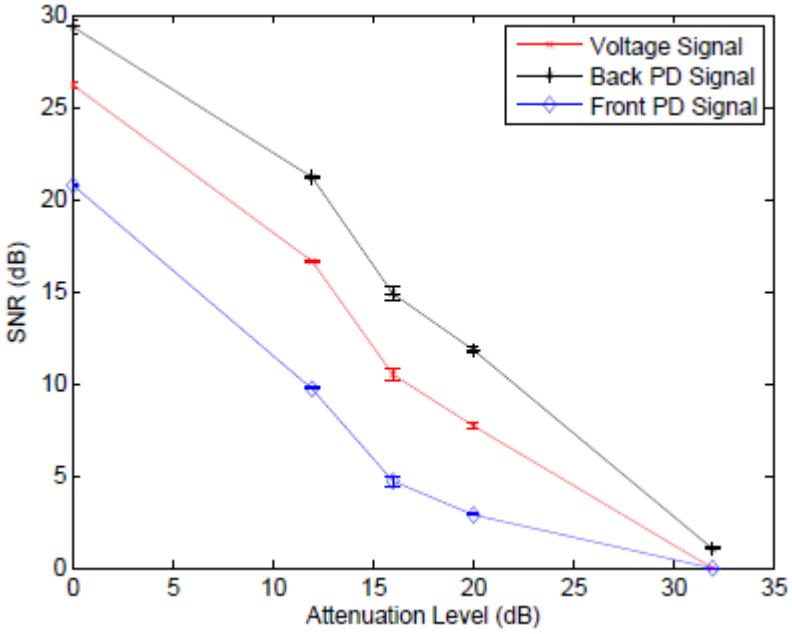

Fig. 4.3: SNRs of OFI signals obtained at 6.5 mA for different feedback levels (solid red: LV signal, solid black: back PD signal, and solid blue: front PD signal).

We will refer to these SNRs when we analyse the output SNRs of every signal processing technique applied to OFI signals. In other words, they are the reference based on which we decide if the performed signal processing technique improves the properties of the OFI signals or not.

b) Autocorrelation of OFI signals

As mentioned earlier, out of the three different OFI signals, LV and back PD signals are always out-of-phase. The front and back PD signals go from in-phase relationship to out-of-phase relationship beyond the crossover current. At crossover current, the front PD signal is reduced to a mere noise. Here, the

injection current is just slightly above threshold, and both PD signals are in-phase. The first signal processing technique applied here is autocorrelation.

Fig. 4.4 shows the SNRs of the output signals obtained from performing the autocorrelation technique on the LV and PD OFI signals measured at 6.5 mA as a function of the attenuation level. The variation of the attenuation levels allows us to compare the SNRs of the autocorrelation output signals as a function of optical feedback levels.

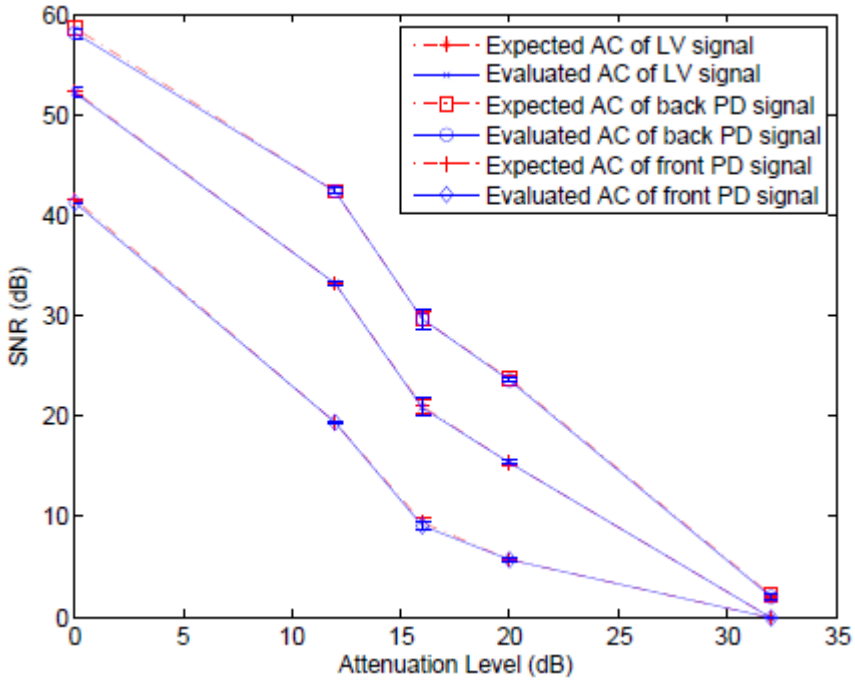

Fig. 4.4: SNRs of the output signals obtained from the autocorrelation of the OFI signals at 6.5 mA for different optical feedback levels (solid blue: obtained values, and dashed red: expected values).

The SNRs of the OFI signals shown in Fig. 4.3, in decibels, will be treated as a reference for those of the output signals. From the spectral properties of the autocorrelation function, when performing autocorrelation on a signal, we expect the SNR of the output signal to be, more or less, twice that of the input signal. OFI signals are accompanied with noise signals which, as explained in the theoretical background subsection, are independent on the noise-free OFI signals, and thus are reduced to zero. This independency can be confirmed through the comparison of the obtained and the expected SNRs.

Fig. 4.4 shows the SNRs of the output signals obtained through applying the autocorrelation technique to the OFI signals and the reference SNRs as a function of the attenuation level. In all OFI signals, the SNRs obtained from autocorrelation are almost twice those of the OFI signals, confirming the independency of the noise signals on the noise-free OFI signals. Moreover, it shows that the SNRs of OFI signals could be strongly improved by performing autocorrelation in the expense of higher memory capacity and longer processing time.

The autocorrelation is a powerful tool to enhance the SNR in general, making it easier to process OFI signals even when the corresponding SNR is quite low. However, this is achieved with the cost of a longer processing time and the inquiry of a higher memory capacity. Even higher SNRs can be obtained through constitutive application of autocorrelation, though processing time and memory capacity will grow exponentially.

c) Cross-correlation of OFI signals

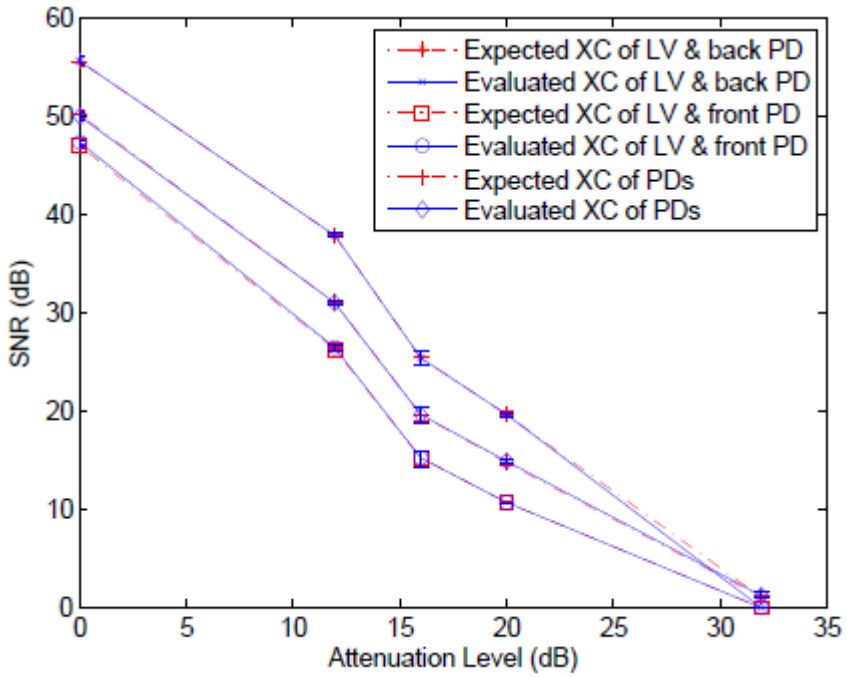

Fig. 4.5: SNRs of the cross-correlation of the OFI signal pairs obtained at 6.5 mA for different feedback levels (solid blue: obtained values, and dashed red: expected values).

The second signal processing technique applied is cross-correlation. Fig. 4.5 shows the SNRs of the output signals obtained from performing the cross-

correlation technique on either two of the OFI signals measured at 6.5 mA as a function of the attenuation level. As expected from cross-correlation, the SNR curves of the output signals exhibit a mixed features of the characteristics of the input OFI signals shown in Fig. 4.3.

Like in autocorrelation technique, when two independent noisy signals are cross-correlated, the SNR of the output signal will be the sum of SNRs of the input signals. Again, since the noise signals are independent on the noise-free OFI signals, we will consider the sums of the input OFI signals SNRs, from Fig. 4.3, as a reference. By comparing the obtained SNRs of the output signals to the reference SNRs, we can prove the noise signals independency.

Fig. 4.5 shows the SNRs of the output signals obtained from the cross-correlation of the OFI signals and the reference SNRs as a function of the attenuation level. Excluding the SNR of the output signal obtained from the cross-correlation of the LV and the back PD signals at the highest attenuation level, which is zero due to the attenuated amplitudes being insufficient for proper fitting, the SNRs obtained from cross-correlation of any two OFI signals are approximately equal to the sum of the SNRs of those OFI signals, ensuring the independency of the noise signals.

Actually, the cross-correlation signal processing technique is inferior to autocorrelation when it comes to the enhancement of SNR. For example, given two input signals with different SNRs, the SNR of the cross-correlation output would be less than twice the highest SNR of the two, which is equivalent to the autocorrelation of the signal with the highest SNR. Moreover, cross-correlation also comes with the expenses of higher capacity and longer processing times.

d) Addition and Subtraction of OFI signals

The third signal processing technique applied is the arithmetic addition and subtraction of OFI signals. The three different OFI signals have different noise sources. Here, we try investigating the possibility of reducing the noise accompanying an OFI signal by adding it to or subtracting it from another OFI signal acquired from a different source. Applying addition or subtraction depends mainly on the phase relationship between the two OFI signals. In order to obtain the highest SNR, addition is implemented when the two OFI signals are in-phase while subtraction is the one implemented when they are out-of-phase.

As demonstrated earlier, if the input signals have the same amplitudes and noise levels, then the SNR of the output signal would be exactly 3 dB higher than those of the input signals. However, the obtained OFI signals have different noise levels and amplitudes. Therefore, depending on the amplitudes and the noise levels of the input signals, we may end up with a SNR that is even lower than the highest SNR of the input signals.

Fig. 4.6 shows the SNRs of the output signals obtained from performing either the arithmetic addition or subtraction techniques on either two of the OFI signals measured at 6.5 mA as a function of the attenuation level. The front and back PD signals were added as they are in-phase while the LV signal was subtracted from both PD signals since it is out-of-phase with either signal.

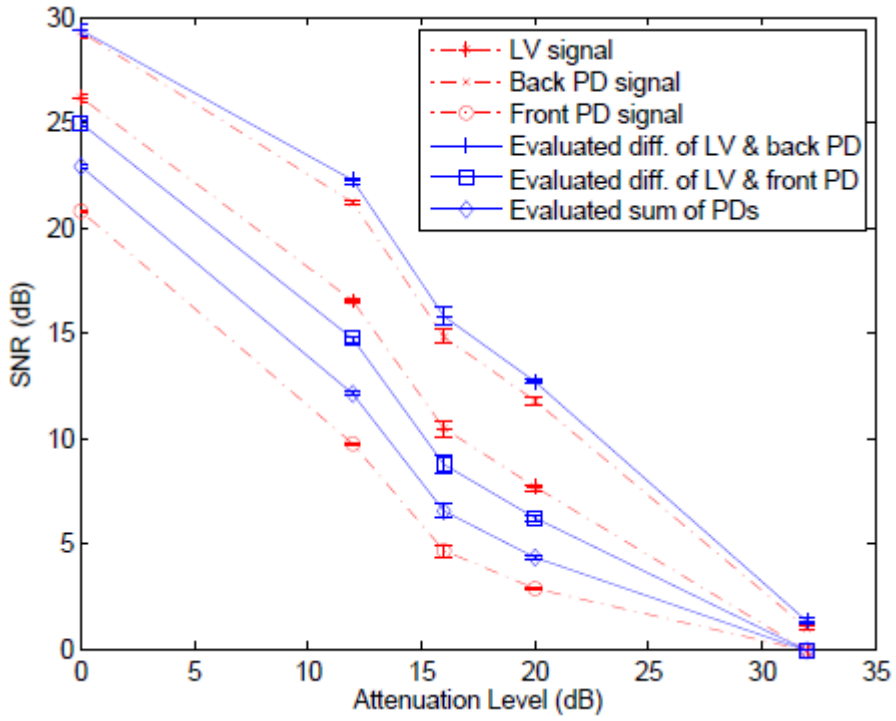

Fig. 4.6: SNRs of either the addition or the subtraction of the OFI signal pairs obtained at 6.5 mA for different attenuation levels (solid blue: obtained values, and dashed red: SNRs of the OFI signals).

Unlike in the autocorrelation and the cross-correlation techniques, since the spectral properties of the addition and subtraction techniques depend on both the amplitudes and the noise levels of the input signals rather than their SNRs, we don't have a reference to compare the SNR of the output signal to. The only fact we have is that the output SNR won't exceed a 3 dB difference from the highest

SNR of the two input signals, which we may consider as kind of a reference. Actually, since the arithmetic operation was chosen to be constructive, the SNR of the output signal would be at least higher than the lower SNR of the two input signals.

Fig. 4.6 shows the SNRs of the output signals obtained from the subtraction of the LV and the back PD signals as well as the SNRs of those OFI signals as a function of the attenuation level. Since both OFI signals are out-of-phase below the crossover current, the signals were subtracted in order to obtain an output signal with the highest SNR. The SNR of the output signal is almost 1 dB higher than that of the back PD signal or almost 2 dB less than the best SNR difference that could be obtained. This is due to the difference in both of noise levels and signals amplitudes.

Also, the SNRs of the output signals obtained from the subtraction of the LV and the front PD signals as well as the SNRs of those OFI signals are shown for different attenuation levels. Like before, both OFI signals are out-of-phase, hence the subtraction operation was performed to obtain an output signal with the maximum SNR. However, the SNR of the output signal almost 1 dB less than the SNR of the LV signal. This is due to the huge difference is noise levels of both signals.

The SNRs of the output signals obtained from the addition of both PD signals as well as the SNRs of those OFI signals are shown as a function of the attenuation level. Both signals are in-phase, hence the addition of the signals. The wide gap in noise levels and the amplitudes of the OFI signals as well results in the SNR of the output signal being way lower than that of the back PD signal.

Unlike cross-correlation and autocorrelation, the logarithmic differences in noise levels and signals amplitudes of the OFI signals, rather than the SNRs, are the parameters that determine if the SNR of the output signal is 3 dB higher or less than the reference SNR. Since the noise levels and the amplitudes of the OFI signals differ considerably with the system parameters and the experimental conditions, it is more convenient to apply either autocorrelation or cross-correlation techniques on the OFI signals rather than the arithmetic operations. Even in the best case scenario, when the noise levels and the signals amplitudes

are almost equal, the 3 dB improvement in SNR is not that high compared to the other two signal processing techniques. Moreover, possible averaging of noise from two different sources wouldn't be effective unless noise levels are comparable to each other.

4.3.1.2 above the crossover current

The second part of the first experiment was performed at 20 mA, an injection current that is slightly more than twice the crossover current. This injection current was chosen so that the SNRs of both PD signals are higher than that of the LV signal. Another reason for choosing this value is that both PD signals are out-of-phase. Therefore, we can compare the phase effect on the outputs of the signal processing techniques with those introduced in the previous subsection. Before proceeding with the signal processing techniques, we should restate that the PD signals are also out-of-phase.

a) SNRs of OFI signals

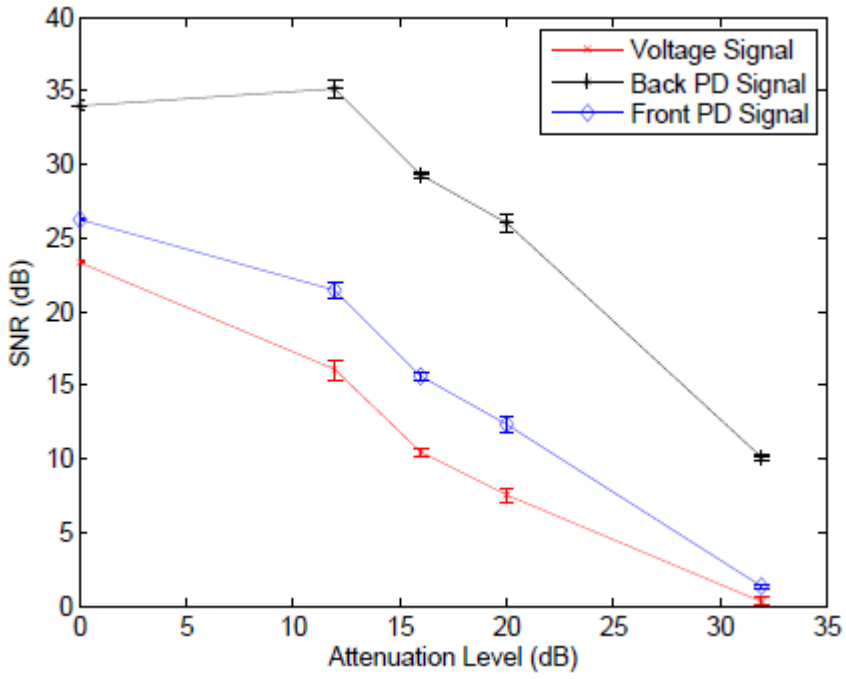

Fig. 4.7: SNRs of OFI signals obtained at 20 mA for different feedback levels (solid red: LV signal, solid black: back PD signal, and solid blue: front PD signal).

Fig. 4.7 shows the SNRs of the OFI signals measured at 20 mA as function of the attenuation levels. Except for the SNR of the back PD signal when there is no attenuation, the SNRs of the OFI signals decrease with the increase of the attenuation level. Like before, these SNRs are considered as references based on which we decide whether a signal processing technique improves the properties of an OFI signal or not.

The SNRs of the OFI signals shown in Fig. 4.7 will be treated as references for those of the output signals. Twice the SNR of an OFI signal will be considered as the reference to which we compare the SNR of the output signal obtained from the autocorrelation of the signal. By comparing both values we can examine the efficiency of the autocorrelation function as a signal processing technique in improving the SNRs of the OFI signals.

b) Autocorrelation of OFI signals

Fig. 4.8 shows the SNRs of the output signals obtained from the autocorrelation of the OFI signals measured at 20 mA as a function of the attenuation level. Since the curves here are based on the ones shown in Fig. 4.7, it comes as no surprise that they exhibit similar profiles.

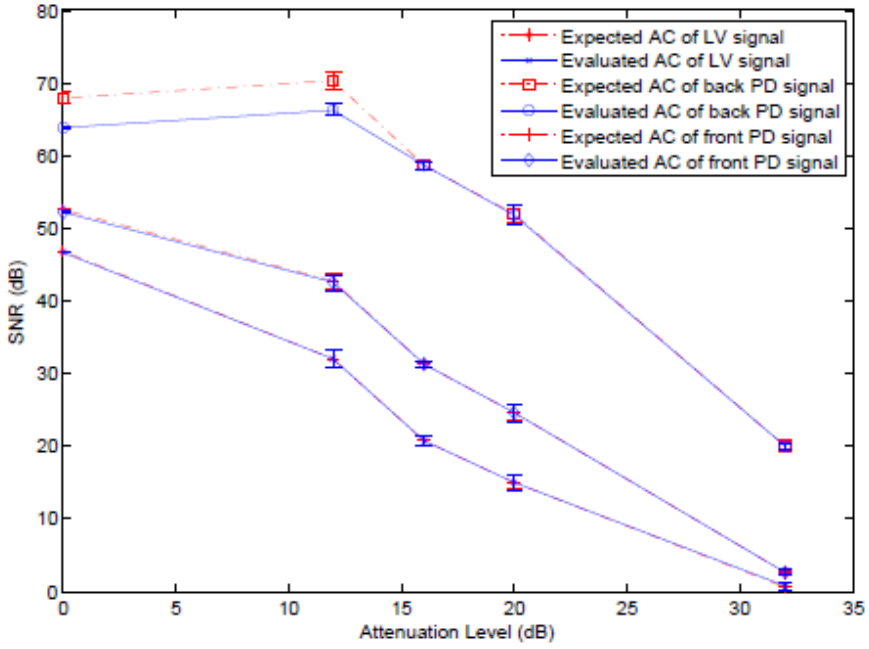

Fig. 4.8: SNRs of the output signals obtained from the autocorrelation of the OFI signals at 20 mA for different optical feedback levels (blue: obtained, and red: expected values).

Except for the SNRs of the output signals obtained from the autocorrelation of the back PD signals at no attenuation and at 12 dB attenuation levels where the output SNRs are almost 4.5 dB lower than those of the references, the corresponding obtained and reference SNRs are almost equal. This is expected since the correlation functions are not affected by the phase-shift. The observed 4 to 5 dB difference in SNRs is mainly due to the windowing effect.

c) Cross-correlation of OFI signals

Fig. 4.9 shows the SNRs of the output signals obtained from the cross-correlation of either two of the OFI signals measured at 20 mA as a function of the attenuation levels. As expected, the SNR curves of the output signals exhibit mixed features of the input OFI signals characteristics regarding the evolution of SNRs with the attenuation levels.

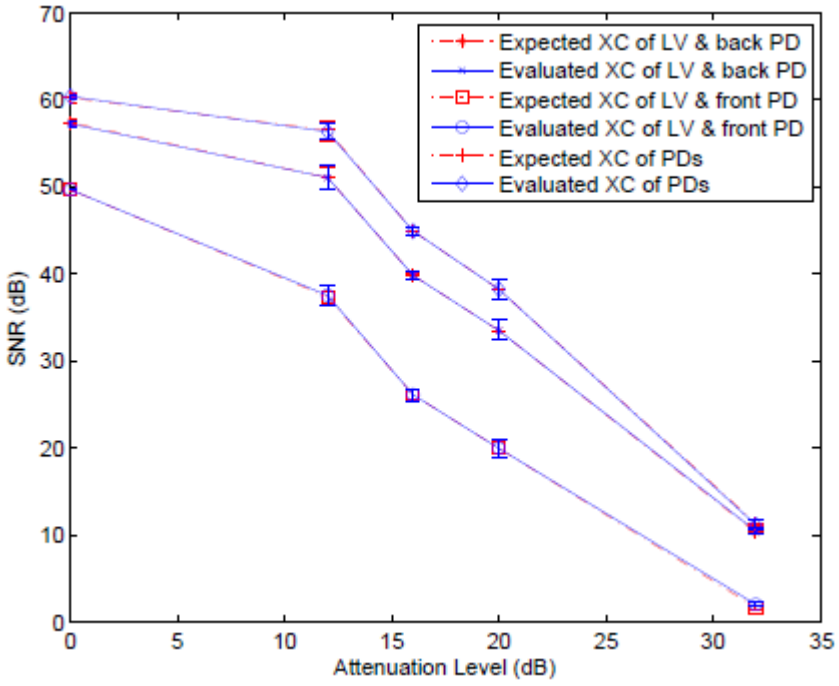

Fig. 4.9: SNRs of the cross-correlation of the OFI signal pairs obtained at 20 mA for different feedback levels (solid blue: obtained values, and dashed red: expected values).

In the previous subsection, we have demonstrated that the obtained SNR equals the sum of the input signals SNRs, which proves the independency of the noise signals on the noise-free OFI signals. Here we will apply the same technique again to prove that the cross-correlation function is insensitive to the phase difference between input signals.

From Fig. 4.9, it is clear that the SNRs of the output signals obtained from the cross-correlation of the OFI signals and the reference SNRs are equal regardless of the attenuation level. Again, both correlation functions are insensitive to phase difference between the input signals. The autocorrelation technique is superior to the cross-correlation technique in terms of improving the SNR of the OFI signals. This improvement requires a trade off with the memory capacity and the processing time.

d) Addition and Subtraction of OFI signals

Before presenting the arithmetic addition and subtraction signal processing techniques, we should re-state the phase relationship between the OFI signals at 20 mA, which is above the crossover current. The LV signal is in-phase with the front PD signal while it is out-of-phase with the back PD signal. Hence, the LV and the front PD signals are added together while the PD signals are subtracted one from the other in order to ensure acquiring the highest SNR that could possibly be obtained through applying either arithmetic operation. However, we should keep in mind that merely 3 dB is the maximum boast in SNR that could be achieved here.

Fig. 4.10 shows the SNRs of the output signals, obtained from applying either arithmetic operation on the OFI signal pairs measured at 20 mA, as a function of the attenuation level. We compare the SNR of the output signal to that of the reference, which is the input signal with the highest SNR, to determine whether this signal processing technique does or does not improve the characteristics of the input signals.

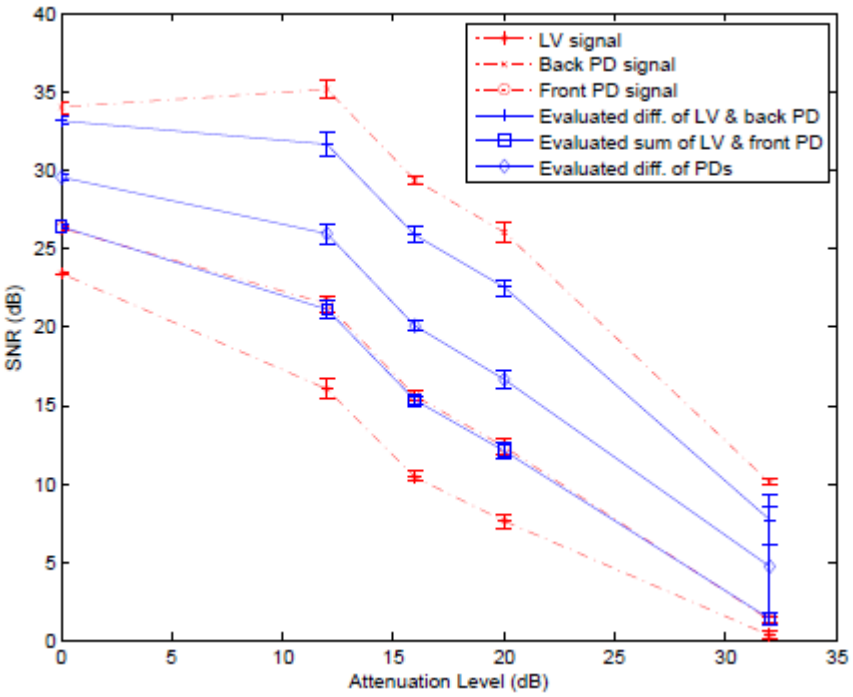

Fig. 4.10: SNRs of either the addition or the subtraction of the OFI signal pairs obtained at 20 mA for different attenuation levels (solid blue: obtained values, and dashed red: SNRs of the OFI signals).

From Fig. 4.10, it is clear that the SNR of the output signal would be at least higher than the lower SNR of the two input signals, as the applied arithmetic operation is always constructive.

The arithmetic operations are inferior to autocorrelation and cross-correlation techniques when it comes to the improvement of SNRs. In correlation techniques, the SNR of the output signal is a function of those of the input signals. Hence, input signals with higher SNRs yield to output signals with higher SNRs. However, in arithmetic operations it all depends on the amplitudes and the noise levels of the input signals rather than their SNRs. Therefore, the improvement of SNR won't exceed 3 dB in the best case scenario. To make it worse, when the gaps in amplitudes and noise levels of the input signal are considerable, the SNR of the output signal may even be less than that of either input signal.

4.3.2 Different injection currents

So far, we have investigated the effect of the attenuation level, and hence the strength of the feedback, on the outputs of different signal processing techniques applied to the OFI signals so as to improve their properties. Moreover, OFI signals were measured at two different injection currents, below and above the crossover current, in order to determine the influence of the phase change on the signal processing outputs.

Here, we investigate the influence of the change in injection current while the attenuation level is maintained constant. The neutral density filters were removed, and the OFI signals were measured at five different bias currents that lie between 6.5 mA and 20 mA to account for the phase inversion of the front PD signal beyond the crossover current.

a) SNRs of OFI signals

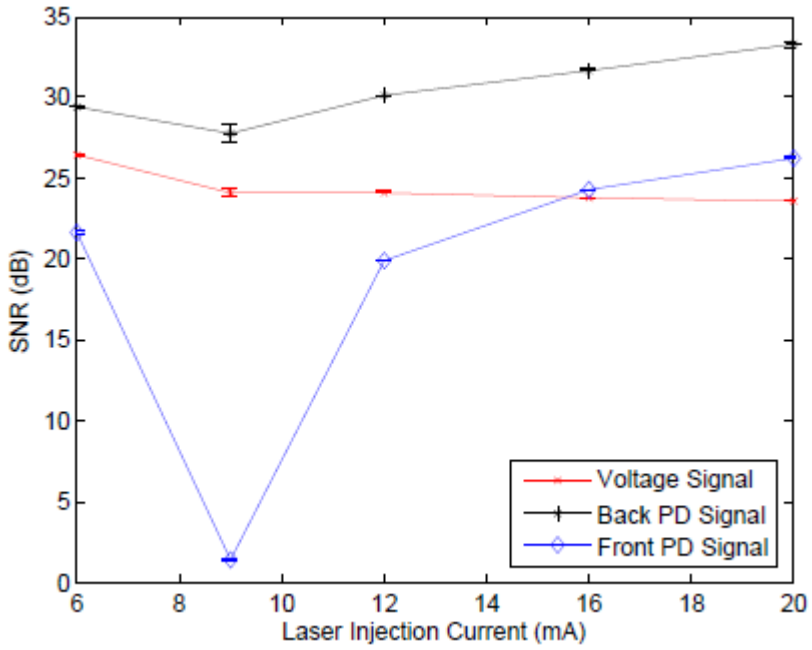

Fig. 4.11: SNRs of OFI signals as a function of laser injection current (solid red: LV signal, solid black: back PD signal, and solid blue: front PD signal).

Fig. 4.11 shows the SNRs of the OFI signals as a function injection current. Except for a minor difference, the evolutions of the SNRs with injection current coincide with those obtained for the amplitudes of OFI signals back in chapter 3. As we can see, the SNR of the LV signal decreases while that of the back PD

signal increases with the increase of injection current. We also observe the sharp drop in the SNR of the front PD signal from above 20 dB to below 2 dB followed by a sharp rise to above 20 dB at 12 mA, indicating that the crossover current is somewhere around 9 mA. As before, the SNRs shown here will be considered as references for the evaluation of the signal processing techniques capability to enhance the SNRs of the OFI signals.

b) Autocorrelation of OFI signals

Fig. 4.12 shows the SNRs of the output signals, obtained from the autocorrelation of the OFI signals, as a function laser injection current. The curves are based on the ones shown in Fig. 4.11, hence the similar profiles. Moreover, twice the SNRs of the OFI signals shown here will be considered the reference SNRs to which we compare those of the autocorrelation outputs.

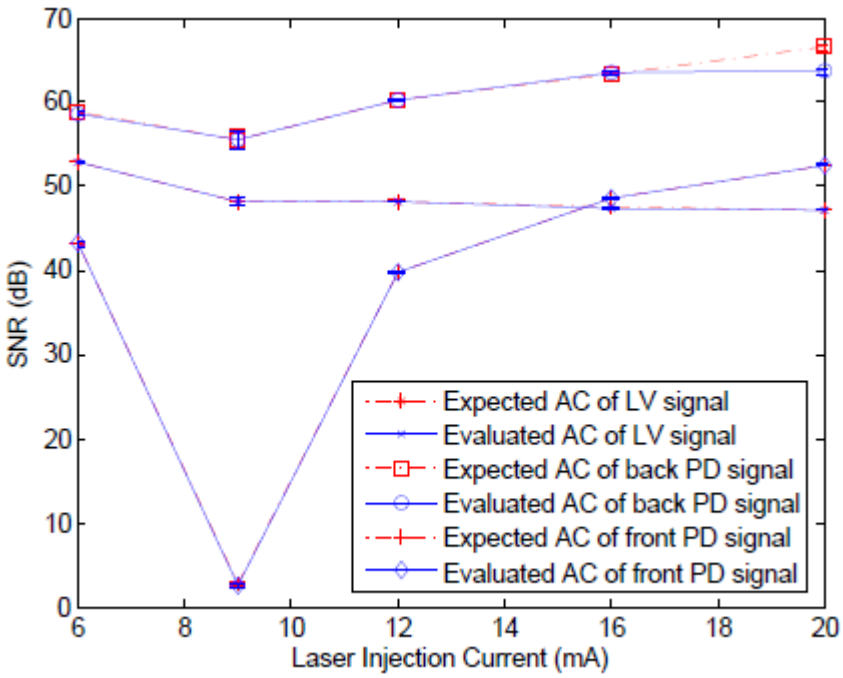

Fig. 4.12: SNRs of the output signals obtained from the autocorrelation of the OFI signals measured at different laser injection currents (solid blue: obtained values, and dashed red: expected values).

Except for the SNR obtained through the autocorrelation of the LV signal at 20 mA where it is approximately 2.5 dB less than expected, the difference between the obtained and the reference SNRs are almost zero for all injection currents.

Again, the observed difference is a result of the windowing used when performing the FFT to obtain the frequency response.

The autocorrelation enhances the SNRs of the OFI signals, which allows processing OFI signals even when their SNRs are quite low. However, the need of longer processing time and higher memory capacity are the drawbacks of this achievement. Successive application of autocorrelation yields even way higher SNRs, though the processing time and memory capacity inquiries will grow exponentially.

c) Cross-correlation of OFI signals

Fig. 4.13 shows the SNRs of the cross-correlation outputs obtained from either two of the OFI signals as a function of laser injection current. The observed sharp decrease in the blue and the black curves around 9 mA is influenced by the sharp decrease in the SNR of the front PD signal around the crossover current.

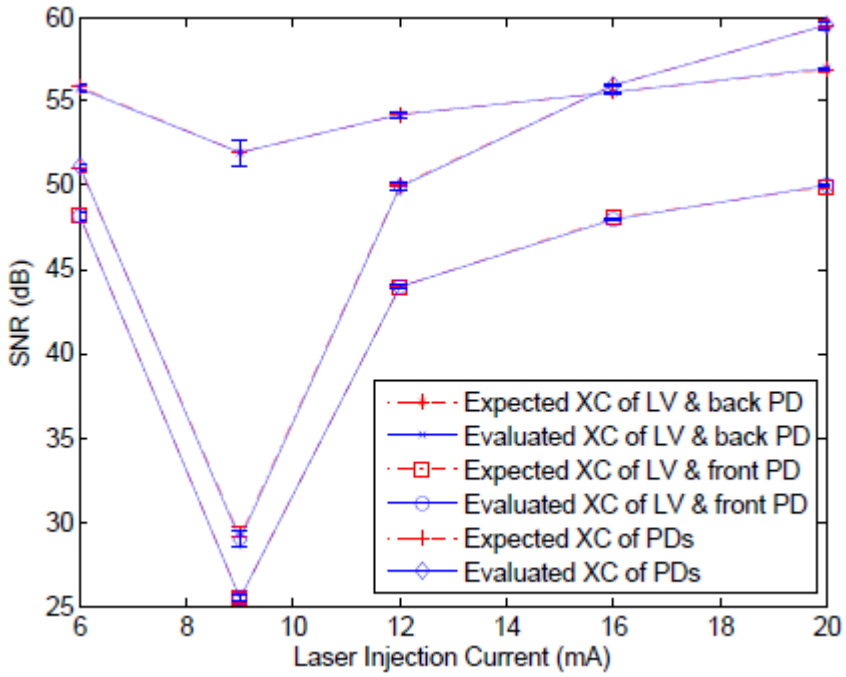

Fig. 4.13: SNRs of the cross-correlation of the OFI signal pairs as a function of laser injection current (solid blue: obtained values, and dashed red: expected values).

There is almost no difference between the obtained and the reference SNRs. Furthermore, the cross-correlation is insensitive to the phase inversion of the front PD signal.

Other than the sharp decrease in SNRs of the cross-correlation outputs influenced by the temporal front PD signal drop, a slight decrease in SNR is observed in the red curve. This may seem odd as it results from the slight drop in the SNR of the back PD signal which should have monotonically increasing amplitude with injection current as demonstrated in the previous chapter. Actually this is still the case, and the momentary drop in SNR is due to the rapid growth of the noise level at low injection current.

Again, the SNR improvement with cross-correlation is still inferior to that of the back PD signal autocorrelation. Furthermore, both correlation techniques are insensitive to any phase shift in the OFI signals.

d) Addition and Subtraction of OFI signals

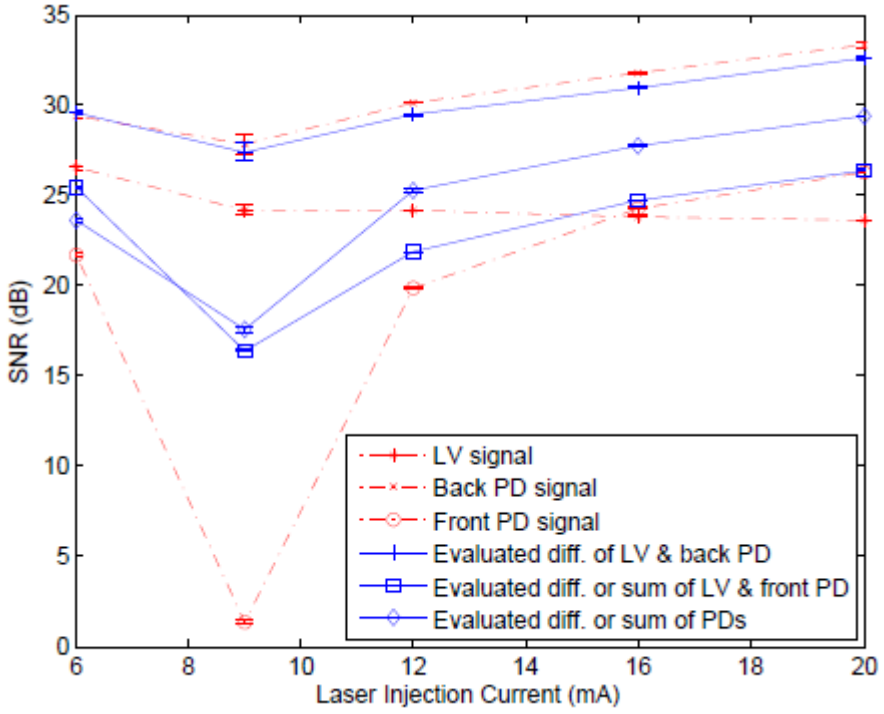

Fig. 4.14: SNRs of either the addition or the subtraction of the OFI signal pairs obtained at different laser injection currents (solid blue: obtained values, and dashed red: SNRs of the measured OFI signals).

The front PD signal is phase-shifted by π somewhere between 9 mA and 12 mA. Hence, PD signals are in-phase at 6.5 mA and 9 mA, while they are out-of-phase for higher injection currents. Furthermore, the LV and the back PD signals are always out-of-phase. Due to this strange behaviour of phase change, we

should be careful when applying either addition or subtraction arithmetic operations on OFI signals.

Fig. 4.14 shows the output SNRs obtained from either addition or subtraction of the OFI signal pairs as a function of the laser injection current. PD signals were added together at 6.5 mA and 9 mA whereas they were subtracted one from the other at higher laser injection currents. Due to the great difference between the signals amplitudes and noise levels, the SNRs of the outputs are less than those of the input signals.

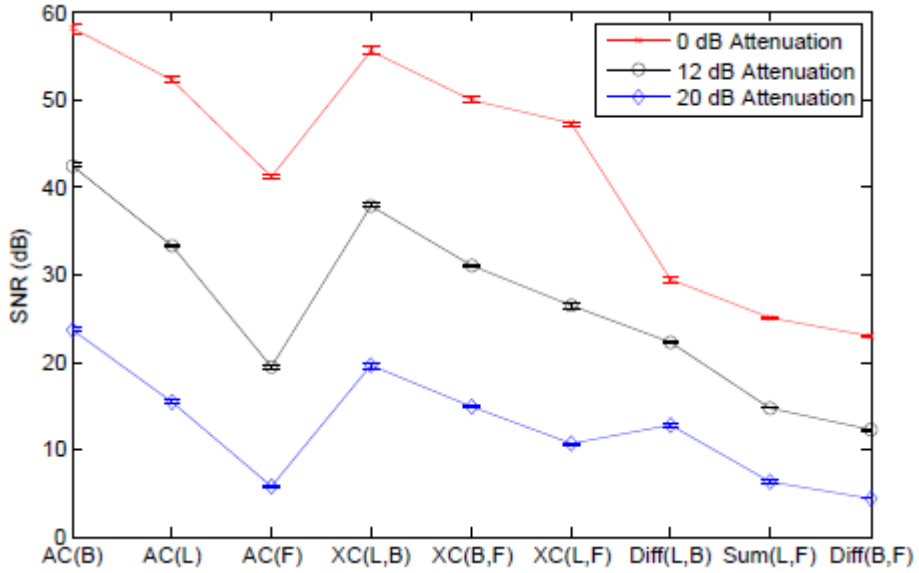

Fig. 4.15: SNRs of the outputs of the different signal processing techniques (AC: autocorrelation, XC: cross-correlation, sum and difference) of the different OFI input signals (L: LV signal, B: back PD signal, and F: front PD signal) acquired at 6.5 mA for different attenuation levels (red solid: 0 dB, black solid: 12 dB, and blue solid: 20 dB).

Fig. 4.15 shows the SNRs of the outputs of the different signal processing techniques performed on the OFI input signals at different attenuation levels for a laser injection current of 6.5 mA. As demonstrated earlier, out of the three techniques, autocorrelation yields the highest improvement in SNR (almost

doubles the SNR in decibels of the input signal), whereas the arithmetic operation hardly yields an output with a SNR that is higher than those of the input signals.

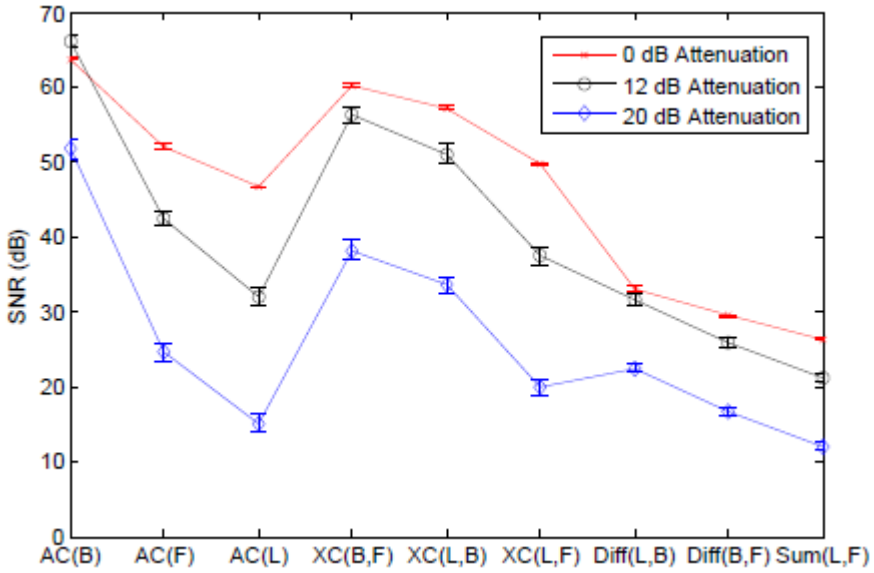

Fig. 4.16: SNRs of the outputs of the different signal processing techniques (AC: autocorrelation, XC: cross-correlation, sum and difference) of the different OFI input signals (L: LV signal, B: back PD signal, and F: front PD signal) acquired at 20 mA for different attenuation levels (red solid: 0 dB, black solid: 12 dB, and blue solid: 20 dB).

Similarly, Fig. 4.16 shows the SNRs of the outputs obtained from the OFI signals which were measured at different attenuation levels for a laser injection current of 20 mA. The noticeable difference in the attenuation levels obtained here, though the neutral density filters are still the same, is due to the presence of high order harmonics when either no attenuation or low attenuation is present.

Comparison of the SNRs of the cross-correlation outputs and the addition/or subtraction outputs are shown in Fig. 4.17 (for the LV signals and the back PD signals) and Fig. 4.18 (for the back and front PD signals). Here, the superiority of the cross-correlation techniques over the addition and the subtraction is clearly demonstrated.

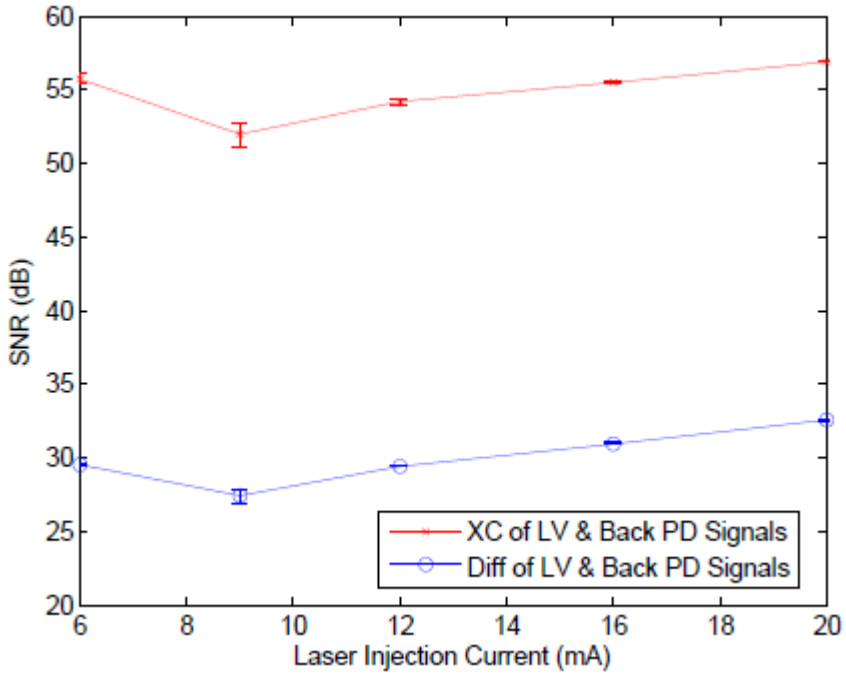

Fig. 4.17: Comparison of the SNRs of both the cross-correlation and the difference of the LV and back PD signals as a function of the laser injection current (solid red: cross-correlation and solid blue: difference).

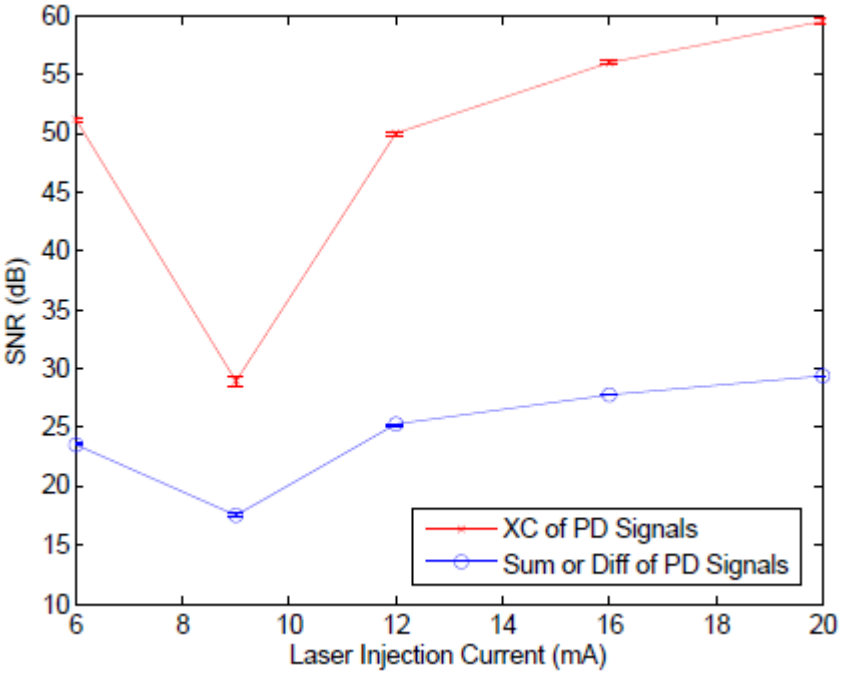

Fig. 4.18: Comparison of the SNRs of both the cross-correlation and the difference of the front and back PD signals as a function of the laser injection current (solid red: cross-correlation and solid blue: difference).

In general, the correlation functions improve the SNRs of OFI signals way higher than those of the addition and subtraction of the OFI signals. The improvement of SNRs in the arithmetic operations doesn't exceed 3 dB in the best case scenario since it solely depends on the signals amplitudes and the noise levels rather than their SNRs. Moreover, the cross-correlation technique is inferior to the autocorrelation technique as the SNR obtained through cross-correlation of two signals is always lower than twice the highest SNR of the input signals. The improvement of SNRs is obtained with the trade off a higher memory capacity and a longer processing time.

General Conclusion

The work presented in this thesis mainly focuses on the derivation and the proposal of a simple mathematical model, applicable to single-mode laser diodes, which provides compact analytical expressions to quantitatively describe the dependence of the OFI signal strength on the system parameters, and particularly the laser injection current. The model accounts for the three different OFI signal sources: the variations in the laser junction voltage (the LV signal) and the power fluctuations in the output optical power emitted from either the rear facet of the laser diode using the commonly built-in monitoring photodiode (the rear PD signal) or the front facet using an external photodiode (the front PD signal). The presented work has been limited to single-mode (transverse and longitudinal) laser diodes due to the device-dependent nature of the optical feedback sensing scheme. Only experimental results have been performed on multimode devices in order to evaluate the model's validity to multimode devices.

The derived model proposed an explanation to the experimentally observed divergent evolution of the PD and the LV signals with laser injection current as the model predicted that the photodiode and voltage signal strengths depend differently on injection current and temperature. In fact, the model showed that both the photodiode and the voltage signal strengths are dependent on the laser slope efficiency, which itself is a function of the injection current and the temperature. Moreover, analysing both the amplitudes and the phase difference between the front and the back PD signals showed that the front PD signal encounters a 180° shift at some point along the laser injection current range, which we defined as the crossover current.

In order to evaluate the analytical model, a set of experiments were performed on for two different types of laser diodes: a distributed feedback (DFB) laser and a vertical-cavity surface-emitting laser (VCSEL). Furthermore, the model validity has been experimentally investigated in the case of multimode laser diodes: a transverse multimode VCSEL and a longitudinal multimode Fabry-Pérot type laser diode. The experiments were performed over a large range of laser injection currents and operating temperatures in order to validate the major influence of these parameters on the OFI signals amplitudes that are predicted by the model.

From both the analytical model and experiments, PD and LV signals behave differently with the laser injection current. The LV signal is greatest just above the laser threshold and subsequently decreases with increasing laser injection current, while the back PD signal strength is linearly increasing with the laser injection current. The front PD signal encounters a gradual increment followed by a gradual decrement until the signal completely vanishes at the crossover current. With further increment of the laser injection current, the front PD signal starts increasing almost linearly with the injection current, similarly to the back PD signal.

This interesting phenomenon can be accounted for by including the laser injection current dependence of slope efficiency. Moreover, the model offers a clear explanation of the experimentally observed monotonic decrease in the back PD signal strength with temperature, as the slope efficiency decreases with the temperature increase while the threshold current increases. Meanwhile, the LV signal strength is proportional to the temperature and the slope efficiency, and the two opposing effects lead to a less pronounced change of the signal strength over the full temperature range with a plateau at temperatures around the middle of the temperature range. The model proposed in this thesis provides insight into the selection of injection current levels that maximize the signal strength, and hence sensor sensitivity, for back PD, front PD and LV acquisition schemes. The biasing strategy is radically different for those schemes: for LV signals the optimal injection current is close to threshold, while front and back PD schemes offer greater sensitivity at much higher bias currents.

Another interesting prediction of the model that has been validated experimentally is that, the back and the front PD signals were found to be in-phase for injection currents lower than the crossover current, and out-of-phase for higher injection currents. Moreover, by performing the measurements with the same system setup for different attenuation levels, we experimentally proved that the value of the crossover current is independent on the optical feedback level, and thus the effective reflectivity of the remote target. The model also explains the inability to detect the front PD signals at the crossover current, and predicts the permanent out-of-phase relationship between the back PD and the LV signals.

Based on the hypothesis that acquisition of the same informative signal through two different sources should be emphasizing the signal while suppressing the noise, different signal processing techniques have been investigated to either two of the different OFI signals (the front PD signal, the rear PD signal and the LV signal) in search for any noticeable improvements in the characteristics of the signals, and in particular the signal-to-noise ratio SNR. The signal processing techniques were autocorrelation, cross-correlation, and the simple arithmetic addition/subtraction operations.

It was proven theoretically and experimentally that improvement in SNRs of OFI signals achieved through the application of the correlation functions far exceeds the one achieved through the application of the arithmetic operations. The improvement of SNRs in the arithmetic operations doesn't exceed 3 dB in the best case scenario since it strongly depends on the signals amplitudes and the noise levels. Moreover, the phase difference between the input OFI signals has a great influence on the outputs of the arithmetic operations, as it has been theoretically and experimentally demonstrated.

As for the correlation functions, the autocorrelation technique is superior in improving the SNR to the cross-correlation technique, since the SNR obtained through cross-correlation of two signals is always lower than twice the highest SNR of the input signals in the logarithmic scale. However, this improvement in SNRs comes with a trade-off with a higher memory capacity and a longer processing time.

The model could be extended by further including the effects of noise, such as taking into account the noise of the laser and the photodetector evolutions with the system parameters: injection current or temperature. Also, further work shall consider more complex lasing regimes with multiple transverse or longitudinal mode operation starting from the generalized Lang and Kobayashi model instead of the standard model.

Bibliography

[1] I. H. Maiman, "Stimulated Optical Radiation in Ruby," *Nature*, vol. 187, pp. 493-494, 1960.

[2] R. J. Collins, D. F. Nelson, A. L. Schawlow, W. Bond, C. G. B. Garrett, and W. Kaiser, "Coherence, Narrowing, Directionality and Relaxation Oscillations

in the Light Emission from Ruby," *Phys. Rev. Lett.*, vol. 5, pp. 303-305, 1960. [3] D. A. Kleinman and P. P. Kisliuk, "Discrimination against Unwanted Orders in the Fabry-Perot Resonator," *Bell Sys. Tech. J.*, vol. 41, pp. 453-462, 1962.

[4] H. Kogelnik and C. K. N. Patel, "Mode Suppression and Single Frequency Operation in Gaseous Optical Masers," *Proc. IRE*, vol. 50, pp. 2365-2366, 1962.

[5] S. A. Collins and G. R. White, "Interferometer Laser Mode Selector," *Appl. Opt.*, vol. 2, pp. 448-449, 1963.

[6] M. Birnbaum and T. L. Stocker, "Mode Selection Properties of Segmented Rod Lasers," *J. Appl. Phys.*, vol. 34, pp. 3414-3415, 1963.

[7] S. Saito and T. Kimura, "Low Frequency Oscillation in a He-Ne Gaseous Optical Maser with Three Reflecting Mirrors," *Jpn. J. Appl. Phys.*, vol. 2, pp. 808-809, 1963.

[8] A. I. Carswell and A. L. Waksberg, "Off-Axis Feedback Modes in a Three-Mirror Laser System," *Can. J. Phys.*, vol. 42, pp. 1829-1834, 1964.

[9] L. C. Foster, M. D. Ewy, and C. B. Crumly, "Laser Mode Locking by External Doppler Cell," *Appl. Phys. Lett.*, vol. 6, pp. 6-8, 1965.

[10] L. Beiser, "Mode Formation and Selection in Modified Confocal Resonator," *Appl. Phys. Lett.*, vol. 13, pp. 87-88, 1968.

[11] A. L. Waksberg, "Stabilization of a CO2 Laser Using a Three-Mirror Laser System," *IEEE J. Quantum Electron.*, vol. QE-4, pp. 532-533, 1968.

[12] P. G. R. King and G. J. Steward, "Metrology with an Optical Maser," *New Sci.*, vol. 17, pp. 180, 1963.

[13] D. M. Clunie and N. H. Rock, "The Laser Feedback Interferometer," *J. Sci. Instrum.*, vol. 41, pp. 489-492, 1964.[14] D. E. T. F. Ashby and D. F. Jephcott, "Measurement of Plasma Density Using Gas Laser as Infrared Interferometer," *Appl. Phys. Lett.*, vol. 3, pp. 13-16, 1963.

[15] J. B. Gerardo and J. T. Verdeyen, "Plasma Refractive Index by a Laser Phase Measurement," *Appl. Phys. Lett.*, vol. 3, pp. 121-123, 1963.

[16] J. B. Gerardo and J. T. Verdeyen, "The Laser Interferometer: Application to Plasma Diagnostics," *Proc. IEEE*, vol. 52, pp. 690-697, 1964.

[17] J. B. Gerardo and J. T. Verdeyen, "Correlated Interferometric Measurements of Plasma Electron Densities at Optical and Microwave Frequencies," *Appl. Phys. Lett.*, vol. 6, pp. 185-187, 1965.

[18] E. B. Hooper, Jr. and G. Bekefi, "Laser Interferometer for Repetitively Pulsed Plasmas," *J. Appl. Phys.*, vol. 37, pp. 4083-4094, 1966.

[19] I. C. Potter, "Frequency Response of the 6328-A Helium-Neon Laser Interferometer," *J. Appl. Phys.*, vol. 40, pp. 4770-4776, 1969.

[20] S. J. Fielding, "A Laser Interferometer with Harmonically Matched Cavities," *J. Phys. E*, vol. 5, pp. 920-922, 1972.

[21] C. B. Wheeler and S. J. Fielding, "Interferometry Using a Laser as Radiation Source, Amplifier and Detector," *J. Phys. E*, vol. 5, pp. 101-103, 1972.

[22] R. F. Gribble, J. P. Craig, and A. A. Dougal, "Spatial Density Measurements in Fast Thetapinch Plasma by Laser Excitation of Coupled Infrared Resonators," *Appl. Phys. Lett.*, vol. 5, pp. 60-62, 1964.

[23] D. E. T. F. Ashby, D. F. Jephcott, A. Malein, and F. A. Raynor, "Performance of the He-Ne Gas Laser as an Interferometer for Measuring Plasma Density," *J. Appl. Phys.*, vol. 36, pp. 29-34, 1965.

[24] D. A. Baker, J. E. Hammel, and F. C. Jahoda, "Extension of Plasma Interferometry Technique with a He-Ne Laser," *Rev. Sci. Instrum.*, vol. 36, pp. 395-396, 1965.

[25] J. B. Gerardo, J. T. Verdeyen, and M. A. Gusinow, "High-Frequency Laser Interferometry in Plasma Diagnostics," *J. Appl. Phys.*, vol. 36, pp. 2146-2150, 1965.

[26] E. B. Hooper, Jr. and G. Bekefi, "A Laser Interferometer for Repetitively Pulsed Plasmas," *Appl. Phys. Lett.*, vol. 7, pp. 133-135, 1965.

[27] W. A. Kricker and W. I. B. Smith, "A Moving Mirror Laser Interferometer for Plasma Diagnostics," *Phys. Lett.*, vol. 14, pp. 102-103, 1965.

[28] J. M. P. Quinn, "Gas-Laser Determination of the Electron Density in the Afterglow of a Hydrogen Discharge," *J. Nuclear Energy Part C*, vol. 7, pp. 113-122, 1965.

[29] A. C. C. Warnock, W. M. Deuchars, J. Irving, and D. E. Kidd, "Gas Laser Measurements of the Electron Density of a Plasma Produced by a Very Fast Theta-Pinch Preheater," *Appl. Phys. Lett.*, vol. 7, pp. 29-32, 1965.

[30] H. Z. Cummins, N. Knable, and Y. Yeh, "Observation of Diffusion Broadening of Rayleigh Scattered Light," *Phys. Rev. Lett.*, vol. 12, pp. 150-153, 1964.

[31] Y. Yeh and H. Z. Cummins, "Localized Fluid Flow Measurements with He-Ne Laser Spectrometer," *Appl. Phys. Lett.*, vol. 4, pp. 176-178, 1964.

[32] M. J. Rudd, "Laser Doppler Velocimeter Employing Laser as Mixer-Oscillator," *J. Phys. E*, vol. 1, pp. 723-726, 1968.

[33] R. N. Hall, G. E. Fenner, J. D. Kingsley, T. J. Soltys, and R. O. Carlson, "Coherent Light Emission from GaAs Junctions," *Phys. Rev. Lett.*, vol. 9, pp. 366-368, 1962.

[34] M. I. Nathan, W. P. Dumke, G. Burns, F. H. Dill, Jr., and G. Lasher, "Stimulated Emission of Radiation from GaAs P-N Junctions," *Appl. Phys. Lett.*, vol. 1, pp. 62-64, 1962.

[35] T. M. Quist, R. H. Rediker, R. J. Keyes, W. E. Krag, B. Lax, A. L. McWhorter, and H. J. Zeigler, "Semiconductor Maser of GaAs," *Appl. Phys. Lett.*, vol. 1, pp. 91-92, 1962.

[36] N. Holonyak, Jr. and S. F. Bevacqua, "Coherent (Visible) Light Emission from Ga (As1-X Px) Junctions," *Appl. Phys. Lett.*, vol. 1, pp. 82-83, 1962.

[37] J. W. Crowe and R. M. Craig, Jr., "GaAs Laser Linewidth Measurements by Heterodyne Detection," *Appl. Phys. Lett.*, vol. 5, pp. 72-74, 1964.

[38] H. Bachert and S. Raab, "The Influence of External Optical Coupling on the Threshold Current Density of GaAs Injection Lasers," *Phys. Stat. Sol.*, vol. 29, pp. 175-178, 1968.

[39] V. N. Morozov, V. V. Nikitin, and A. A. Sheronov, "Self-Synchronization of Modes in a GaAs Semiconductor Injection Laser," *JETP Lett.*, vol. 7, pp. 256-258, 1968.

[40] R. F. Broom, "Self-Modulation at Gigahertz Frequencies of a Diode Laser Coupled to an External Cavity," *Electron. Lett.*, vol. 5, pp. 571-572, 1969.

[41] R. F. Broom, E. Mohn, C. Risch, and R. Salathe, "Microwave Self-Modulation of a Diode Laser Coupled to an External Cavity," *IEEE J. Quantum Electron.*, vol. QE-6, pp. 328-334, 1970.

[42] R. Lang and K. Kobayashi, "External Optical Feedback Effects on Semiconductor Injection Laser Properties," *IEEE J. Quantum Electron.*, vol. QE-16, pp. 347-355, 1980.

[43] I. Ikushima and M. Maeda, "Self-Coupled Phenomena of Semiconductor Lasers Caused by an Optical Fiber," *IEEE J. Quantum Electron.*, vol. QE-14, pp. 331-332, 1978.

[44] O. Hirota and Y. Suematsu, "Noise Properties of Injection Lasers Due to Reflected Waves," *IEEE J. Quantum Electron.*, vol. QE-15, pp. 142-149, 1979.

[45] G. P. Agrawal, *Fiber-Optic Communication Systems*, 3rd ed., New York: Wiley-Interscience, 2002.

[46] A. Seko, Y. Mitsuhashi, T. Morikawa, J. Shimada, and K. Sakurai, "Self-Quenching in Semiconductor Lasers and Its Applications in Optical Memory Readout," *Appl. Phys. Lett.*, vol. 27, pp. 140-141, 1975.

[47] Y. Mitsuhashi, T. Morikawa, K. Sakurai, A. Seko, and J. Shimada, "Self-Coupled Optical Pickup," *Opt. Commun.*, vol. 17, pp. 95-97, 1976.

[48] W. J. Burke, M. Ettenberg, and H. Kressel, "Optical Feedback Effects in CW Injection Lasers," *Appl. Opt.*, vol. 17, pp. 2233-2238, 1978.

[49] Y. Mitsuhashi, J. Shimada, and S. Mitsutsuka, "Voltage Change across the Self-Coupled Semiconductor Laser," *IEEE J. Quantum Electron.*, vol. QE-17, pp. 1216-1225, 1981.

[50] A. Dandridge, R. O. Miles, and T. G. Giallorenzi, "Diode Laser Sensor," *Electron. Lett.*, vol. 16, pp. 948-949, 1980.

[51] J. H. Churnside, "Laser Doppler Velocimetry by Modulating a CO2 Laser with Backscattered Light," *Appl. Opt.*, vol. 23, pp. 61-66, 1984.

[52] J. H. Churnside, "Signal-to-Noise in a Backscatter-Modulated Doppler Velocimeter," *Appl. Opt.*, vol. 23, pp. 2097-2106, 1984.

[53] S. Shinohara, A. Mochizuki, H. Yoshida, and M. Sumi, "Laser Doppler Velocimeter Using the Self-Mixing Effect of a Semiconductor Laser Diode," *Appl. Opt.*, vol. 25, pp. 1417-1419, 1986.

[54] E. T. Shimizu, "Directional Discrimination in the Self-Mixing Type Laser Doppler Velocimeter," *Appl. Opt.*, vol. 26, pp. 4541-4544, 1987.

[55] H. W. Jentink, F. F. M. de Mul, H. E. Suichies, J. G. Aarnoudse, and J. Greve, "Small Laser Doppler Velocimeter Based on the Self-Mixing Effect in a Diode Laser," *Appl. Opt.*, vol. 27, pp. 379-385, 1988.

[56] M. H. Koelink, M. Slot, F. F. M. de Mul, J. Greve, R. Graaff, A. C. M. Dassel, and J. G. Aarnoudse, "In Vivo Blood Flow Velocity Measurements Using the Self-Mixing Effect in a Fiber-Coupled Semiconductor Laser," *Proc. SPIE*, vol. 1511, pp. 120-128, 1991.

[57] C. Zakian, M. Dickinson, and T. King, "Particle Sizing and Flow Measurement Using Self-Mixing Interferometry with a Laser Diode," *J. Opt. A: Pure Appl. Opt.*, vol. 7, pp. 445-452, 2005.

[58] G. Beheim and K. Fritsch, "Range Finding Using Frequency-Modulated Laser Diode," *Appl. Opt.*, vol. 25, pp. 1439-1442, 1986.

[59] D. Guo and M. Wang, "Self-Mixing Interferometer Based on Temporal-Carrier Phase-Shifting Technique for Micro-Displacement Reconstruction," *Opt. Commun.*, vol. 263, pp. 91-97, 2006.

[60] Yah Leng Lim, K. Bertling, Pierre Rio, J. R. Tucker, A. D. Rakić, "Displacement and Distance Measurement using the Change in Junction Voltage across a Laser Diode due to the Self- Mixing Effect", Proceedings of SPIE 6038, pp.378-387 (2006).

[61] W. Mao, S. Zhang, L. Cui, and Y. Tan, "Self-Mixing Interference Effects with a Folding Feedback Cavity in Zeeman-Birefringence Dual Frequency Laser," *Opt. Express*, vol. 14, pp. 182-189, 2006.

[62] U. Zabit , F. Bony , T. Bosch and A. D. Rakic, "A self-mixing displacement sensor with fringe-loss compensation for harmonic vibrations", *IEEE Photon. Technol. Lett.*, vol. 22, pp. 410-412, 2010.

[63] L. Arriaga, F. Bony and T. Bosch, "Real-Time Algorithm for Versatile Displacement Sensors Based on Self-Mixing Interferometry," in *IEEE Sensors Journal*, vol. 16 (1), pp. 195-202, 2016.

[64] M. Norgia, G. Giuliani, and S. Donati, "New Absolute Distance Measurement Technique by Self-Mixing Interferometry in Closed Loop," in *Proc. 21st IEEE Instrum. Meas. Technol. Conf.*, vol. 1, IEEE, 2004, pp. 216-221.

[65] L. Kervevan, H. Gilles, S. Girard, M. Laroche, and Y. Monfort, "Absolute Distance Measurement with Heterodyne Optical Feedback on a Yb:Er Glass Laser," *Appl. Opt.*, vol. 45, pp. 4084-4091, 2006.

[66] A. Sakamoto, N. Tsuda, and J. Yamada, "Characteristic of Self-Coupling Distance Meter Using VCSEL," *IEEJ Trans. EIS*, vol. 126, pp. 1454-1459, 2006.

[67] H. Wang, T. Zhao, J. Xu, D. He, L. Lu, H. Gui, W. Huang, H. Ming, and J. Xie, "Optimized Design of Laser Range Finding System Using the Self-Mixing Effect in a Single-Mode VCSEL," *Chin. Opt. Lett.*, vol. 4, pp. 87-90, 2006.

[68] D. Guo and M. Wang, "Self-Mixing Interferometry Based on a Double-Modulation Technique for Absoluted Distance Measurement," *Appl. Opt.*, vol. 46, pp. 1486-1491, 2007.

[69] L. Scalise, Y. Yu, G. Giuliani, G. Plantier, and T. Bosch, "Self-Mixing Laser Diode Velocimetry: Application to Vibration and Velocity Measurement," *IEEE Trans. Instrum. Meas.*, vol. 53, pp. 223-232, 2004.

[70] H.-Q. Gui, L. Lu, D.-Y. He, J. Xu, J.-P. Xie, T.-P. Zhao, A.-T. Wang, and H. Ming, "New Laser Doppler Velocimetry with Wide Dynamic Range and Clear Directional Discrimination," *Chin. Phys. Lett.*, vol. 22, pp. 1344-1346, 2005.

[71] L. Lv, H. Gui, T. Zhao, J. Xu, D. He, A. Wang, X. C. F. Li, H. Ming, and J. Xie, "Theoretical and Numerical Analysis of Polarization Properties Used as Doppler Velocimetry in Vertical-Cavity Surface-Emitting Lasers," *Proc. SPIE*, vol. 5644, pp. 829-834, 2005.

[72] C. Zakian, M. Dickinson, and T. King, "Dynamic Light Scattering by Using Self-Mixing Interferometry with a Laser Diode," *Appl. Opt.*, vol. 45, pp. 2240-2245, 2006.

[73] L. Kervevan, H. Gilles, S. Girard, M. Laroche, and P. Leprince, "Self-Mixing Laser Doppler Velocimetry with a Dual-Polarization Yb:Er Glass Laser," *Appl. Phys. B*, vol. 86, pp. 169-176, 2007.

[74] L. Scalise, W. Steenbergen, and F. de Mul, "Self-Mixing Feedback in a Laser Diode for Intra-Arterial Optical Blood Velocimetry," *Appl. Opt.*, vol. 40, pp. 4608-4615, 2001.

[75] T. Ren, A. L. Nuttall, and J. M. Miller, "Relative Blood Velocity Measurement in Individual Microvessels Using the Self-Mixing Effect in a Fiber-Coupled Helium-Neon Laser," *Microvasc. Res.*, vol. 49, pp. 233-245, 1995.

[76] M. Wang, M. Lu, H. Hao, and J. Zhou, "Statistics of the Self-Mixing Speckle Interference in a Laser Diode and Its Application to the Measurement of Flow Velocity," *Opt. Commun.*, vol. 260, pp. 242-247, 2006.

[77] E. E. Ramirez-Miquet, A. L. Arriaga, A. Quotb, O. Sotolongo-Costa and J. Perchoux, "In-situ measurement of non-steady flows using optical feedback interferometry," *Industrial Technology (ICIT), 2015 IEEE International Conference on*, Seville, 2015, pp. 1469-1473.

[78] J. Perchoux, A. Quotb, R. Atashkhooei, F. J. Azcona, E. E. Ramirez-Miquet, O. Bernal, A. Jha, A. Luna-Arriaga, C. Yanez, J. Caum, T. Bosch and S. Royo, " Current Developments on Optical Feedback Interferometry as an All-Optical Sensor for Biomedical Applications," *Sensors*, vol. 16(5), p. 694, 2016.

[79] P. J. de Groot and G. M. Gallatin, "Three-Dimensional Imaging Coherent Laser Radar Array," *Opt. Eng.*, vol. 28, pp. 456-460, 1989.

[80] P. J. de Groot, G. M. Gallatin, and M. F. Cullen, "Compact Imaging System with Ranging and Velocimetry," *Proc. SPIE*, vol. 1005, pp. 153-163, 1989.

[81] J. R. Tucker, Y. L. Lim, A. V. Zvyagin and A. D. Rakic, "A Massively Parallel Imaging System Based on the Self-Mixing Effect in a Vertical-Cavity Surface-Emitting Laser Array," *2006 Northern Optics*, Bergen, 2006, pp. 41-45.

[82] J. R. Tucker, J. L. Baque, Y. L. Lim, A. V. Zvyagin and A. D. Rakic, " Parallel self-mixing imaging system based on an array of vertical-cavity surface-emitting lasers," *Applied optics*, 46(25), pp. 6237-6246, 2007.

[83] Y. L. Lim, R. Kliese, K. Bertling, K. Tanimizu, P. A. Jacobs and A. D. Rakic, "Parallel self-mixing flow sensor using monolithic VCSEL array," *2009 14th OptoElectronics and Communications Conference*, Hong Kong, 2009, pp. 1-2.

[84] C. Gorecki, S. Khalfallah, H. Kawakatsu, and Y. Arakawa, "New SNOM Sensor Using Optical Feedback in a VCSEL-Based Compound-Cavity," *Sens. Actuat. A-Phys.*, vol. 87, pp. 113-123, 2001.

[85] D. Heinis, C. Gorecki, C. Bringer, V. Bardinal, T. Camps, J. Doucet, P. Dubreruil, and C. Fontaine, "Miniaturized Scanning Near-Field Microscope Sensor Based on Optical Feedback inside a Single-Mode Oxide-Confined Vertical-Cavity Surface-Emitting Laser," *Jpn. J. Appl. Phys.*, vol. 42, pp. L1469-L1471, 2003.

[86] D. Heinis, Y. Poujet, C. Gorecki, A. Lesuffleur, and P. Gogol, "A New Concept of an Integrated SNOM Microscope Using Optical Feedback within Vertical Cavity Surface Emitting Lasers," *J. Korean Phys. Soc.*, vol. 46, pp. 182-185, 2005.

[87] D. S. Burgess, "Microscopy Focus: Feedback-Based Imaging Enables Miniature Scanning Confocal Microscopes," *Photon. Spectra*, vol. 40, pp. 113-114, 2006.

[88] D. Heinis, C. Gorecki, S. Bargiel, and B. Cretin, "Feedback-Induced Voltage Change of a Vertical-Cavity Surface-Emitting Laser as an Active Detection System for Miniature Optical Scanning Probe Microscopes," *Opt. Express*, vol. 14, pp. 3396-3405, 2006.

[89] H. Gilles, S. Girard, M. Laroche and A Belarouci, "Near-field amplitude and phase measurements using heterodyne optical feedback on solid-state lasers," *Optics letters*, 33(1), pp. 1-3, 2008.

[90] B. Ovryn and J. H. Andrews, "Phase-Shifted Laser Feedback Interferometry," *Opt. Lett.*, vol. 23, pp. 1078-1080, 1998.

[91] A. Bearden, M. P. O'Neill, L. C. Osborne, and T. L. Wong, "Imaging and Vibrational Analysis with Laser-Feedback Interferometry," *Opt. Lett.*, vol. 18, pp. 238-240, 1993.

[92] M. Wang and G. Lai, "Self-Mixing Microscopic Interferometer for the Measurement of Microprofile," *Opt. Commun.*, vol. 238, pp. 237-244, 2004.

[93] A. Valavanis *et al*., "Surface-profiling through self-mixing in a THz quantum cascade laser," *in International Quantum Cascade Lasers School & Workshop 2012, Austria*.

[94] T. Pereira, M. Sequeira, P. Vaz, et al., "Submicron Surface Vibration Profiling Using Doppler Self-Mixing Techniques," Advances in Optics, 2014.

[95] T. Bosch, N. Servagent, and F. Boyer, "Vibrations Measurements with a Self-Mixing Type Laser Displacement Sensor for Modal Analysis," in *Proc. 13th IEEE Instrum. Meas. Technol. Conf.*, vol. 1, IEEE, 1996, pp. 648-653.

[96] T. Bosch, N. Servagent, and M. Lescure, "A Displacement Sensor for Spectrum Analysis Using the Optical Feedback in a Single-Mode Laser Diode," in *Proc. 14th IEEE Instrum. Meas. Technol. Conf.*, vol. 2, IEEE, 1997, pp. 870-873.

[97] N. Servagent, T. Bosch, and M. Lescure, "A Laser Displacement Sensor Using the Self-Mixing Effect for Modal Analysis and Defect Detection," *IEEE Trans. Instrum. Meas.*, vol. 46, pp. 847-850, 1997.

[98] T. Bosch, N. Servagent, R. Chellali, and M. Lescure, "A Scanning Range Finder Using the Self-Mixing Effect inside a Laser Diode for 3-D Vision," in *Proc. 13th IEEE Instrum. Meas. Technol. Conf.*, vol. 1, IEEE, 1996, pp. 226-231.

[99] Y. Ichioka, F. Fukushima, S. Shinohara, H. Ikeda, H. Yoshida, and M. Sumi, "Search of a Moving Object and Its Range-Image Measurement Using Range Finding Speedometer," in *Proc. 31st IAS Ann. Meeting*, vol. 3, IEEE, 1996, pp. 1635-1639.

[100] E. Gagnon, "A 3-D Laser Range Scanner Based on the Self-Mixing Effect in a Laser Diode," M.S. thesis, Dept. Elect. Eng., University of Ottawa, Ontario, Canada, 1997.

[101] T. Bosch, N. Servagent, R. Chellali, and M. Lescure, "Three-Dimensional Object Construction Using a Self-Mixing Type Scanning Laser Range Finder," *IEEE Trans. Instrum. Meas.*, vol. 47, pp. 1326-1329, 1998.

[102] E. Gagnon and J. F. Rivest, "Laser Range Imaging Using the Self-Mixing Effect in a Laser Diode," *IEEE Trans. Instrum. Meas.*, vol. 48, pp. 693-699, 1999.

[103] J. Perchoux, L. Campagnolo, Y. L. Lim and A. D. Rakic, "“Lens-free” self-mixing sensor for velocity and vibrations measurements," *2010 Conference on Optoelectronic and Microelectronic Materials and Devices*, Canberra, ACT, 2010, pp. 43-44.

[104] M Norgia, L Kun, A Palludo, F Cavedo and A. Pesatori, "Self-mixing laser sensor for short-distances measurement," in *AIP Conf. Proc.* 1740 (1), 100002 (2016).

[105] Kliese, R.; Yah Leng Lim; Bertling, K.; Bakar, A.A.A.; Bosch, T.; Rakic, A.D. , “Self-mixing displacement sensing using the junction voltage variation in a GaN laser” Proceedings of the 2008 IEEE Conference on Optoelectronic and Microelectronic, Materials and Devices, pp 23-25, (2008).

[106] J. R. Tucker, A. Mowla, J. Herbert, M. A. Fuentes, C. S. Freakley, K. Bertling, Y. L. Lim, R. S. Matharu, J. Perchoux, T. Taimre, S. J. Wilson, and A. D. Rakić, “Self-mixing sensing system based on uncooled vertical-cavity surface-emitting laser array: linking multichannel operation and enhanced performance,” Opt. Lett. 39, 394–397 (2014).

[107] Perchoux, J., Dougan, H.E., Bony, F., Rakic, A.D., “Photodiode-free Doppler velocimeter based on self-mixing effect in commercial VCSELs”, IEEE Sensors conference, pp. 290 – 293, 2008.

[108] J. T. Verdeyen, *Laser Electronics*, 3rd ed., (Prentice Hall, 1995).

[109] P. J. de Groot, G. M. Gallatin, and S. H. Macomber, "Ranging and Velocimetry Signal Generation in a Backscatter-Modulated Laser Diode," *Appl. Opt.*, vol. 27, pp. 4475-4480, 1988.

[110] M. H. Koelink, M. Slot, F. F. M. de Mul, J. Greve, R. Graaff, A. C. M. Dassel, and J. G. Aarnoudse, "Laser Doppler Velocimeter Based on the Self-Mixing Effect in a Fiber-Coupled Semiconductor Laser: Theory," *Appl. Opt.*, vol. 31, pp. 3401-3408, 1992.

[111] K. Petermann, *Laser Diode Modulation and Noise*, Dordrecht, (Kluwer Academic, 1991).

[112] D.-S. Seo, J.-D. Park, J. G. McInerney, and M. Osinski, “Effects of feedback asymmetry in external-cavity semiconductor laser systems,” Electron. Lett. 24, 726 (1988).

[113] R. C. Addy, A. W. Palmer, and K. T. V. Grattan, “Effects of external reflector alignment in sensing applications of optical feedback in laser diodes,” IEEE, Journal of Lightwave Technology, vol. 14, No 12, pp. 2672–2676, 1996.

[114] Y. Yu, H. Ye, and J. Yao, “Analysis for the Self-Mixing Interference Effects in a Laser Diode at High Optical Feedback Levels,” J. Opt. A.: Pure Appl. Opt. 5, 117-122 (2003).

[115] L. Golderg, H. F. Taylor, A. Dandridge, J. F. Weller, and R. O. Miles, “Spectral Characteristics of Semiconductor Lasers with Optical Feedback” IEEE J. Quantum Electron, Vol. QE-18, pp. 555-564, (1982).

[116] T. Bosch, C. Bes, L. Scalise, and G. Plantier, “Optical feedback interferometry,” Encyclopaedia Sens. X, 1–20 (2006).

[117] J. O. Binder and G. D. Cormack , "Mode selection and stability of a semiconductor laser with weak optical feedback" , *IEEE J. Quantum Electron.* , vol. 25 , pp.2255 -2259, 1989.

[118] J. Mork and B. Tromborg , "The mechanism of mode selection for an external cavity laser" , *IEEE Photon. Technol. Lett.* , vol. 2 , pp.21 -23 , 1990.

[119] D. Lenstra, "Statistical theory of the multistable external-feedback laser," Opt. Commun. 81, 209-214 (1991).

[120] R. W. Tkach and A. R. Chraplyvy, “Regimes of feedback effects in 1.5 pm distributed feedback lasers,” Journal of Lightwave Technology, Vol. LT-4, pp. 1655-1661,(1986).

[121] S. Donati and M. T. Fathi, “Transition from short-to-long cavity and from self-mixing to chaos in a delayed optical feedback laser,” IEEE J. Quantum Electron., vol. 48, no. 10, pp. 1352–1359, Oct. 2012.

[122] N. Servagent, F. Gouaux, and T. Bosch, "Measurements of Displacement Using the Self-Mixing Interference in a Laser Diode," *J. Opt.*, vol. 29, pp. 168-173, 1998.

[123] N. Servagent, T. Bosch, and M. Lescure, "Design of a Phase-Shifting Optical-Feedback Interferometer Using an Electrooptic Modulator," *IEEE J. Select. Topics Quantum Electron.*, vol. 6, pp. 798-802, 2000.

[124] N. Takahashi, S. Kakuma, and R. Ohba, “Active heterodyne interferometric displacement measurement using optical feedback effects of laser diodes,” Optical Engineering, vol. 35, pp. 802–807, 1996.

[125] C. Bes, G. Plantier, and T. Bosch, "Displacement Measurements Using a Self-Mixing Laser Diode under Moderate Feedback," *IEEE Trans. Instrum. Meas.*, vol. 55, pp. 1101-1105, 2006.

[126] C. Bes, V. Belloeil, G. Plantier, Y. Gourinat and T. Bosch, “A self-mixing laser sensor design with an extended Kalman filter for optimal online structure analysis and damping evaluation”, IEEE/ASME Trans. on Mechatronics, Vol. 12, No. 3, pp. 387-394, 2007.

[127] C. Bes, T. Bosch, G. Plantier and F. Bony, "Characterisation of a self-mixing displacement sensor under moderate feedback". Optical Engineering, Vol. 45, No. 8, pp. 084402-1–084402-6, 2006.

[128] A. Doncescu, C. Bes and T. Bosch, “Displacement Estimation with an Optical Feedback Interferometer Using an Evolutionary Algorithm”, Proceedings of IEEE Sensors 2007, Atlanta, 2007.

[129]. P. A. Roos, M. Stephens, and C. E. Wieman, “Laser vibrometer based on optical-feedback induced frequency modulation of a single-mode laser diode”, Applied Optics, Vol. 35, pp. 6754-6761, 1996.

[130]. G. Giuliani, S. Bozzi-Pietra, and S. Donati, “Self-mixing laser diode vibrometer,” Measurement Science and Technology, Vol. 14, pp. 24-32, 2003.

[131]. M. Norgia,C. Svelto,“Novel Measurement Method for Signal Recovery in Optical Vibrometer”, IEEE Transactions on Instrumentation and Measurement, Vol. 57, Issue 8, pp.1703 – 1707, 2008.

[132] X. Raoul, T. Bosch, G. Plantier, and N. Servagent, "A Double-Laser Diode Onboard Sensor for Velocity Measurements," *IEEE Trans. Instrum. Meas.*, vol. 53, pp. 95-101, 2004.

[133] G. Plantier, N. Servagent, A. Sourice, and T. Bosch, "Real-Time Parametric Estimation of Velocity Using Optical Feedback Interferometry," *IEEE Trans. Instrum. Meas.*, vol. 50, pp. 915-919, 2001.

[134] M. A. Amann, T. Bosch, M. Lescure, R. Myllyla, and M. Rioux, "Laser ranging: a critical review of usual techniques for distance measurement",Optical Eng. Vol. 40, pp. 10-19, 2001.

[135] G. Giuliani, M. Norgia, S. Donati and T. Bosch, "Laser diode self-mixing technique for sensing applications", Journal of Optics A: Pure and Applied Optics, Vol. 4, pp. 283-294, 2002.

[136] E. G. Williams, J. Maynard, and E. Skudrzyk, "Sound source reconstructions using a microphone array," J. Acoust. Soc. Am. 68, pp. 340-344, 1980.

[137] P. A. Chinnery, V. F. Humphrey, and C. Beckett, "The schlieren image of two-dimensional ultrasonic fields and cavity resonances," J. Acoust. Soc. Am., vol. 101, pp. 250-256, 1997.

[138] R. Malkin, T. Todd, and D. Robert, "A simple method for quantitative imaging of 2D acoustic fields using refracto-vibrometry," J. Sound Vib., Vol. 333, pp. 4473-4482, 2014.

[139] K. Bertling, J. Perchoux, T. Taimre, R. Malkin, D. Robert, A. D. Rakić, and T. Bosch, "Imaging of acoustic fields using optical feedback interferometry," Opt. Express 22, pp. 30346-30356, 2014.

[140] C. Zakian, M. Dickinson, and T. King, "Particle sizing and flow measurement using self-mixing interferometry with a laser diode," J. Opt. A, Pure Appl. Opt. **7**(6), pp. 445-452, 2005.

[141] G. Osche, *Optical Detection Theory for Laser Applications* (John Wiley and Sons Inc., 2002).

[142] S. Sudo, Y. Miyasaka, K. Nemoto, K. Kamikariya, and K. Otsuka, "Detection of small particles in fluid flow using a self-mixing laser," Opt. Express **15**(13), pp. 8135-8145, 2007.

[143] H. Wang and J. Shen, “Fast and economic signal processing technique of laser diode self-mixing interferometry for particle size measurement,” Appl. Phys. B **115**(2), pp. 285-291, 2014.

[144] V. Contreras, J. Lonnqvist, and J. Toivonen, “Edge filter enhanced self-mixing interferometry,” Opt. Lett. **40**(12), pp. 2814-2817, 2015.

[145] V. Contreras, J. Lonnqvist, and J. Toivonen, “Detection of single microparticles in airflows by edge-filter enhanced self-mixing interferometry,” Opt. Express **24** (8), p. 8886, 2016.

[146] G. Giuliani and S. Donati, “Laser interferometry,” in *Unlocking Dynamical Diversity: Optical Feedback Effects on Semiconductor Lasers*, D. M. Kane and K. A. Shore, eds. (Wiley, 2005), pp. 217-255.

[147] L. A. Coldren, S. W. Corzine, and M. L. Mashanovitch, *Diode Lasers and Photonic Integrated Circuits*, 2nd ed. (Wiley, 2012).

[148] G. Acket, D. Lenstra, A. den Boef, and B. Verbeek, “The influence of feedback intensity on longitudinal mode properties and optical noise in index-guided semiconductor lasers,” IEEE J. Quantum Electron. 20, pp. 1163-1169, 1984.

[149] J. Al Roumy, J. Perchoux, Y. L. Lim, T. Taimre, A. D. Rakić, and T. Bosch, “Effect of injection current and temperature on signal strength in a laser diode optical feedback interferometer,” Appl. Opt. 54, pp. 312-318, 2015.

[150] J. Katz, S. Margalit, C. Harderer, D. Wilt, and A. Yariv, “The intrinsic electrical equivalent circuit of a laser diode,” IEEE J. Quantum Electron. 17**,** pp. 4-7, 1981.

[151] R. Juskaitis, N. P. Rea, and T. Wilson, “Semiconductor laser confocal microscopy,” Appl. Opt. 33, pp. 578-584, 1994.

[152] E. M. Randone and S. Donati, “Self-mixing interferometer: analysis of the output signals,” Opt. Express 14, pp. 9788-9796, 2006.

[153] J. Al Roumy, J. Perchoux, and T. Bosch, “Phase Relationship of Photodetected Signals of an Optical Feedback Interferometry Sensor,” (Submitted to CLEO-PR).

[154] R. Kliese, Y. L. Lim, T. Bosch, and A. D. Rakić, Opt. Lett. 35, p. 814, 2010.

[155] T. Hertsens, “Measuring diode laser characteristics,” ILX Lightwave Appl. Note 5, 2005.

[156] Yi. Hu, M. Bhatnagar, and P. C. Loizou, “A cross-correlation technique for enhancing speech corrupted with correlated noise,” in Proceedings of International Conference on Acoustics, Speech, and Signal Processing, vol. 1, pp. 673-676, 2001.

[157] J. G. Proakis and D. G. Manolakis, *Digital Signal Processing: Principles, Algorithms, and Applications*, 4th ed. (Prentice Hall, 2007).

[158] Y.W. Lee, T.P. Cheatham, and J.B. Wiesner, “The application of correlation functions to the detection of small signals in noise,” *Tech. Rep.* 141, 1949.

List of Publications

International Journals:

1. J. Al Roumy, J. Perchoux, Y. L. Lim, T. Taimre, A. D. Rakic, and T. Bosch, "Effect of injection current and temperature on signal strength in a laser diode optical feedback interferometer," Appl. Opt. 54, pp. 312-318, 2015.

International Conferences:

1. J. Al Roumy, J. Perchoux, Y. L. Lim, T. Taimre, A. D. Rakic, and T. Bosch, "Effect of injection current on signal strength in a singlemode laser diode subject to feedback," in *2015 European Conference on Lasers and Electro-Optics - European Quantum Electronics Conference*, (Optical Society of America, 2015), paper CH_8_1.
2. J. Al Roumy, J. Perchoux, and T. Bosch, "Phase Relationship of Photodetected Signals of an Optical Feedback Interferometry Sensor," in *2015 Conference on Lasers and Electro-Optics Pacific Rim*, (Optical Society of America, 2015), paper 27F1_4.

Abstract

Title: Analysis of the different signal acquisition schemes of an optical feedback based laser diode interferometer.

Abstract: The optical feedback interferometry phenomenon occurs when a portion of the output optical power is back-scattered from a remote target and coupled into the laser cavity to vary the laser's emission properties (frequency and power mostly). Thus, this scheme results in a compact, self-aligned and contact-less interferometric sensor. Recent applications of optical feedback interferometer in the domains of microfluidics or acoustics have shown promising results and open new fields of researches. However in these applications, the amplitude of the sensing signal is extremely small due to the weakness of the backscattered power changes that are measured. In this thesis, an analytical model that describes the laser injection current and temperature dependence of the optical feedback interferometry signal strength for a single-mode laser diode has been derived from the Lang and Kobayashi rate equations. The model has been developed for all the known signal acquisition methods of the optical feedback interferometry scheme: from the package included monitoring photodiode, by collection of the laser power with an external photodetector and by amplification of the variations in the laser junction voltage. The model shows that both the photodiodes and the voltage signals strengths are related to the laser slope efficiency, which itself is a function of the laser injection current and of the temperature. Moreover, the model predicts different behaviors of the photodiodes and the voltage signal strengths with the change of the laser injection current and the temperature; an important result that has been proven by conducting measurements on all three signals for a wide range of injection current and temperature. Therefore, this simple model provides important insights into the radically different biasing strategies required to achieve optimal sensor sensitivity for the different interferometric signal acquisition schemes. In addition, the phase and amplitude relationships between the external and the in-package photodiode signals have been investigated theoretically and experimentally demonstrating unexpected results. Based on our model and on experimental observations, a critical study has been performed on the impact of the combination of the three signals in the signal processing strategy in order to improve the sensor sensibility to low amplitude optical feedback.

Key words: Optical Feedback Interferometry; Self-Mixing; Modeling; Laser rate equations; Sensor; Laser diode.

Résumé

Titre: Analyse des différents schémas d'acquisition d'un capteur interférométrique par réinjection optique dans une diode laser.

Résumé: Le phénomène d'interférométrie par réinjection optique se produit lorsqu'une portion de la puissance optique du laser est rétrodiffusée par une cible distante puis réinjectée dans la cavité laser ce qui affecte les propriétés d'émission du laser (fréquence et puissance en particulier). Ce principe résulte alors en un capteur interférométrique compact, auto-aligné et sans contact. Des applications récentes des capteurs par réinjection optique dans les domaines de la microfluidique et de l'acoustique ont montré des résultats prometteurs et ouvert de nouveaux domaines de recherche. Pourtant, dans le cadre de ces applications, l'amplitude du signal est extrêmement faible à cause de la faible amplitude des variations de la puissance rétrodiffusée qui est mesurée. Dans cette thèse, un modèle analytique décrivant la dépendance de l'amplitude du signal issu d'une diode laser monomode au courant d'injection et à la température est développé à partir des équations d'évolution de Lang et Kobayashi. Le modèle a été développé pour toutes les méthodes connues d'acquisition du signal interférométrique par réinjection optique : par la photodiode de monitoring incluse dans le boîtier de la diode laser, par la captation de la puissance optique au moyen d'un photodétecteur externe et par l'amplification de la tension aux bornes de la diode laser elle-même. Le modèle démontre que les signaux des photodiodes et de la tension sont liés à l'efficacité externe de la diode laser, qui elle-même est fonction du courant injecté et de la température. Qui plus est, le modèle prédit une évolution très différente de l'amplitude de ces différents signaux en fonction du courant d'injection ou de la température. Un résultat remarquable, confirmé par une campagne de mesures pour ces trois types de signaux sur une large plage de courants d'injection et de températures. Ainsi ce modèle simple permet une compréhension nouvelle des stratégies de polarisation très différentes de la diode laser permettant d'obtenir une sensibilité optimale du capteur dans les différents schémas d'acquisition du signal. Par ailleurs, les relations entre la phase et l'amplitude des signaux issus des photodiodes externes et de monitoring ont été étudiées sur le plan théorique et expérimental ce qui a permis de révéler des résultats inattendus. À partir du modèle et basé sur des observations expérimentales, une étude critique a été menée sur l'impact de la combinaison des trois signaux dans la stratégie de traitement du signal afin d'améliorer la sensibilité du capteur aux réinjections optiques de faible amplitude.

Mots clés: Interférométrie par réinjection optique; Self-Mixing; Modélisation; Équations d'évolution; Capteur; Diode laser.